

## Durham E-Theses

---

### *Electrosharpening of Tungsten Probes for Arc Discharge Assembly of Carbon Nanotubes*

STONE, RICHARD,FRANCIS,LEICESTER

#### How to cite:

---


STONE, RICHARD,FRANCIS,LEICESTER (2016) *Electrosharpening of Tungsten Probes for Arc Discharge Assembly of Carbon Nanotubes*, Durham theses, Durham University. Available at Durham E-Theses Online: <http://etheses.dur.ac.uk/11666/>

#### Use policy

---



This work is licensed under a [Creative Commons Attribution No Derivatives 3.0](https://creativecommons.org/licenses/by-nd/3.0/)  
(CC BY-ND)



# Electrosharpening of Tungsten Probes for Arc Discharge Assembly of Carbon Nanotubes

A Thesis for a  
Doctorate of Philosophy in  
Engineering

Richard Stone

Supervisor: Professor D. A. Zeze

Secondary Supervisors: Profs. M. C. Petty & K. S. Coleman



**Durham**  
University  
School of Engineering  
& Computer Sciences

# Abstract

Ultra-sharp tungsten probes fill a key role in science for allowing measurements and interactions at the nanoscale. However, their current method of fabrication is outdated, fundamentally limited in length, sharpness and consistency, and often referred to as an ‘art’.

A new process of fabricating ultra-sharp tungsten probes known as ‘Tungstate Sharpening’ was invented. This electrochemical process utilises solely the  $\text{WO}_4^{2-}$  by-product to create a gradient of etching which results in a sharpening effect. It was shown to electrochemically etch probes controllably over lengths from 0.5 – 4.5 mm with tip radii of 10 nm via a fully automated process. Tungstate sharpening overcomes many of the limitations of the previous methods as well as creating new opportunities for further research into electrosharpening.

Tungstate sharpening was improved to use bulk coulometry analysis which allows users to select specific probe lengths. The process was also modified to allow etching of five probes simultaneously, which is fundamentally impossible with conventional techniques. Furthermore, this batch process was improved with the application of a magnetic field that reduced fabrication time and inconsistencies. Flow simulations were conducted to confirm experimental observations of the electrode separation influence on turbulence within the electrochemical system, supporting the underlying theory and observations of the tungstate layer. Finally, this processing technique was expanded with various materials and shapes to demonstrate versatility. Razor blades with edge radii of 40 nm were produced demonstrating that electrosharpening is no longer limited to ‘1D’ objects.

Another process was developed to fabricate carbon nanotubes (CNTs) as a macroscopic material. ‘Arc Assembly’ was invented to explore the possibility of forming long chains of CNTs whilst maintaining the  $sp^2$  crystalline bonding within and between individual CNTs.

For the first time, dielectrophoresis was combined with arc discharges to form ‘threads’ of CNTs using the tungsten probes produced. The tungsten probes were applied as electrodes for dielectrophoresis of CNT chains and simultaneous arcing between them. Multiple high voltage circuits with outputs ranging from beneath the breakdown threshold and negative  $K(\omega)$  up to 1000 V and 8 MHz were constructed and tested. Dispersed carbon nanotube mixtures for a variety of dielectric organic fluids, solvents and polymers were placed between the electrodes. The resulting phenomenon was the assembly of dielectrophoretic chains with arc-induced adhesion between nanotubes: termed as “Arc Assembly”.

As Arc Assembly was developed, the CNT threads were analysed using scanning electron microscopy, energy dispersive X-ray spectroscopy, transmission electron microscopy and Raman analysis. Observations were made of both amorphous and crystalline links between the CNTs, as well as embedded CNT chains within in-situ formed polymer composites. The process produced threads of carbon nanotubes up to 5 mm length, indicating that this may be a viable means of exploiting CNTs in every-day life.



# Contents

<b>Abstract.....</b>	<b>2</b>
<b>Chapter 1: Introduction .....</b>	<b>10</b>
1.1 Research Objective .....	10
1.2 Project Scope .....	12
1.3 Thesis Structure .....	13
1.4 References.....	15
<b>Chapter 2: Tungstate Sharpening .....</b>	<b>19</b>
2.1 Introduction.....	19
2.2 General Principles of Electrosharpening .....	20
2.2.1 Basic Electrochemical Reaction .....	20
2.2.2 Intermediary Steps .....	21
2.3 Drop-Off Method Experimental Progression.....	23
2.3.1 The Drop-off Method.....	25
2.3.2 Angled Electrosharpening.....	27
2.4 Shadowgraphs .....	30
2.4.1 Introduction to Shadowgraphs .....	30

2.5 Principles of Tungstate Sharpening .....	34
2.6 Implementation .....	35
2.6.1 Control Through Bulk Coulometry.....	36
2.6.2 Observations of Tungsten Trioxide .....	39
2.7 Automation Programming Concept .....	41
2.7.1 Software Implementation.....	43
2.7.2 Automated Electrochemical Circuitry .....	44
2.8 Automated Electrosharpening.....	46
2.8.1 Tip Radius.....	50
2.8.2 Overall Tip Length.....	51
2.9 Probe Geometry .....	52
2.9.1 Bulk Coulometry Calculations.....	54
2.9.2 Evaluation of Calculations .....	57
2.10 Scanning Tunnelling Microscopy Application .....	58
2.11 Conclusion .....	61
2.12 References.....	63
<b>Chapter 3: Enhancements to Electrosharpening .....</b>	<b>69</b>
3.1 Introduction.....	69
3.2 Conventional Techniques Applied to Batch Electrosharpening .....	69
3.3 Tungstate Sharpening Applied to Batch Electrosharpening .....	71
3.4 Modelling Fluid Flow Within Batch Electrosharpening.....	75

3.5 Lorentz Force Theory .....	82
3.5.2 Application Within Electrosharpening .....	83
3.6 Magnetic Enhancements to Batch Electrosharpening.....	86
3.7 Evaluation of Batch Electrosharpening .....	90
3.8 Fabrication of Razor Blades.....	92
3.9 Conclusion .....	95
3.10 References.....	97
<b>Chapter 4: Arc Assembly .....</b>	<b>103</b>
4.1 Carbon Nanotube Overview .....	103
4.1.1 Interest in Carbon Nanotube Yarns.....	103
4.1.2 Carbon Nanotube Characteristics .....	104
4.1.3 Synthesis of Carbon Nanotubes .....	105
4.2 Introduction to Dielectrophoresis .....	108
4.2.2 The Clausius-Mossotti Function .....	109
4.3 Dielectrophoresis for Arc Assembly of Carbon Nanotubes .....	110
4.4 Arc Assembly Implementation .....	112
4.4.1 Intermittent Arc Assembly Circuit.....	112
4.4.2 Continuous Arc Assembly Circuit .....	113
4.4.3 General Arc Assembly Mechanism .....	115
4.5 COMSOL Models of Electric Field Strength .....	117
4.5.1 Principles of Model.....	117

4.5.2 Substrate and Atmosphere .....	118
4.5.3 Geometry of the Droplet on a Surface .....	119
4.5.4 Geometry of the Probe .....	121
4.6 Findings and implications from COMSOL simulations .....	124
4.6.1 Matching Simulation to Experiments .....	124
4.6.2 Electrode Distance Analysis .....	125
4.6.3 Probe Sharpness Analysis .....	127
4.6.4 Preliminary SEM Results.....	128
4.6.5 Evidence for Fluidic Motion Within Continuous Arc Assembly .....	131
4.6.6 Initial Electrical Measurements .....	133
4.7 Arc Assembly TEM .....	134
4.8 EDX Spectroscopy of TEM results.....	137
4.8 TEM Electron Diffraction Patterns .....	139
4.10 Raman Spectroscopy.....	144
4.10.1 Raman Spectrum of Continuous Arc Assembled Thread .....	147
4.10.2 Raman Spectroscopy of G-Bands .....	149
4.10.3 Evaluation of Raman Spectroscopy Results .....	150
4.11 Conclusion .....	153
4.12 References.....	155
<b>Chapter 5: Conclusion.....</b>	<b>163</b>
5.1 Electrosharpening Conclusion .....	163

5.2 Future Work on Tungstate Sharpening and Enhancements to Electrosharpening.....	165
5.3 Arc Assembly Conclusion .....	166
5.4 Future Work on Arc Assembly .....	167
Final Remark.....	169
Acknowledgements.....	170
Publications, Conferences, Awards & Patents.....	171
Journal Papers .....	171
Conference Proceedings.....	171
Prizes .....	172
Patents .....	172
<b>Appendix.....</b>	<b>173</b>
Automated Measurement .....	173
Measurement Thresholds .....	175
Programmatic Integration of Data .....	177
Process Control .....	179
Output Control .....	181
User Determined Parameters .....	183
Front End .....	185
Future Improvements.....	186
Cover Picture Details .....	187





# Chapter 1

## Introduction

# Chapter 1: Introduction

## 1.1 Research Objective

We are building our world on smallness. As we do, our interest in the nanoscopic world grows at an ever increasing rate and our tools and methods to explore and exploit this world need to meet the demands of this modern era.

In 1936 Erwin Muller used Field Electron Microscopy<sup>1</sup> (FEM) with a sharpened tungsten probe to display the arrangement of the atoms present at the tip. In 1982 Binning and Rohrer used tungsten probes to develop scanning tunnelling microscopy<sup>2</sup> (STM) to show the atomic surface of gold. This technique remains essential for nanoscopic analysis today. The tungsten probes which were essential to developing these experiments are also finding more applications in variants on scanning probe microscopy<sup>3</sup> (SPM), neuroscience<sup>4</sup> and dielectrophoresis<sup>5</sup> (DEP). Ultra-sharp probes combined with the refractory nature of tungsten enable many novel developments in nanoscience.

However, tungsten probes are often used in applications where the unusual combination of electrochemical and fluidic effects required to sharpen them are entirely unrelated to the task they are performing. Hence, many researchers are not well equipped to reliably obtain these essential tools to perform their work. They either depend on third-parties to provide these probes, or must develop their own resources – whilst taking away precious time from the actual research they wish to perform. Furthermore, these probes are consumable by nature. It

is inevitable that during interactions at the nanoscale the probes will be damaged, which hinders their ability to perform nanoscopic research.

The most widely used technology for etching probes to date is known as the “drop-off method”.<sup>6,7</sup> This is an electrochemical etching process that utilizes a necking effect caused by the surface meniscus of the electrolyte. Although the process requires simple apparatus and may be relatively expedient, it is renowned for being unreliable and highly dependent on the operator’s skill to conduct the experiment. It is difficult to control the probe geometry and fundamentally impossible to fabricate multiple probes simultaneously. Many researchers have developed variants of the technique, such as adjusting the electrode shape,<sup>8</sup> withdrawing the probe during use,<sup>9</sup> and utilising tungsten trioxide by-product,<sup>10</sup> in attempts to make the drop-off method more viable. However all variations remain hindered by the fundamental limitations of this process caused by the surface meniscus and necking effect.

Given the important role these probes play in many areas of research it is clear that a new approach must be developed that completely eliminates these restrictive experimental parameters. This approach must improve the reliability, convenience and address the volume of tungsten probe fabrication.

It has been established that tungsten probes are instruments that allow researchers to bridge the gap between the nanoscopic and macroscopic worlds. However, this principle of “bridging the gap” is also becoming increasingly important for nanomaterials too. Since their (re)<sup>11</sup>discovery<sup>12</sup> in 1991 there has been a surge of interest in Carbon Nanotubes (CNTs) due to their remarkable characteristics. Their mechanical, thermal and electronic properties<sup>13</sup> are often far superior to that of conventional materials and promise to enhance existing technologies whilst creating a variety of new ones - but only at the nanoscale. Many

researchers have attempted many different methods to grow or assemble nanotubes at the macroscale.<sup>14,15</sup> However, their highly sought after properties still remain orders of magnitude out from their theoretical potential.<sup>16</sup> The challenge to exploit carbon nanotubes at the macroscale will form the basis for one application of the tungsten probes. This area of research depends on very different natural phenomena to the electrochemical etching of tungsten probes. However, the practical experimentation with CNTs will demand consistent tungsten probe production. This will be a ‘driving force’ behind the invention of a new tungsten probe electrochemical sharpening method whilst simultaneously developing novel research in carbon nanotube technology.

## 1.2 Project Scope

One of the key reasons the drop-off method remains used, yet still found wanting, is because the vast majority of the researchers are applying variations to the same fundamental process. Despite altering many other parameters in the experimentation any improvements still depend on either the surface meniscus which is often fixed by the fluidic properties of the electrolyte, or the drop-off point on the probe which is fixed by the mechanical properties of tungsten.

Thus, throughout this thesis the theme is invention. Simply looking at variants of the drop-off method, or attempting to characterise parameters of the process will not provide the means to fabricate tungsten probes effectively.

This project will follow the development of experiments to produce tungsten probes that meet the aforementioned requirements. It will also show how these developments lead to variations of their own, allowing for many more improvements and applications beyond nanoscience

research. Furthermore, this project will utilise these probes for research into carbon nanotubes threads leading into the new development of “Arc Assembly” - a process which would have been challenging to develop without the initial invention of tungstate sharpening.

### 1.3 Thesis Structure

Given this thesis’s focus on novel invention, the chapters will largely focus on experimental progress, with theoretical background, characterisation and modelling used to inform the development of such experiments. The following summary of each chapter outlines the key areas of experimental development and how this work contributes to the thesis and academia in general:

**Chapter 1** *Introduction* explains the necessity and relevance of the research undertaken. It explores why existing technology is inadequate, and how the approach and solution proposed in this thesis can address the typical problems encountered. It also places into context how each area of the thesis relates to each other as a single piece of work.

**Chapter 2** *Tungstate Sharpening* follows the development of the principal invention of this thesis for fabricating tungsten probes. The fundamentals of the electrochemistry involved are outlined and initial experiments into the drop-off method are shown as well as how the tungstate (the oxidised, aqueous ion of tungsten represented as  $\text{WO}_4^{2-}$ ) layer was first investigated. Analytical techniques such as shadowgraphs and bulk coulometry are covered. The apparatus, electronics and programming required to develop this process are shown. The chapter concludes with the results of this process and further verified for “use in the field” with STM.



**Chapter 3** *Enhancements to Electrosharpening* expands on the work from Chapter 2, increasing the volume of tungsten probes available through a novel liquid-liquid interface approach. The fluid dynamics within the electrochemical system are modelled to show the influence of turbulence and probe spacing. A magnetohydrodynamic effect is also employed to improve the process and also show how tungstate sharpening can be adapted with significant changes in its process parameters. The process is further developed beyond probe structures with a demonstration of how this can be applied to razor blade fabrication.

**Chapter 4** *Arc Assembly* was developed alongside the invention of tungstate sharpening. It initially highlights why methods for developing carbon nanotube threads are sought after and the background theory to dielectrophoresis. A new process is created that allows for the adhesion of carbon nanotubes and characterisation of the material through SEM, TEM, EDX and Raman techniques yield information on how the material is forming. Throughout this chapter the development depends on the use of tungsten probes in a destructive process – with experimental conditions vastly different to those of probe fabrication.

**Chapter 5** The *Conclusion* chapter reflects on the work accomplished and outlines the direction for further developments in the form of *Future Work*. Given the inventive nature of the research, Chapter 5 will put the final results into context within the thesis and towards the goals it has set out to achieve. It will also show that there are many more areas of interest opened up by the work undertaken here.

## 1.4 References

- [1] A. J. Melmed, ‘Recollections of Erwin Müller’s laboratory: the development of FIM (1951–1956)’, *Appl. Surf. Sci.*, vol. 94, pp. 17–25, 1996.
- [2] G. Binnig and H. Rohrer, ‘Scanning tunneling microscopy’, *IBM Journal of Research and Development*, vol. 30, no. 4, pp. 355–369, 1986.
- [3] Y. Ge, W. Zhang, Y.-L. Chen, C. Jin, and B.-F. Ju, ‘A reproducible electropolishing technique to customize tungsten SPM probe: From mathematical modeling to realization’, *Journal of Materials Processing Technology*, vol. 213, no. 1, pp. 11–19, Jan. 2013.
- [4] M. HajjHassan, V. Chodavarapu, and S. Musallam, ‘NeuroMEMS: Neural Probe Microtechnologies’, *Sensors*, vol. 8, no. 10, pp. 6704–6726, Oct. 2008.
- [5] B.-F. Ju, Y.-L. Chen, and Y. Ge, ‘The art of electrochemical etching for preparing tungsten probes with controllable tip profile and characteristic parameters’, *Rev. Sci. Instrum.*, vol. 82, no. 1, p. 013707, 2011.
- [6] H. W. Lee, S. H. Kim, Y. K. Kwak, E. S. Lee, and C. S. Han, ‘The effect of the shape of a tip’s apex on the fabrication of an AFM tip with an attached single carbon nanotube’, *Sens. Actuators Phys.*, vol. 125, no. 1, pp. 41–49, Oct. 2005.
- [7] B.-F. Ju, Y.-L. Chen, M. Fu, Y. Chen, and Y. Yang, “Systematic study of electropolishing technique for improving the quality and production reproducibility of tungsten STM probe,” *Sensors Actuators Phys.*, vol. 155, no. 1, pp. 136–144, Oct. 2009.

- [8] Y. Khan, H. Al-Falih, Y. Zhang, T. K. Ng, and B. S. Ooi, "Two-step controllable electrochemical etching of tungsten scanning probe microscopy tips," *Rev. Sci. Instrum.*, vol. 83, no. 6, p. 063708, 2012.
- [9] A. K. Kar, S. Gangopadhyay, and B. K. Mathur, "A reverse electrochemical floating-layer technique of SPM tip preparation," *Meas. Sci. Technol.*, vol. 11, no. 10, p. 1426, 2000.
- [10] W.-T. Chang, I.-S. Hwang, M.-T. Chang, C.-Y. Lin, W.-H. Hsu, and J.-L. Hou, 'Method of electrochemical etching of tungsten tips with controllable profiles', *Review of Scientific Instruments*, vol. 83, no. 8, p. 083704, 2012.
- [11] S. Iijima, 'Helical microtubules of graphitic carbon', *Nature*, vol. 354, no. 6348, pp. 56–58, Nov. 1991.
- [12] V. M. L. L. V. Radushkevich, 'About the structure of carbon formed by thermal decomposition of carbon monoxide on iron substrate', *Zurn. Fisic. Chim.*, vol. 26, pp. 88–95, 1952.
- [13] Peter J. F. Harris, *Carbon Nanotube Science: Synthesis, Properties and Applications*. Cambridge University Press, 2009, ISBN 9780521535854.
- [14] N. Behabtu, C. C. Young, D. E. Tsentalovich, O. Kleinerman, X. Wang, A. W. K. Ma, E. A. Bengio, R. F. ter Waarbeek, J. J. de Jong, R. E. Hoogerwerf, S. B. Fairchild, J. B. Ferguson, B. Maruyama, J. Kono, Y. Talmon, Y. Cohen, M. J. Otto, and M. Pasquali, "Strong, Light, Multifunctional Fibers of Carbon Nanotubes with Ultrahigh Conductivity," *Science*, vol. 339, no. 6116, pp. 182–186, Jan. 2013.
- [15] K. Jiang, Q. Li, and S. Fan, "Nanotechnology: Spinning continuous carbon nanotube yarns," *Nature*, vol. 419, no. 6909, pp. 801–801, 2002.

- [16] F. Li, H. M. Cheng, S. Bai, G. Su, and M. S. Dresselhaus, ‘Tensile strength of single-walled carbon nanotubes directly measured from their macroscopic ropes’, *Applied Physics Letters*, vol. 77, no. 20, p. 3161, 2000.

# Chapter 2



**Tungstate  
Sharpening**



## Chapter 2: Tungstate Sharpening

### 2.1 Introduction

The electrochemical etching of tungsten to produce ultra-sharp tips has proved an essential process for nano-scale applications from their ground-breaking use to display the first image of a tungsten atom in Erwin Müller's lab.<sup>1</sup> They remain critical for many modern techniques such as scanning probe microscopy (SPM), transmission electron microscopy, cellular studies and dielectrophoresis.<sup>2,3</sup> For each of these applications the tip radius, probe length and shape are important parameters. For instance, in scanning tunnelling microscopy (STM), a short rounded probe is desired to minimize vibrations whilst for general SPM, narrow and longer probes may be preferred to achieve high resolution over rough surfaces.<sup>4,5</sup>

Currently, the most widely used method of performing the sharpening of SPM probes is the drop-off method.<sup>6</sup> This relies on the capillarity of the electrolyte around the tungsten to alter the etching rates of the electrochemical process. The method has many advantages in that it is relatively easy to perform and has well established parameters for achieving optimal results.<sup>7</sup> Various improvements to the technique such as gradually withdrawing the tip and the use of ring shaped counter electrodes allow this method to achieve tip radii on the order of 10 nm. However, the control is very limited as the minimum tip radius<sup>8,9</sup> - and the process in general - is almost entirely determined by the breaking of the tungsten when it drops-off.<sup>10</sup> Many attempts have been made to increase the aspect ratio of these probes by extending the lengths

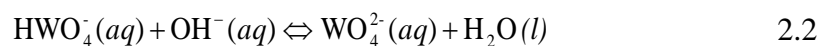
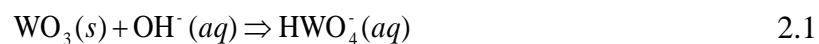
whilst maintaining low tip radii. However, no established means have been developed to produce accurately, and reliably control lengths above 1.3 mm whilst maintaining low conic angles and tip radii less than 15 nm.<sup>11,12</sup>

The work presented in this chapter demonstrates a new method for automatically controlling the tip radii and lengths of tungsten probes up to 4.5 mm, such that any probe shape can be obtained while maintaining low radii. This offers benefits for achieving high resolution microscopy images and also general nano-manipulation in embedded samples whilst simultaneously removing the drawbacks of the drop-off method. Tungsten probes already have a vast range of applications in nanotechnology; the process proposed extends the range even further.

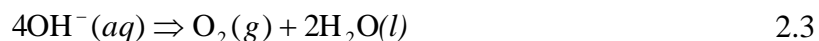
## 2.2 General Principles of Electrosharpening

### 2.2.1 Basic Electrochemical Reaction

The electrochemical<sup>13</sup> etching of tungsten probes follows a series of reactions.<sup>14</sup> Initially the air oxidised outer layer of tungstate reacts non-electrochemically but is accelerated due to the increased concentration of the anodic layer of OH<sup>-</sup>.

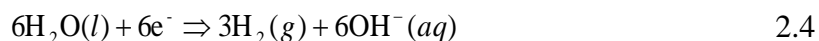


Due to the unavailability of tungsten at the start of this reaction electrolysis of water occurs and oxygen is observed.

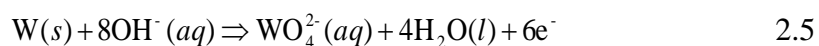


However, the following reactions (4-6) take place once tungsten is exposed.

Cathode:



Anode:

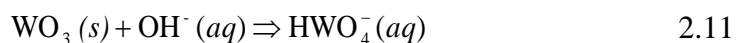
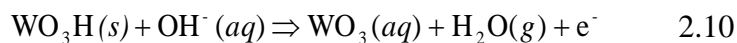
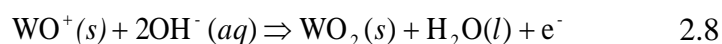
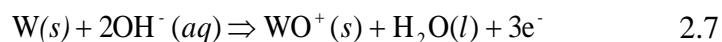


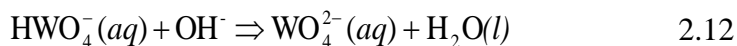
Complete Reaction:



### 2.2.2 Intermediary Steps

Although the reaction may ultimately be shown as the reactants and products via the equations 2.1 – 2.6 the overall reaction mechanism is more complex and the following stages occur from step 2.7 onwards (extensively referenced from Erik Lassner et al<sup>15</sup> page 125. However, one should note some differences, thought to be errors, from Lassner in equations 2.10 and 2.11).





The results of this reaction are that the tungsten anode is etched to  $\text{WO}_4^{2-}$  and  $\text{H}_{2(g)}$  is evolved and escapes at the cathode. For the case of electrosharpening, it is important to consider the rate of the etching at the anode. The rate of etching is determined primarily by the applied voltage, immersion depth and availability of electroactive species.<sup>16</sup>

The  $\text{WO}_3$  precipitate dissolves readily in the KOH solution,<sup>17</sup> and forms a very loose layer over the probe that is often removed as the probe is lifted through the surface meniscus (this was briefly used for its removal instead of various stirring methods). Although the precipitate can cause the process to fail (the composition of this precipitate has not been confirmed), the process may still need stirring to remove oxygen bubbles that can form on the probe's surface. The intermediary reactions show that the production of  $\text{WO}_2$ ,  $\text{WO}_3$  and  $\text{WO}_3\text{H}$  solids may precipitate out as solids under certain conditions in the reaction. However, current literature suggests that any such precipitate observed is  $\text{WO}_3$ .<sup>18</sup> If the composition and the cause of the precipitate were known the amount of stirring may be reduced, or avoided.

\*Note: Although equation 9 is the rate determining step, the process used in the context of this thesis is diffusion limited. That is, the reaction is limited by the availability of the reactants, either from the ions ability to diffuse from the electrolyte or the available surface area of W exposed. This is also experimentally observed by the increase in current via stirring, and the overall tungstate sharpening effect.<sup>19</sup>

## 2.3 Drop-Off Method Experimental Progression

The results of this reaction indicate that the tungsten anode is etched to  $\text{WO}_4^{2-}$  and  $\text{H}_{2(\text{g})}$  is evolved and escapes at the cathode.<sup>20</sup> For the case of electrosharpening it is important to consider the rate of the etching at the anode, which is determined primarily by the applied voltage, immersion depth and availability of electroactive species. Above the redox potential, the applied voltage increases the tendency for reduction/oxidation to occur as the electrons are raised to a higher energy. The immersion depth increases the surface area to which ions can exchange charge.<sup>19</sup>

The key parameter for the drop-off method is the surface meniscus around the anode.<sup>21</sup> This restricts the flow of ions due to the reducing volume of fluid surrounding the anode:  $\text{WO}_4^{2-}$  ions locally increase in concentration and restrict the electrolysis reaction as a negative and non-electroactive species. This is because further from the surface there is a larger volume of fluid for the  $\text{WO}_4^{2-}$  ions to diffuse to. This results in a decreasing etching rate towards the top of the meniscus. Furthermore, the denser tungstate layer flows down and restricts the etching further down the electrode. Therefore, the shape of the meniscus<sup>22</sup> and the ability for the ions to diffuse, determine the sharpening effect of the electrolysis.<sup>23,24</sup> The limitations of this process are that the surface meniscus remains as a fixed shape, and the necking point breaks at a finite diameter based on the mass of tungsten it can support.

As the etching progresses a necking of the tungsten electrode is observed at the surface level of the electrolyte due to the two gradients of  $\text{WO}_4^{2-}$  concentrations and the corresponding gradients of etching. When the diameter of the necking point is low enough: such that the weight of the lower portion of tungsten exceeds the tensile limit of the necking point, the lower portion drops off. At this point, the current drawn through electrolysis rapidly



decreases as seen in Figure 2.1. The DC voltage should be turned off to prevent further etching which would blunt the tip. The remaining sharpened tip can then be removed for use.

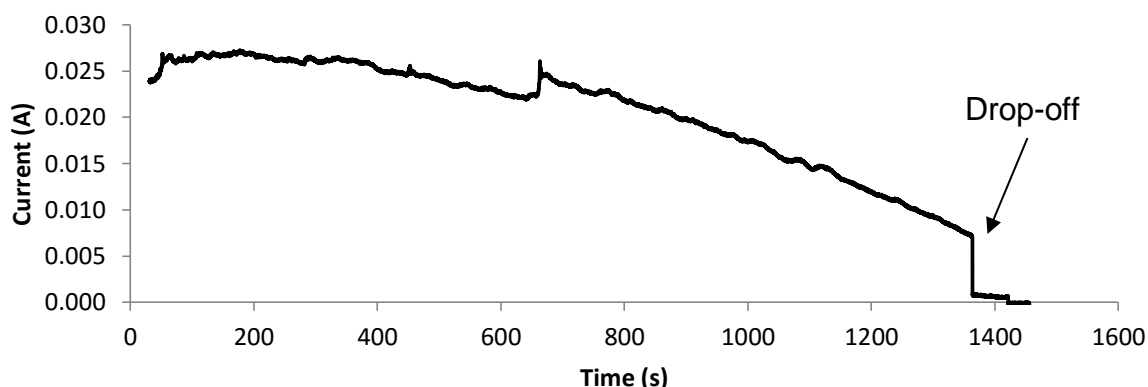


*Figure 2.1.* Bulk Coulometry Graph for the Drop-Off Method, where the step down in current shows where the lower portion of tungsten was removed, lowering the total surface area acting as an electrode.

Current practice of electrosharpening exploits only the shape of the surface meniscus to restrict the layer of tungstate. Aspect ratios are controlled by using features such as a ringed electrode to extend the surface meniscus, immersion depths and concentrations of the electrolyte. In addition, other mechanisms such as decreasing the time between drop-off and voltage cut-off are also used to improve probe characteristics.<sup>25,26</sup> Despite these improvements, the process is still restricted by these 2 aspects of drop-off and meniscus shape. These are ultimately the only elements of the theory being used to define the sharpening geometry. However, it is clear that the formation of the tungstate layer has a distinct sharpening effect on the lower portion of the electrode. Thus, this work will look at utilising just the tungstate layer for electrosharpening. This approach offers the potential to bypass the restrictions imposed by the surface meniscus and drop-off parameters.

### 2.3.1 The Drop-off Method

An example probe produced via the drop-off method can be seen in the SEM image of Figure 2.2. It was etched in 2M KOH at 4 V and was removed immediately at the drop-off point. The SEM images show that it has a tip radius of 90 nm, an aspect ratio of 277 and an overall length of 675  $\mu\text{m}$  from tip to the top of the area of etching.

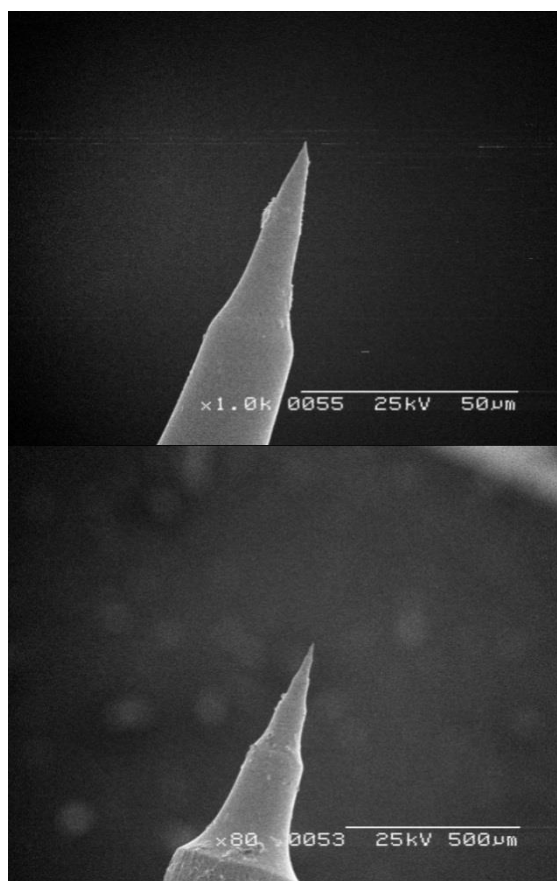


*Figure 2.2.* SEM images of a probe at different magnifications from the Drop-Off Method

Literature findings have quoted probes being used from anywhere between 10-100 nm tip radius. Therefore, 90 nm is within the expected range albeit towards the upper end. 90 nm is probably too high for applications in STM which are typically well below 30 nm.<sup>27</sup> The reason for the slightly higher tip radius is due to the lack of a control circuit to stop the power

supplied to the electrosharpening as soon as possible after the drop off point. Some literature suggests the power cut-off be controlled to under 1 ms.<sup>28</sup> For this experiment, the drop off method was stopped manually. Therefore, the stopping time was estimated to be ~1 second. During the time after the drop-off the tip will continue to be etched which will increase the tip radius until the power is switched off.

In addition, the probe does not exhibit a uniform curvature along its length, a feature also present in the literature regarding the drop-off method.<sup>29</sup> The multiple points of curvature observed are attributable to a shift in the meniscus during etching. Ideally, this should be preventable by reducing vibrations during the experiment. Although this may not appear to influence the shape of the tip, the theory for electrosharpening based on the gradient of the  $\text{WO}_4^{2-}$  down the meniscus suggests, that a shift in the meniscus alters the etching rate down to the tip. The main practical implication of these non-uniformities is the added complexity to modelling the tip and for applications in SPM where the resonance of the tip is an important parameter; these non-uniformities could introduce inaccuracies to such calculations.

Therefore, it can be seen that although the drop-off method is simple and well established for producing nanometre sharp probes, it does have many drawbacks. The restrictions and irregularities caused by the surface meniscus on the overall probe geometry are intrinsic to the process. Furthermore, the drop off point needs to be measured to within a very small time frame to prevent further etching of the tip. In addition, the tip radius is limited by the mass of tungsten that has dropped-off.

### 2.3.2 Angled Electrosharpening

The following experiments show how the tungstate layer and surface meniscus can be further exploited through angled electrosharpening.

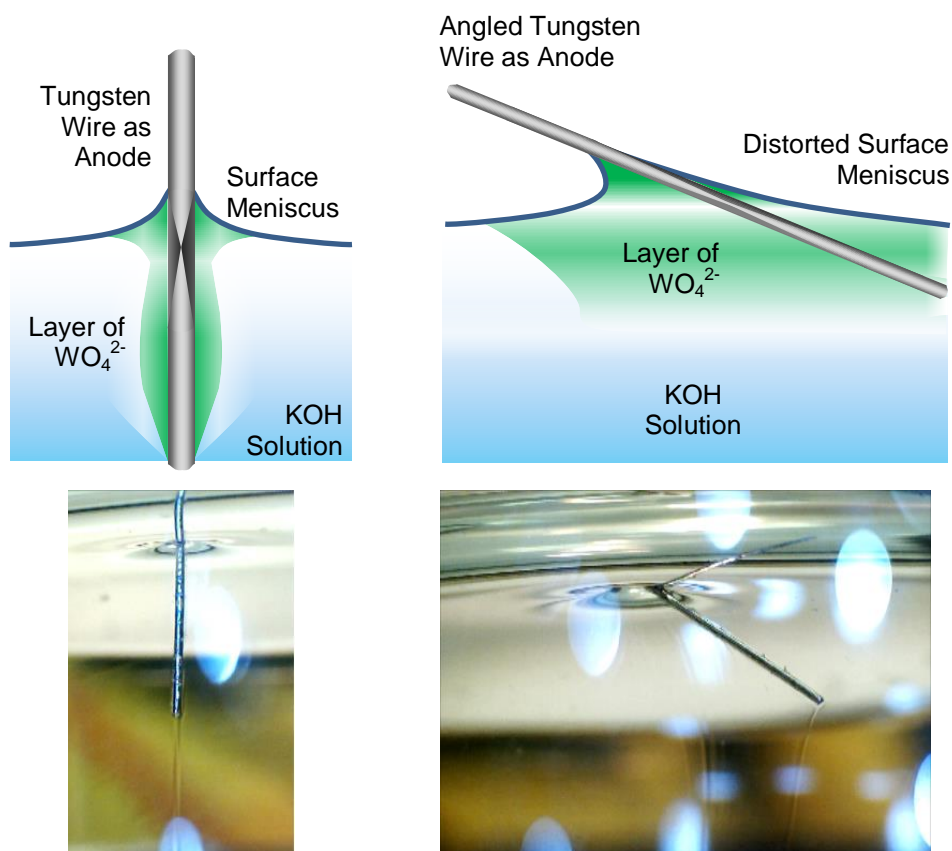


*Figure 2.3.* Left: Tungstate flow for the drop-off method. Right: Tungstate flow on angled electrosharpening. The experimental picture corresponding to each schematic (top) is displayed at the bottom

The layer of aqueous tungstate is denser than the surrounding medium and moves to the bottom of the solution under gravity as a result. This is how the tungstate is primarily removed from the electrode surface. For the typical vertical alignment of electrosharpening this creates a large increase in tungstate concentration as it envelopes and moves down the electrode. As already demonstrated by the current practice of electrosharpening,

this leads to a decreasing rate of electrolysis down the electrode. By immersing the electrode at an angle to the surface of the solution the tungstate will not flow down and envelope the electrode to the same extent as shown in Figure 2.3. The denser tungstate layer is removed by gravity away from the electrode rather than being pulled around the electrode. This reduces the amount by which the tungstate accumulates on the electrode. Therefore a lower *gradient* for the rate of electrolysis occurs.

Due to the fact that the etching rate along the electrode can be controlled directly by altering the angle, higher aspect ratios can now be achieved by reducing the accumulation of the tungstate layer. In addition to this, as the angle of the tungsten anode becomes more parallel with the surface, the drop off will still occur but at a smaller radius due to the mass of the lower portion being smaller due to the increased etching across it.

Figure 2.4 shows results from the angled electrosharpening experiments which demonstrate high aspect ratios and tip radii lower than 50 nm. Thus these experiments show that it could be possible to just consider the tungstate layer when determining probe geometry.

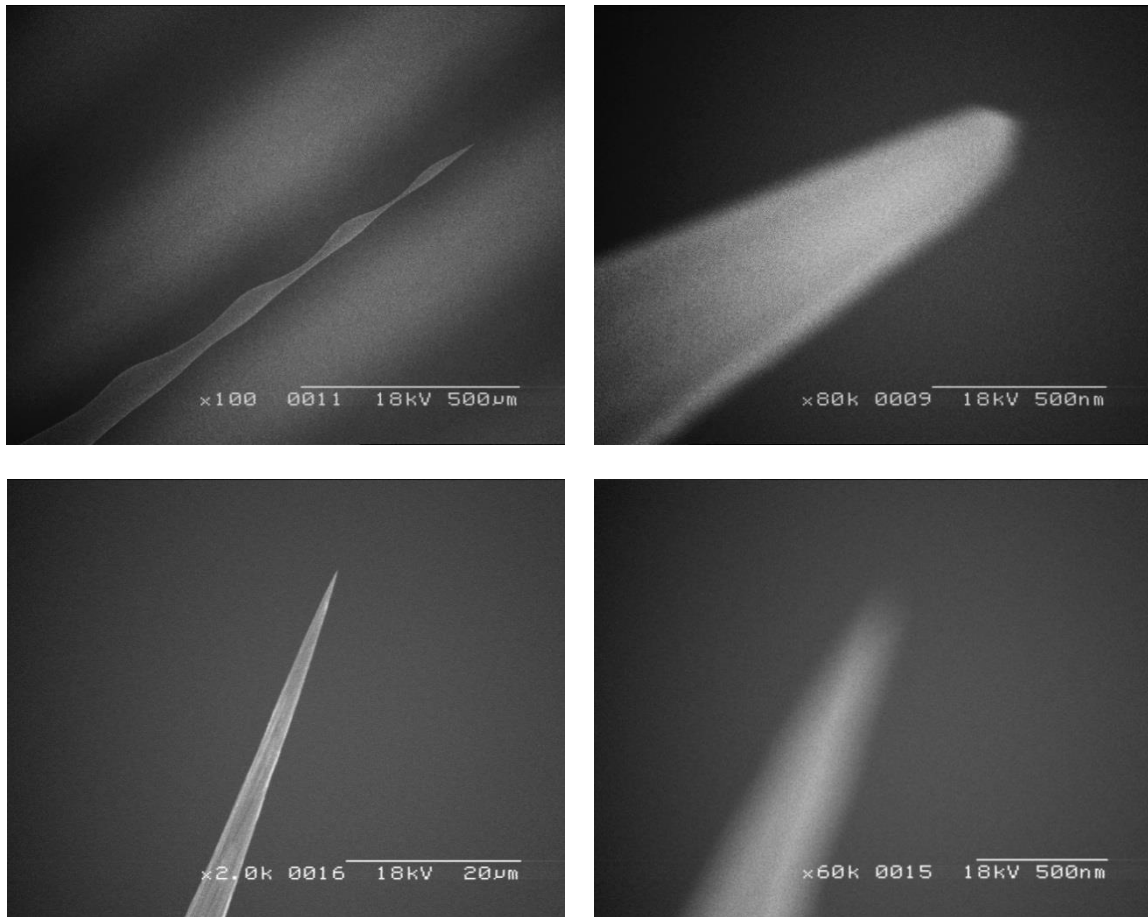


*Figure 2.4.* Preliminary SEM micrographs of 2 probes etched via an angled variation of the drop-off method. (Top row: A probe with necking over probe length and probe tip. Bottom row : A probe with high aspect ratio with no necking and probe tip.)

It should be noted however that as shown in Figure 2.4 some probes experienced a problem of multiple necking points. This was caused by debris, bubbles and tungsten trioxide forming along the electrode and insulating these points from the etching effect. As will be discussed later, this problem can be solved by simply stirring the solution intermittently.

## 2.4 Shadowgraphs

As shown in 2.3.2, the tungstate layer plays a crucial role in the sharpening process. For instance, it has been shown to alter the probes shape simply by varying the orientation of the probe during etching. To further understand how the tungstate layer affects the process shadowgraphs were used.

### 2.4.1 Introduction to Shadowgraphs

The invention of the Schlieren techniques may be credited to the British natural philosopher Robert Hooke in 1665 who observed through a lens the refraction of a candle's heat plume from the light of a second candle. In 1780 the controversial scientist and French revolutionary Jean-Paul Marat published the first known images of a shadowgraph. Now, the techniques have developed into an essential modern methodology for fluid dynamics, including in this thesis for the experimental observation of electrochemical fluidic layers.<sup>30</sup>



*Figure 2.5.* Microscope image of tungstate flow – the lighting conditions which presented this image are unknown

With the use of a digital microscope to control and analyse the experiments it was observed that occasionally the tungstate layer could be viewed under certain lighting conditions as illustrated in Figure 2.5. The effects of the tungstate layer could also be seen often through the downwards movement of bubbles as they are caught in the flow. However, the reasons as to why certain “lighting conditions” allowed the layer to be seen was unknown and these conditions could not be reproduced reliably. Given the essential nature of the tungstate layer in this process, it was deemed necessary to gain reliable footage to confirm its presence and how it behaves during the process which may be useful to find ways for improving the method.

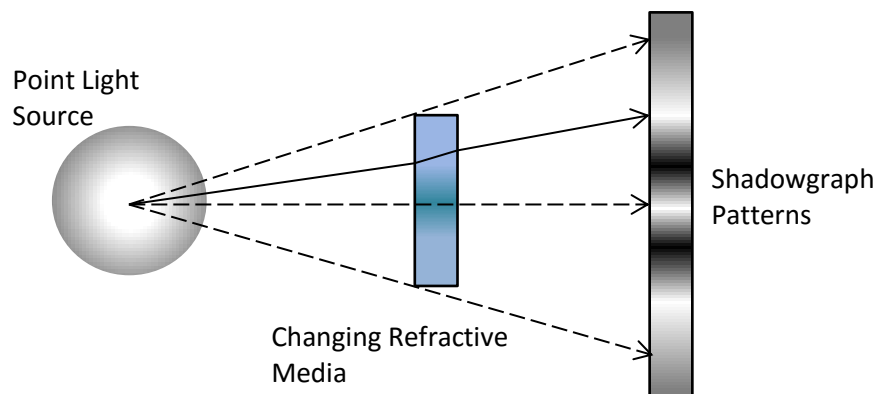


*Figure 2.6. A diagram of a typical shadowgraph pattern*

Common observational techniques used in fluid dynamics are direct shadowgraphs and Schlieren photography. These processes exploit the differing refractive indexes of 2 media to create a shadow contrasted image. This is useful for viewing the movement of fluids where compression or temperature in the fluid changes the refractive index.

Schlieren photography relies on the refractive index shifting the focal point of the image into a knife edge.<sup>31</sup> This blocks the path of the light and creates a shadow on the image where the



different media would otherwise be. Shadowgraphs are much simpler, and use a single point light source. The medium refracts diverging light away from the points on the image that it would normally be illuminated thus creating areas of shadow as shown in Figure 2.6.

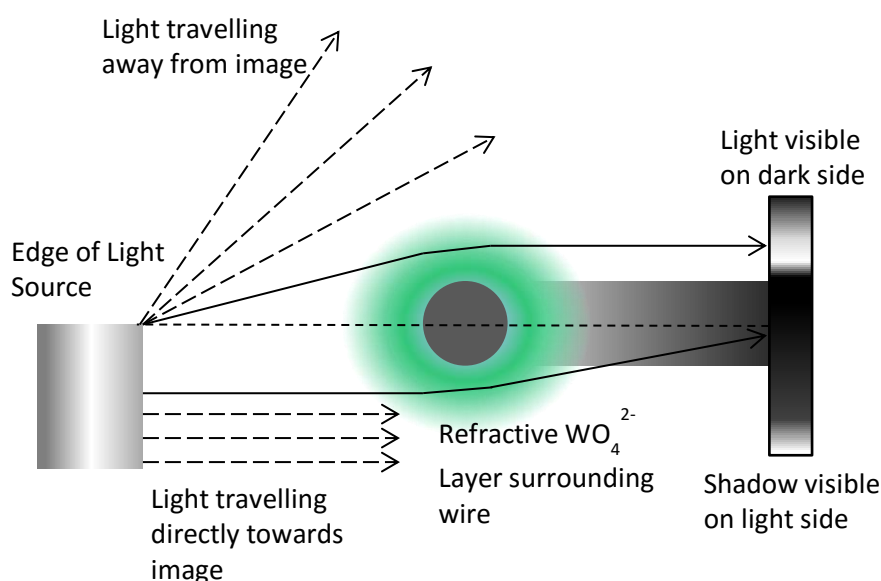


*Figure 2.7.* A diagram of the shadowgraph method used for developing tungstate sharpening

Schlieren photography can potentially create much sharper images than shadowgraphs because it is not as prone to interferences from diffraction. However, due to the simplicity of shadowgraphy and that these experiments are to provide indications and evidence towards the theory rather than any complex measurements - shadowgraphy was the more practical and suited technique. However, despite the simplicity of shadowgraphs, due to the relatively small size of the tungsten probe compared to the point light source (a pin hole through tin foil over a lamp was used), there was insufficient light to provide illumination to the microscope and direct shadowgraphs were not obtained. Instead, a new form of shadowgraph was found during attempts to make direct shadowgraphs work. This was based on positioning the edge of a much stronger light source (the entire filament of the lamp) in line with the centre of the probes width. This resulted in a shadowgraph that still produced shadows with the different

refractive index of the media involved, the KOH solution and the  $\text{WO}_3$  layer but with one side of the probe producing a positive image and the other side of the probe producing a negative. Figure 2.7 depicts how the process is thought to work. Although this is unconventional, the images met the requirements of providing evidence for the tungstate layer and its behaviour.

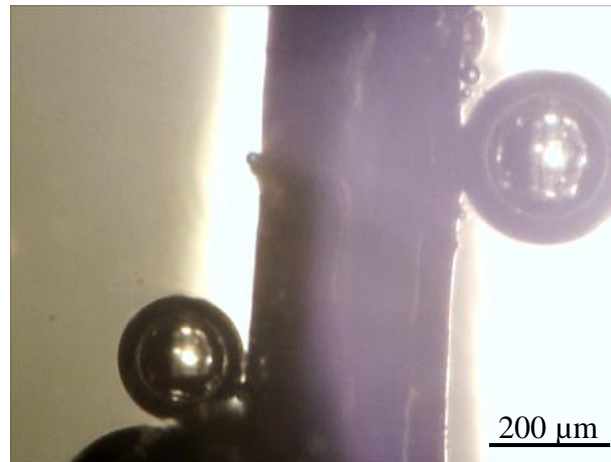


*Figure 2.8.* A tungsten probe during etching. A modified shadowgraph indicates the tungstate layer surrounding the probe in the lighter and darker regions.

Figure 2.8 shows a probe that has just started the electrosharpening process where some oxygen bubbles and tungstate debris still remain attached. On the left hand side of the image the  $\text{WO}_4^{2-}$  layer is illuminated and shows its path down the side of the wire with increasing volume. It can also be noted that a small piece of debris is protruding out and a slight bulge in the  $\text{WO}_4^{2-}$  layer can be seen around it. This suggests that this piece of debris may distort the uniformity of the sharpening process. On the right hand side of the image the  $\text{WO}_4^{2-}$  layer is represented by a shadow. The image shows that the  $\text{WO}_4^{2-}$  is obstructed by a large oxygen bubble and it appears to lose its volume around the probe at this point. After this point, the tungstate layer increases in volume again normally. This would suggest that the oxygen bubble will create a necking point just beneath it if not removed: as this is where the etching

will be increased due to a reduction in the insulating effect of the  $\text{WO}_4^{2-}$  layer. (This is further confirmed by the evidence in Figure 2.11 (A) where it can be seen that without stirring the debris is not removed and leads to multiple drop-off points in the bulk coulometry graphs which are caused by the necking points forming.) In addition, the fact that the  $\text{WO}_4^{2-}$  layer is seen generally increasing in volume on both sides of the probe and also in other images presented throughout this report, provides further evidence for the theory behind this sharpening process.

## 2.5 Principles of Tungstate Sharpening

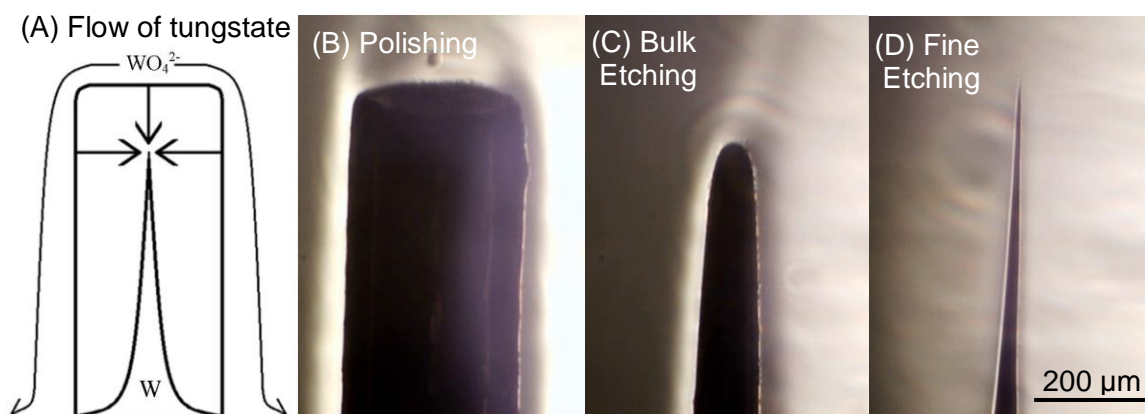


*Figure 2.9.* Shadowgraph images of the  $\text{WO}_4^{2-}$  layer at various stages in probe fabrication. The difference in light/dark areas indicate where  $\text{WO}_4^{2-}$  is flowing as in the diagram on the left, such that the etching converges to a sharp point.

Tungstate sharpening relies entirely on the  $\text{WO}_4^{2-}$  layer flowing down the probes. This layer is visible via the diagram and shadowgraph images displayed in Figure 2.9. The layer accumulates over the probe as it flows downwards and decreases the rate of etching. Thus, a gradient of etching occurs over the length of the probe with the greatest etching at the top and the weakest at the bottom. Figure 2.9 shows how this transitions from a bulk W, Figure 2.9 (B), to a sharp W probe, Figure 2.9 (D). Using this method, sharp and yet longer probes, with

aspect ratios similar to those obtained using the drop off method were produced. The advantage is that the probe can be etched to a sub-15 nm tip whilst at a longer lengths of 4.5 mm and maintain this sharpness to much shorter lengths of 0.5 mm. In addition, it is important to note that the probe shape is not dependent on a single drop-off point but can be altered continuously and requires no mechanical movement to change the length. The whole process is controlled via the electrochemical reaction.

## 2.6 Implementation

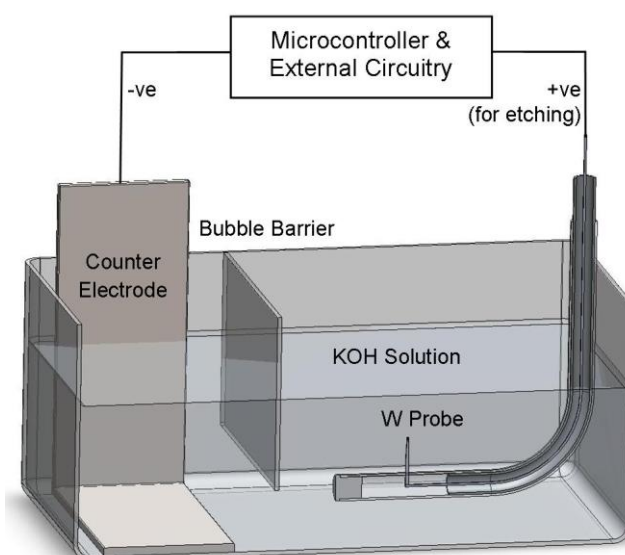


*Figure 2.10.* A cross-section of a 3D model of the tungstate sharpening apparatus. The connection to the tungsten probe is electrically insulated from the KOH. (Refer to Figure 2.15 for complete circuit layout)

The basic set up for the electrosharpening is shown in Figure 2.10. The tungsten wire is the anode and the cathode is a metal that is electrochemically inactive for the voltage range applied - for these experiments stainless steel was chosen. The main difference over the drop-off method is that the electrode must be completely submerged in the solution and pointing upwards. This was achieved by placing the wire through a piece of silicone tubing with rubber O-rings to seal the ends. Both electrodes are immersed in KOH solution; NaOH may

also be used, but has been shown to be less effective by some literature due to the reduced ion mobility and thus the reduced conductivity of the electrolyte. A DC voltage is applied to the electrodes. When the voltage is greater than the summation of the standard oxidation potential, standard reduction potential and electrochemical polarisation, electrolysis occurs, as described in equations 2.1 – 2.6. For the experiments listed here, a 4V DC voltage with a 99.95% pure tungsten wires of 250 - 400  $\mu\text{m}$  diameter in 2M KOH.

A LabView program with an NI 6009 DAC was developed in house to modulate the power and take current measurements. A USB microscope was used for real-time observations and taking time-lapse footage of the process. Shadowgraphs of the tungstate layer were obtained by positioning the edge of a light source behind the tungsten probe. The counter electrode was also partially shielded from the probe with a physical barrier to prevent hydrogen bubbles disrupting the diffusion layer.

### **2.6.1 Control Through Bulk Coulometry**

Another key element of the control is the practical yield of the electrosharpening procedure. Typically a tip formed after drop-off is as sharp as possible; if the procedure is disturbed either through debris or vibrations then the whole probe is wasted and the procedure has to be restarted. Using the tungstate sharpening method the tip can be constantly monitored as it is forming. If the tip is asymmetrical or not sharp enough then the voltage can be reduced or turned off as well as introducing stirring at key points to remove unwanted debris, such as the tungsten trioxide that forms. Figure 2.12 shows an image of some “bulging” on a tungsten probe due to the insulating effect of some  $\text{WO}_3$  on the side of the probe. However, if the debris is removed through stirring, the polishing effect of the etching will erode the protrusion.

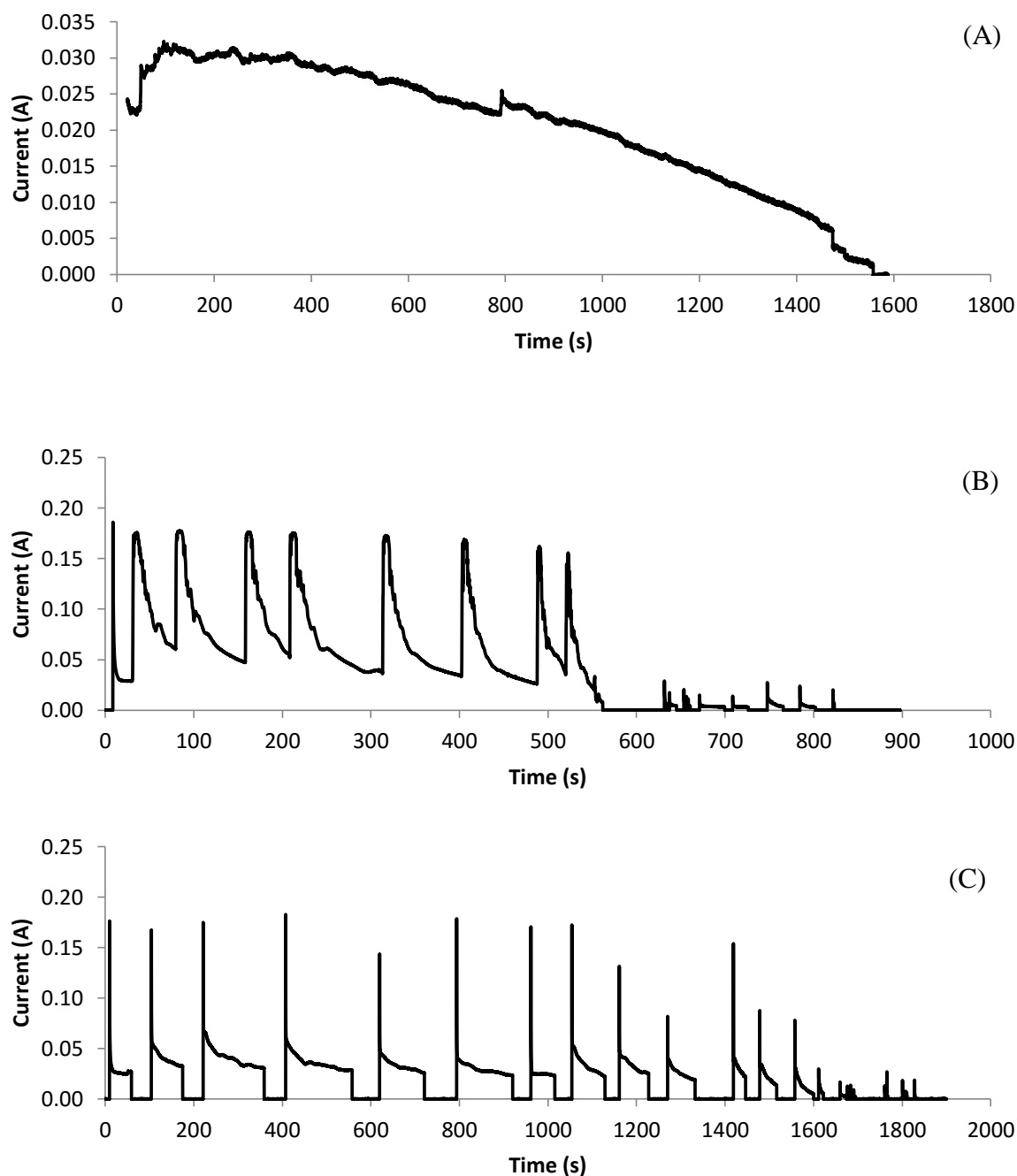


*Figure 2.11* : Bulk coulometry graphs of three different tungstate sharpening regimes used in the development of this process.

- A: with no stirring and no power control
- B: with stirring and manual power control from 600s onwards
- C: with stirring and manual power control throughout process

Figure 2.11 shows three graphs establishing the control of the process using stirring and manual power control. It should be noted that the duration of the stirring is based purely on

inspection of the probe such that it is stirred until debris has been removed by observation. One should also note that the gradual decrease in current is due to the surface area of the tungsten electrode decreasing.

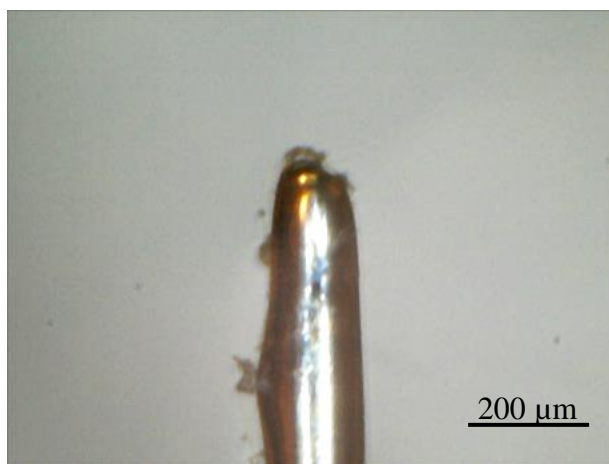


*Figure 2.12.* Bulging due to debris obstructing the diffusion of  $\text{OH}^-$ .

According to a Faradic current, the rate of reaction decreases with the area as fewer ions have space to diffuse through to the electrode. In A) the probe was allowed to be etched till the process stopped simply due to the tungsten being completely removed. It should be noted that this results in “minor drop-offs” at the 1500 second mark onwards as the wire width becomes too thin to support its own weight and that of the debris attached. This indicates that the control allowed in this process is both useful and essential given that the purpose of this method is to avoid drop-off completely. In (B) and (C) however, the process was controlled with the voltage being switched on and off towards the end of the process to avoid these smaller drop-offs and to create the probe and tip shape desired.

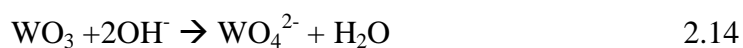
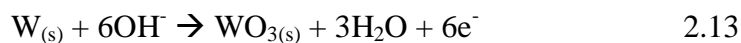
## 2.6.2 Observations of Tungsten Trioxide



Figure 2.13. Three images showing WO<sub>3</sub> formation and progression to probe collapse.

During the process of tungstate sharpening it was observed that a fine ‘mesh’ of material formed down the wire when the wire approached thickness of around  $\sim 70\mu\text{m}$  (for a 4V supply with 2M KOH). The mesh can be seen in Figure 2.13.

This mesh is thought to be tungsten trioxide (WO<sub>3</sub>). This is due to its apparent yellow colour, *(it should be noted that the first image was illuminated by a yellow lamp therefore may be misleading in this case)* and this is typically associated with tungsten trioxide. Tungsten trioxide is prevalent in the electrochemical reactions as an intermediary state before forming tungstate ions:



It is suggested, that as the volume of the electrolytic diffusion layer reduces with the decreasing diameter of the electrode, the concentration of tungsten trioxide increases to a saturation point where it then starts to precipitate into the solution around the electrode.



In general, the formation of tungsten trioxide can make the tungstate sharpening unreliable if not addressed. It produces necking points as observed in the angled sharpening due to electrical insulation and adds non-supporting weight to the structure. As shown in Figure 2.13 this can ultimately lead to a premature collapse of the tungsten probe. Figure 2.13 also gives an indication towards the extent of this growth: a column of  $\text{WO}_3$  which had been forming down the whole electrode falls past the camera as the top portion of the electrode collapses under the excess weight. A time-lapse video of this occurring during the first test of tungstate sharpening can be found in the appendices.

However, this problem is easily solved by simply turning the power off momentarily and stirring the solution to remove any mesh forming. Stirring may also be performed during the electrolysis to allow more tungsten trioxide to react with  $\text{OH}^-$  as the double layer is disturbed. However, as discussed, this will have the effect of increasing the rate of electrolysis and possibly symmetry.

One possible advantage of this tungsten trioxide formation is that there is a wide range of recent research conducted on the production of porous tungsten trioxide layers and its various applications due to its remarkable photoelectrochemical, ‘gas sensing’ and catalysing characteristics. So far, attempts to extract this tungsten trioxide layer have been unsuccessful as it is removed from the electrode by the surface of the solution as the electrode is withdrawn. However, this is just to note that this otherwise ‘unhelpful’ debris may offer a possible alternative to producing tungsten trioxide.

## 2.7 Automation Programming Concept

Initially investigations into the drop-off method and the tungstate sharpening experiments were performed as a manual process, where the user regulates the power whilst visually inspecting the wire via a microscope in situ. This created a great restriction on the drop-off experiments, as any etching that continues after the moment of drop-off blunts the tips. This restriction may also be attributed to the development of tungstate sharpening, which may continue etching once a sharp tip is obtained so manual fabrication would not be detrimental to this key feature.

Despite the nature of tungstate sharpening allowing for manual control, other advantages of the process could not be realised without full automation. Manually controlled experimental results showed that the length could be controlled beyond that of the drop-off method. However, the accuracy of the length was difficult to ascertain under a microscope, where it is technically difficult to view the dimensions of the tip and the entire length of the probe simultaneously. In addition, although timing is not as critical for achieving a tip radius below 100 nm timing is still critical to obtain an accurate length. Further practical benefits are gained as the process duration is between 15 – 60 minutes and the user would have to maintain attention throughout that time.

Overall, with automation it became possible to:

- Measure the current of the process as bulk coulometry.
- Infer the length of the probes etched.
- Stop the process without the need for user intervention or attention.
- Implement additional processes such as stirring/pausing.

- General improved reliability with timing of the experiments.
- Record data in situ.
- Inform user of progress.
- Faster experimental through-put.

These advantages over manual control all became requirements for the actual program constructed. To implement these requirements LabVIEW was chosen as the programming environment for the automation, the reasons for this are listed below:

#### Advantages of using LabVIEW

- LabVIEW is a concurrent language, so multiple processes can be handled simultaneously. This is useful for automation as data from an experiment can be acquired whilst changes are made to the experiment at the same time.
- It is designed for interfacing with instrumentation hardware, and in addition to this National Instruments provides many off-the-shelf devices specifically designed to function for experimental work from the LabVIEW environment.
- LabVIEW also comes with extensive libraries and a platform for constructing graphical user interfaces (GUI) which enables quick development of a usable program, and time is only spent developing the automation.
- LabVIEW is written with a graphical source code that relies on “data flow” connections between objects within the program. This makes it intuitive to see how the automation is running in a sequence as well as allowing the logic of the program to be more accessible and understandable to those not familiar with the language.
- LabVIEW incorporates a large library of functions and tasks that are pre-constructed and typical for automation projects, i.e. writing data to text files and their location within a computer is all incorporated into a single object available with the program.

### 2.7.1 Software Implementation

The program was developed over 25 iterations, from an initial program that could only display current measurements and execute a fixed sequence of control without any feedback to a program which meets all the aforementioned requirements through the sections outlined in more detail below. Due to the complex nature of the program it may be useful to refer to the Appendix for the full details of the program's operation.

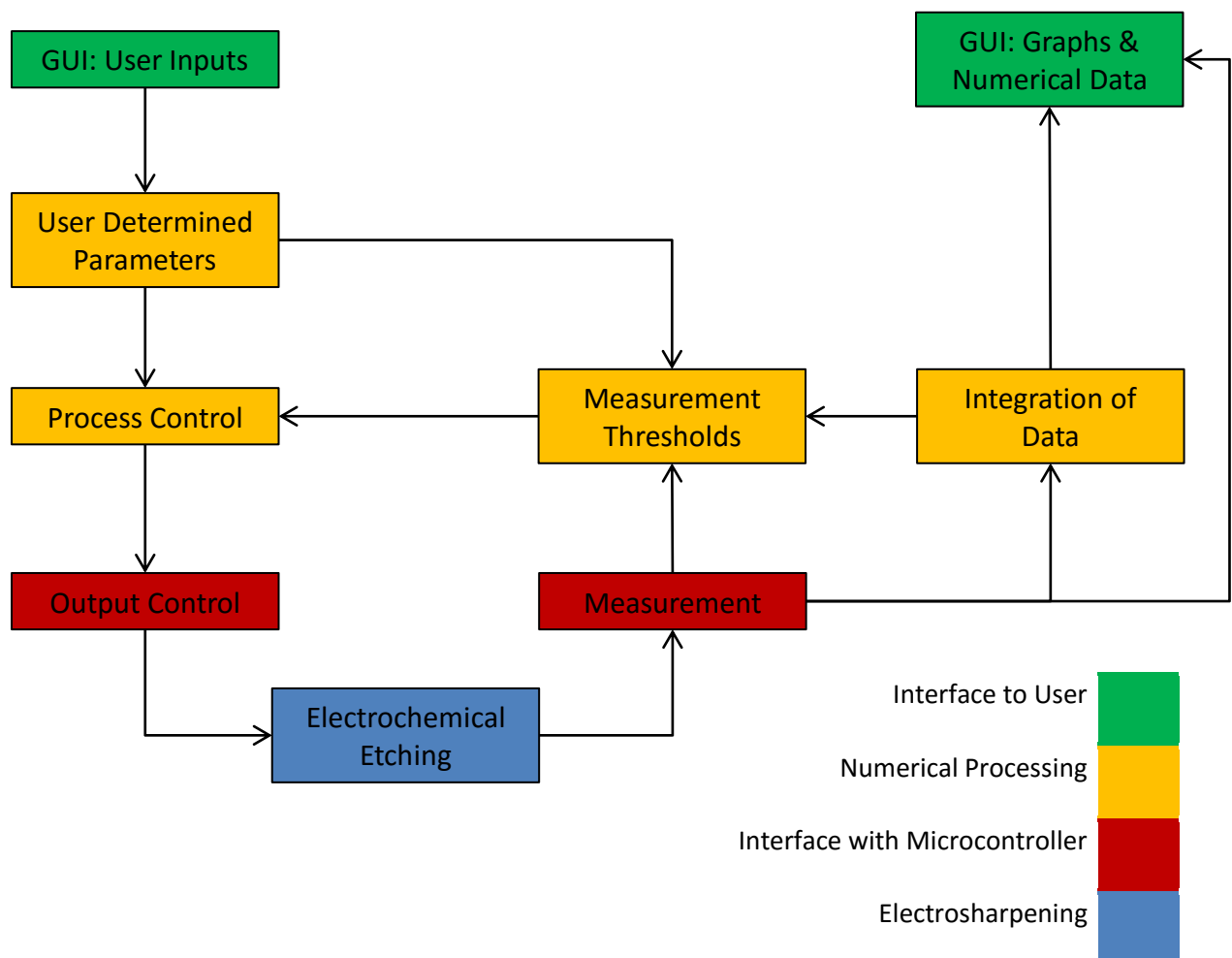


*Figure 2.14.* A program map for all the main LabVIEW sub-sections that allow complete automation over electrosharpening

## 2.7.2 Automated Electrochemical Circuitry

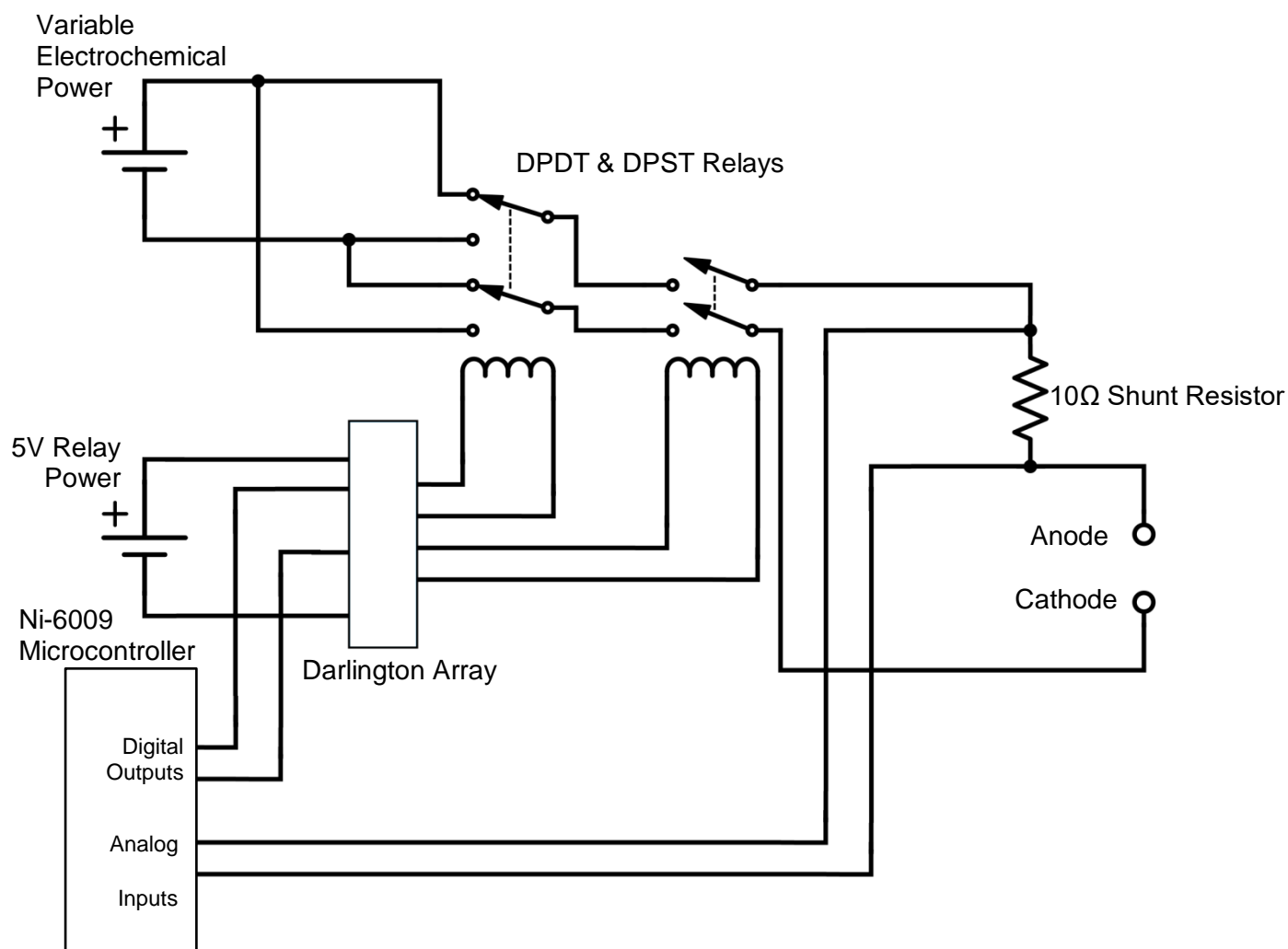


Figure 2.15. Electrochemical Etching Circuit for Automation

The automated system uses a combination of Darlington arrays<sup>31</sup> and relays in between the microcontroller and the electrochemical apparatus. This setup keeps the electrochemical system as isolated as possible with the exception of a single 10  $\Omega$  shunt resistor (independently measured to  $9.9 \pm 0.05 \Omega$ ) which is necessary for current measurements. If any components are placed alongside the electrochemical system it can distort the equilibrium established during the reactions.<sup>32,8</sup>

The NI-6009 microcontroller connects the digital outputs to the darlington array logic which uses a separate powersupply to drive the relay switches which can supply a forward or reverse bias, and also turn the power on and off. The analog inputs of the microcontroller is placed over the shunt resistor which is adjusted for in the LabVIEW software. The relays are used instead of IC switches to prevent possible inaccuracies being introduced to electrochemical measurements (i.e activation voltage of any semiconductive switches would distort the electrochemical equilibrium) with potential semiconductor switches (such as those in the Darlington array) The relays introduce the greatest delay circuit, rated at a maximum of 8ms. However, as the program is typically operating with a sample rate of 4 Hz, this has minimal effect on experimentation.

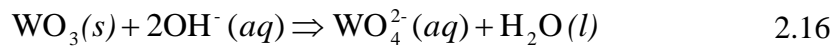
Future improvements to this circuit would include a lower shunt resistor, which in turn, requires a microcontroller with a greater resolution. A lower shunt resistor would allow for closer data sampling to the actual electrochemical reactions, and the rate of etching would increase. Note however, an increase in the rate of etching may not be beneficial. In addition, the two relays could be replaced by a single DPDT centre-off relay. There may also be interest in components to alter the electrochemical equilibrium as an extra parameter to control (and place feedback through.) However, for this thesis the reaction was kept “undisturbed” other than changes to the duty cycle and etching durations so the current measurements were an accurate indication of the actual electrochemical reaction taking place.

## 2.8 Automated Electrosharpening

A uniform DC current cannot be applied for tungstate sharpening to work reliably. Instead, the power and polarity must be modulated over the course of the etching to prevent a build up in gaseous bubbles and excess tungsten trioxide ( $\text{WO}_3$ ). Initially, an automated stirrer was used. However, this was found to increase the duration of etching as a lead time had to be observed to prevent fluidic movement from distorting the diffusion layer. As an alternative, the power is reversed, and with an electrochemically inert electrode hydrolysis will occur as in equation 2.15 where hydrogen bubbles “clean” the probe.



A precautionary separate variable resistor or other current limiter in the reverse state was used to ensure that the potentially high current drawn (greater than 0.25A) by hydrolysis does not damage the probe. Note that a thin outer layer of  $\text{WO}_3$  is formed as part of the cathodic reaction, but is etched away in the following non-electrochemical reaction afterwards in equation 2.16. This method also removes the disadvantage of having to perform an initial etch on the probe as is frequently the case in the drop-off method via equation 2.16.



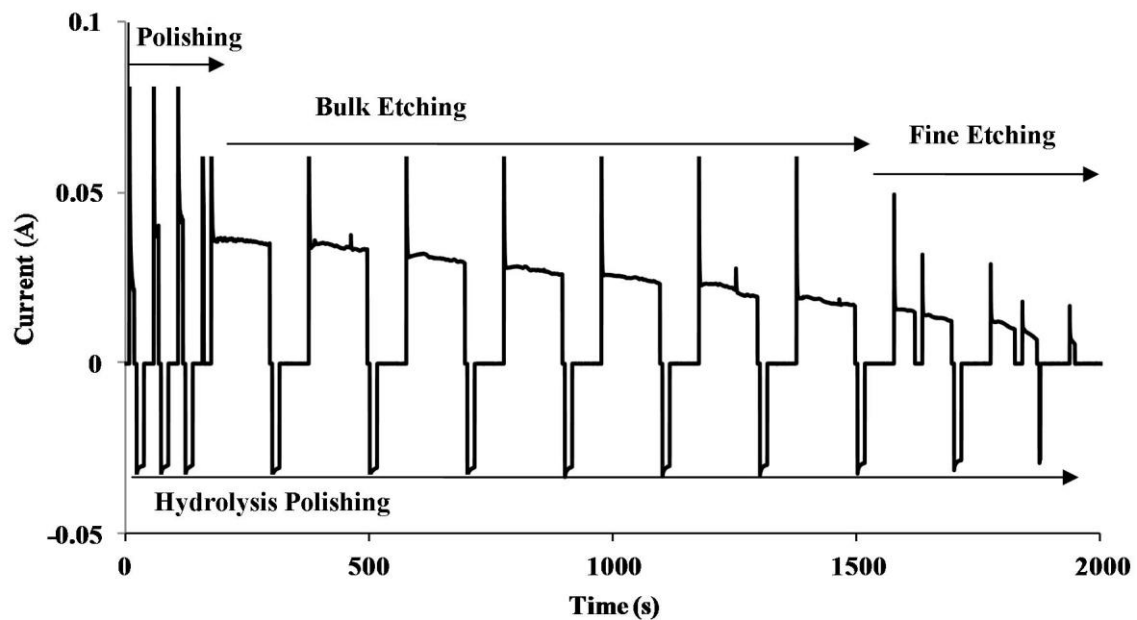


Figure 2.16. Automated current analysis of typical tungstate sharpening with various etching regimes.

- The spikes on the graph are from the accumulation of the diffusion layer forming
- This still adds to the etching, and is accounted for with bulk coulometry, and the removal will simply be at an increased rate.
- However this is likely not governed by the tungstate layer (so uniform sharpening – which puts a limit on the minimum amount of time an etching pulse can form)
- However there may be circumstances when uniform etching is desired, especially after the overall profile of the probe has been formed.
- i.e. an etching regime that was a fast duty cycle up to 1 second would etch as if the tungstate layer was not formed.



A current versus time graph of a typical tungstate sharpening process is shown in Figure 2.16. The timing for the sequence is not predetermined. Instead, a sequence within the developed LabView program is triggered to change at set thresholds at which the current measurements falls above or below. The thresholds determine the progress of the etching for a given surface area of the probe, and hence the current decreases as more material is removed as shown in equation 2.17. For a 2M KOH solution at 4 V these thresholds typically range from 50 mA down to 2.5 mA. The final threshold which the user sets determines the final probe shape and is the minimum current before the probe stops etching. The sequence is designed to etch for the appropriate length of time for a given stage in the fabrication of the probe. Note that during the polishing regime, the current is increasing, as the outer layer of  $\text{WO}_3$  is stripped and a greater surface area for the general reaction is exposed. The bulk etching regime is designed to remove as much material as possible whilst not creating irregularities along the probes length. In turn, the fine etching regime is designed to minimize the hydrolysis stirring required and etch in short steps to ensure an accurate probe is obtained when approaching the final current threshold. As shown in Figure 2.16, the program can automatically select the time of etching required for various stages in the probes manufacture. The program utilizes the normalized form of Faraday's equation which introduces the proportionality between current and total area of the probe.

$$i = nFAv \quad 2.17$$

where  $i$ ,  $n$ ,  $F$ ,  $A$  and  $v$  are the current, number of electrons transferred, Faraday's constant, surface area of the electrode and rate of material removed per unit area.

Thus, the thresholds are determined by two possible criteria: either a current reading or the calculated total charge transferred during the process. The accuracy of each of these is

fundamentally affected by different starting conditions. For the current reading the concentration and voltage must be known - but is independent of the mass of tungsten used. Conversely, with the summation of charge transferred, knowledge of the initial mass of tungsten immersed is required to calculate the total material removed, and hence the probe shape. However, assuming no faradic losses this measurement is independent of the concentration.

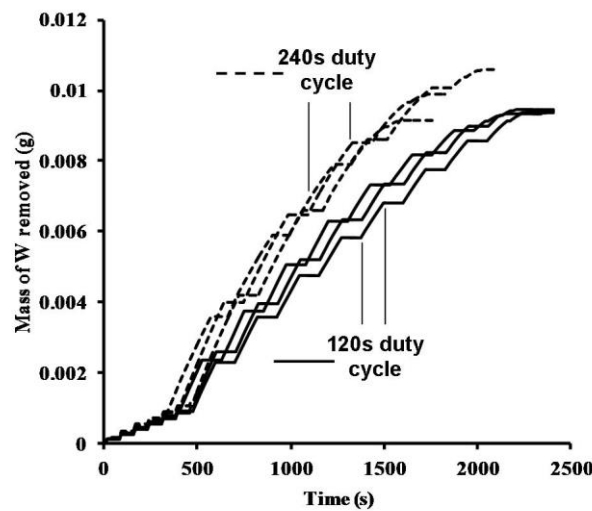


*Figure 2.17.* Coulometric graph of tungsten removed for 2 different duty cycles showing repeatability.

Typically, the thresholds are determined by the current measurement, as this allows for probes to be immersed at different lengths and etched to a given surface area. However, the coulometric measurements can give a strong indication of the reliability. Figure 2.17 shows two sets of three probes all immersed to 5 mm in length, and etched to the same area value with different duty cycle times in the bulk etching regime.

The importance of using the correct duty cycle for the power is also evident from Figure 2.17. With half the bulk etching time at 120 s, results spanned a range of 0.08 mg; 0.85% of the average mass lost. However, at 240 s, the data spanned a range of 1.46 mg; 14.8 % of the average mass lost. The reason for this difference is that the probe will develop varied surface asperities along its length due to irregularities forming with inadequate cleaning. This causes the probe to break during the fine etching regime, which prevents accurate measurements and control over the later stages of its fabrication. However, the duty cycle of 240 s is faster in about ~1800 s whilst the 120 s duty cycle takes ~2200 s. Thus, if reliable control is not required for a rapid and large production of assorted probes, this type of process is still viable.

### **2.8.1 Tip Radius**

This parameter defines the radius for the best fitting circle as drawn over the tip's apex as shown in Figure 2.18. For this project the tip radii and all other characteristics listed below, are measured from an SEM image using ImageJ software. ImageJ is a program that interprets image data to allow measurements to be taken based on a calibration from a known scale of the pixels in the image. The accuracy of these measurements, particularly in nanometre ranges may not be entirely reliable due to limited calibration and resolution of the SEM used, as well as human error from applying a best fitting circle. This is why an emphasis is placed on utilizing these probes within experimental environments where their sharp tips are essential, as this confirms the probes ability to fulfil their roles in nanotechnology.

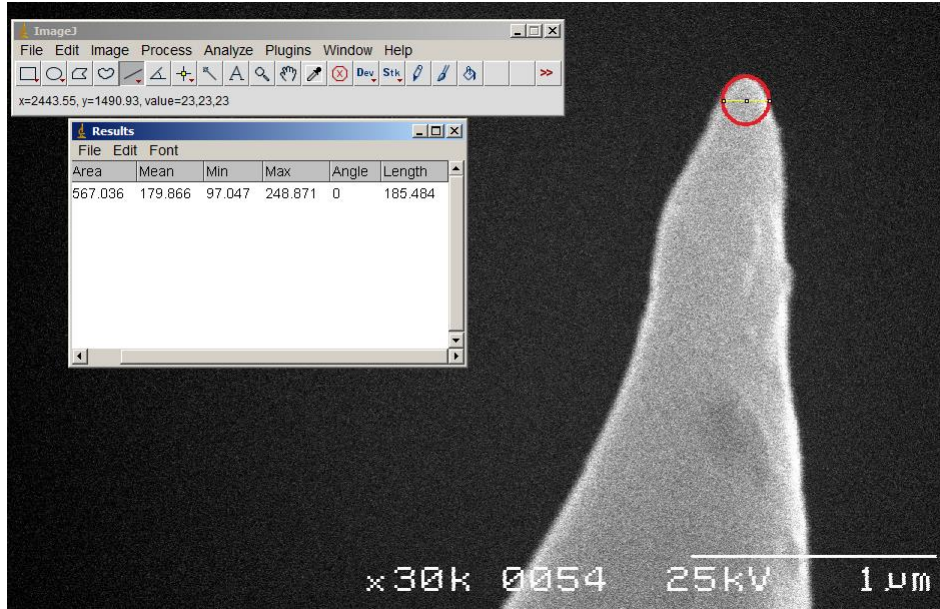


*Figure 2.18.* Demonstration of ImageJ used to measure SEM tip radii from drop off method tip

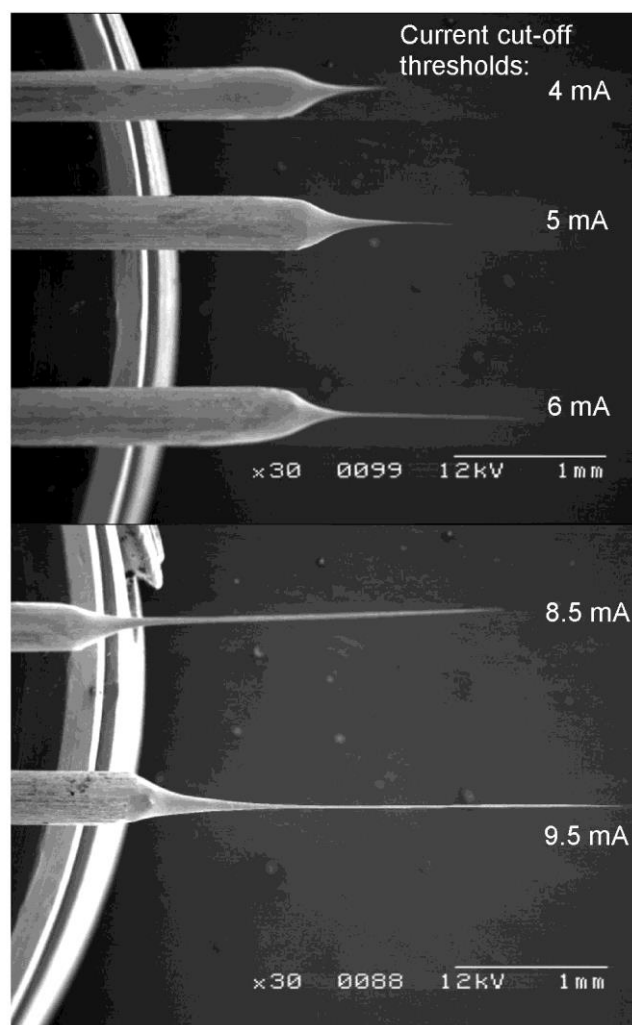
Typically it is the tip radius that defines the sharpness of the probe. As shown from the theory behind dielectrophoresis and in the COMSOL models, the radius determines the gradient of the electric field – which plays a critical role in Chapter 4 of this thesis.

## 2.8.2 Overall Tip Length

Given the aspect ratio for this project is defined from a fixed length, the need to define the overall length of the etched probe must be clarified beforehand. By stating the overall length of the probe the aspect ratio for a given application with a different effective length will be obtainable. This characteristic may be useful for applications other than this project, e.g. probing cellular structures or manipulating nanoscale objects within fluids where a greater probe length is required to reach through larger volumes of tissue.

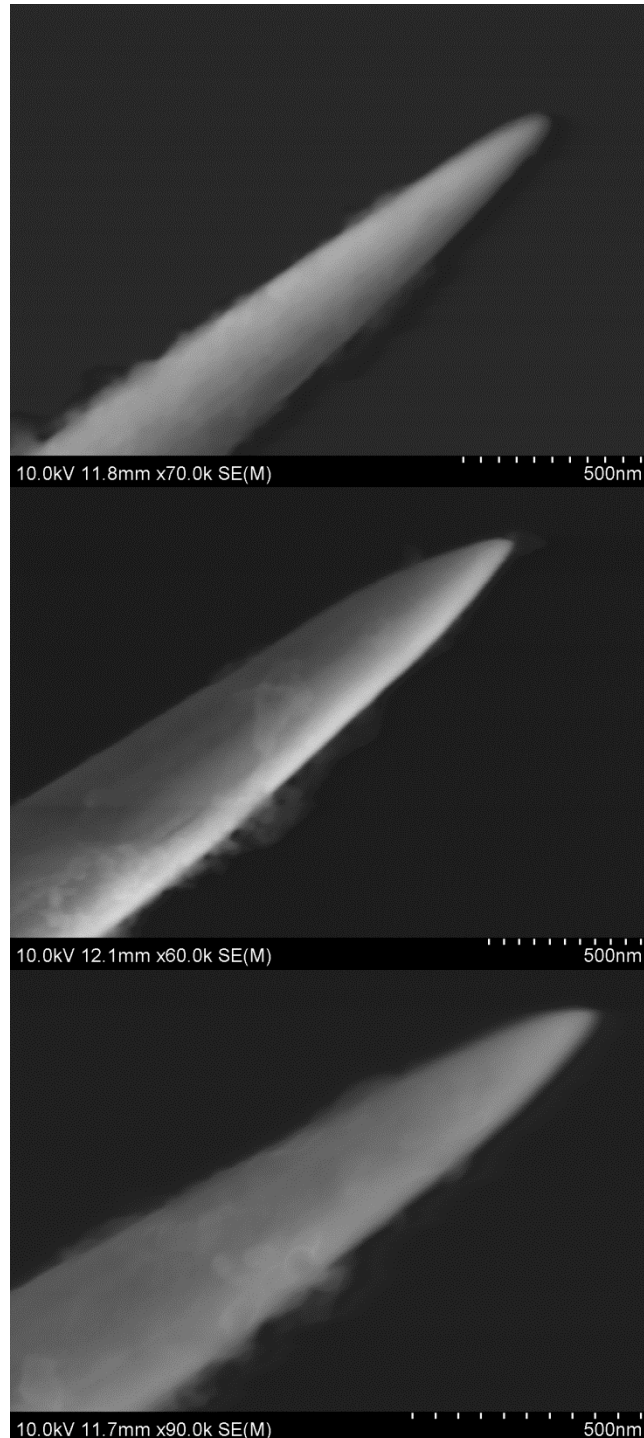
## 2.9 Probe Geometry

Figure 2.19 shows a selection of the types of probes which were obtained using the tungstate sharpening techniques. The overall probe lengths may range from 0.5 mm to 4.5 mm, with tip radii between 15 and 20 nm and a minimum conic angle of less than  $1^\circ$ . Figure 2.19 illustrates the uniformity of the probes suggesting that no mechanical weaknesses are present due to necking points or asperities. All results were measured using a scanning electron microscope (SEM) with magnification scales down to 500 nm.



*Figure 2.19.* The typical range of lengths for short and long probes, their overall profile and the respective cut-off currents.

In addition, three probes were also etched for high resolution SEM images to examine the probe tips seen in Figure 2.20. All the probes achieved tip radii  $\sim 20$  nm. The material observed along parts of the probes is expected to be  $\text{WO}_3$  either as a residue from the etching process or from oxidation in the air.



*Figure 2.20.* Tungsten probe tip profiles. The fuzzy material along the structures is  $\text{WO}_3$

### 2.9.1 Bulk Coulometry Calculations

To establish further control over this process the recorded current was compared to the amount of observed material removed from the tungsten probe. Figure 2.29 shows a current-time graph for an example process which also uses stirring and intermittent etching. By calculating the charge transferred under one of the periods where etching was taking place, in this case integrating from 1359 - 1625 s, we can calculate the expected material removed based off electrical measurements.

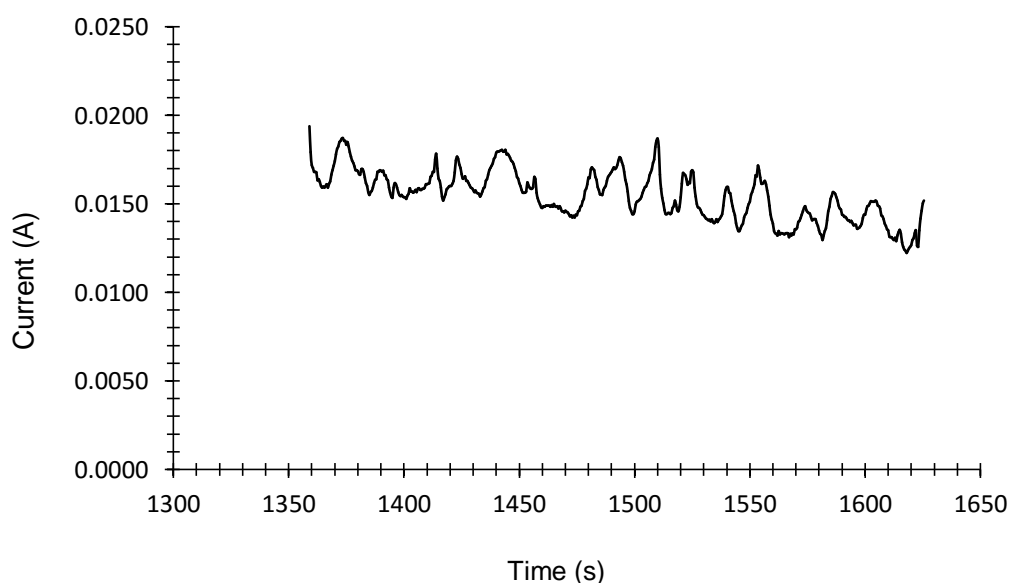


*Figure 2.21.* Extracted portion of a bulk coulometry graph during a fixed period of etching.

The total charge was calculated by integrating under the section of the graph from 1359s to 1625 s using the trapezium rule between points (Note, this is the same method used by the automation program described in 2.7.4):

$$Q = \int_0^t I(t) dt \quad 2.18$$

$$Q = \frac{Current_t + Current_{t+1}}{2} \times dt_{measurement} \quad 2.19$$

= 4.12 Coulombs over a 266.5 second period

Using Faraday's Equation:

$$Q = nFM \quad 2.20$$

Where Q, n, F and M are total charge transferred, moles of electrons exchanged, Faraday's Constant (96485 C/mole) and moles of reagent respectively.

$$M = 7.12 \times 10^{-6} \text{ moles}$$

Multiplied by tungsten's molar mass of 184:

$$184g/mol \times 7.12 \times 10^{-6} \text{ moles} = 0.0013 \text{ g of tungsten}$$

### **Calculations based from Observed Dimensions**

Weight analysis is not a viable method for ascertaining the accuracy of the etching process as the amount of material removed typically lies significantly within the accuracy of readily available balances. However, the following method based on observed dimensions shows that a close approximation can be made by inferring characteristics of the probe. This example of the observational method only works whilst the probe can be approximated to a cylinder, in theory. However, it could still work if accurate imaging is available and the volume of the probe can be estimated. Its accuracy is determined by that of the estimated volume and how close the density of the tungsten matches the theoretical value.





*Figure 2.22.* A probe shown in two different stages of etching. The difference of the diameters can be used as an alternate indication of the material removed.

Left: Width of probe before 1350s: 265 $\mu$ m

Right: Width of probe after 1600s: 204 $\mu$ m

The tungsten probe was measured from stills on ImageJ at times before and after the 1350 and the 1625 second mark of an electrosharpening experiment.

Widths: Before 1350 s = 265  $\mu$ m

After 1625 s = 204  $\mu$ m

The height of the probe was measured before the experiment to be 3 mm a series of ImageJ stills confirm the height of the probe to be 3.3 mm (the size of the probe measured before the experiment was to an accuracy of  $\pm 1.5 \mu$ m (the size of pixels from the digital microscope).

Density of tungsten at room temperature: = 19.25 g/cm<sup>3</sup>

$$dV \times \sigma = \left( \left( \frac{265 \mu m}{2} \right)^2 - \left( \frac{204 \mu m}{2} \right)^2 \right) \times 3 mm \times \pi \times 19.25 g/cm^3 \quad 2.20$$

$$= 0.00129 \text{ g of tungsten}$$

### 2.9.2 Evaluation of Calculations

By comparing to the corresponding difference in size of the probe in Figure 2.22 to the electrical measurements taken, we find that according to bulk coulometry the material lost should be 1.31 mg whilst the observed material lost is 1.29 mg. Both results are very similar. The minor 1.5% difference in these measurements could be accounted for by Faradic losses during the reaction – accounting for more charge drawn for non-sharpening processes, although it must be recognised that inaccuracies during observed measurements are likely far greater than this difference. However, this similarity between 2 different methods of observation does suggest reliability between them. This close comparison of observed material lost with measured current indicates that this process may be controllable using purely electronic measurements.

These results show how this process can be fully automated as current measurements can be used as a good indicator of material removed during etching. This is in contrast to the drop-off method which commonly employs simple automation to stop the process quickly, but has no control over the amount material removed, and thus, no influence on the overall shape of the probe.

## 2.10 Scanning Tunnelling Microscopy Application

Although tungsten probes have a wide variety of applications, the most common is scanning tunnelling microscopy (STM). STM was invented in 1981 by Gerd Binnig and Heinrich Rohrer<sup>33</sup> for which they won the 1986 Nobel Prize in Physics. This instrumental method utilizes the phenomenon of quantum tunnelling between a probe tip and a sample as the tip is scanned across the surface of the sample. The information from the tunnelling current allows a topographic image of the surface to be obtained at atomic resolution. The basic setup for STM may be seen in Figure 2.23:

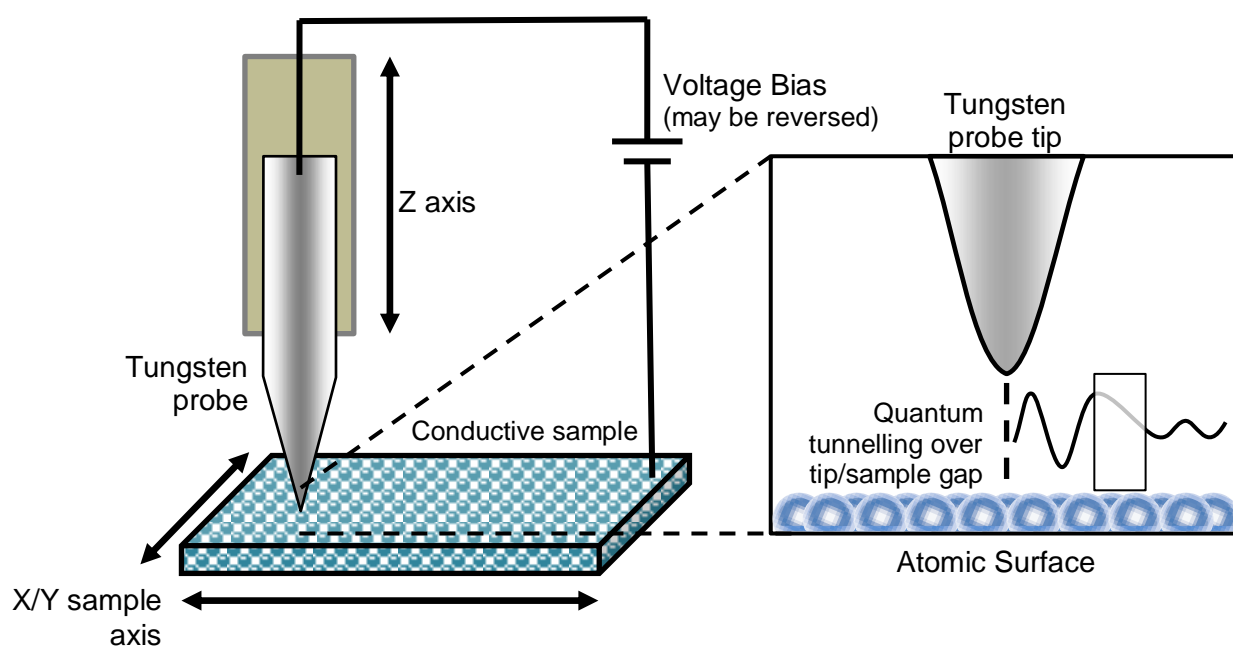


*Figure 2.23.* The basic setup for STM: A sharp probe utilizes a tunnelling current to scan across a conductive sample and build a topographic image of the surface.

Quantum tunnelling is caused by the probabilistic behaviour of wave/particles. There is always a finite probability that a particle (in this case an electron) can overcome a potential barrier (in this case the gap between probe and sample.) The probability of tunnelling is

determined by the distance between the probe and the sample in addition to the applied voltage, and the nature of the sample surface. Thus, the current measured during STM operation is a direct indication of the distance between the probe and the sample for a given voltage. The tunnelling current is measured as the tip rasters across the surface and this combined with the location of the probe produces a map of the tunnelling current (or the adjusted z-axis in constant current mode) and thus an image of sample surface.

Generally an STM can only obtain atomic resolution if the tip has a radius  $< 20\text{nm}$  (i.e. a high likelihood of a single atomic tip.) It is possible for a tip with a higher radius to obtain a single tunnelling current if it possesses a protruding asperity from the tip – but this is an uncommon and uncontrollable feature. STM relies on quantum tunnelling which allows electrons to move between electrodes at  $< 1\text{ nm}$  distances provided the voltage is high enough. A blunt tip will not obtain atomic resolution because for a given distance and voltage multiple regions at the tips surface will tunnel at the same time as sketched in Figure 2.24 A creating a blurred image.

The STM results shown in Figures 2.24 B & C are of cleaved HOPG. This creates a highly uniform surface from which atomic images can be obtained. Planes of graphite can be seen in Figure 2.24 B with a rough region in the top left corner that cannot be scanned at higher magnifications. Figure 2.24 C shows an atomic resolution of the smooth area with a hexagonal lattice of carbon atoms. This was obtained at room temperature and pressure in air at  $770\text{ mV}$ . The STM used a  $0.5\text{ mm}$  probe, because lower lengths typically introduce less vibrational noise into the image as the tip is relatively stiffer. These images are comparable to STM results achieved by probes of other techniques under similar conditions.

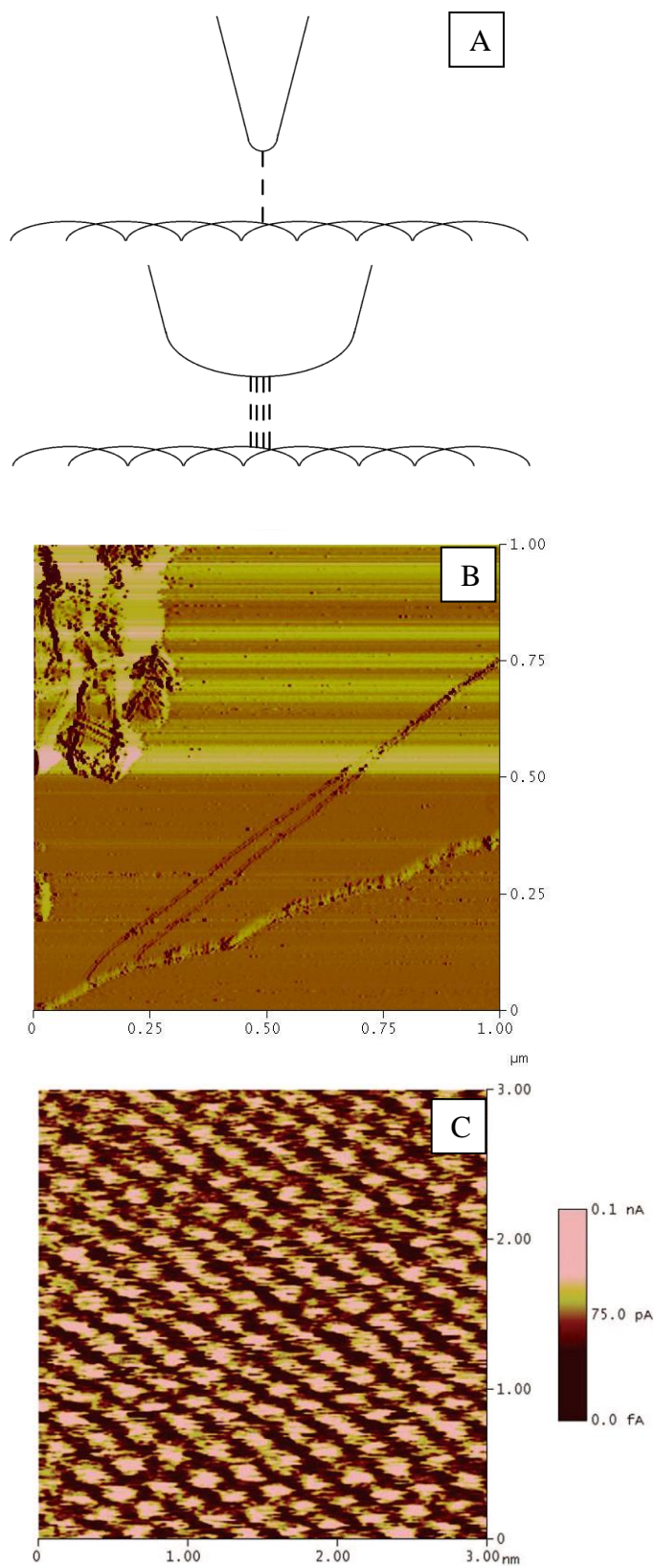


Figure 2.24. A) Illustration of tunnelling between sharp and blunt tips. B) 1 μm view of smooth regions of HOPG C) hexagonal atomic lattice observed with tungstate sharpened probe.

## 2.11 Conclusion

It was established that the conventional methods of manufacturing ultra-sharp tungsten probes is antiquated, unreliable and restrictive.<sup>34</sup> Despite this, tungsten probes have remained a vital instrument for many nanoscale applications. In this chapter an alternative method was proposed that may supersede the long-established 'drop-off method'.

Tungstate sharpening has been shown to produce ultra-sharp tips down to 20 nm radius, which is essential for nanoscopic interaction. Furthermore, this process was fully automated which removes the uncertainty of user error, in addition to saving time for any applications where these probes need to be produced in addition to making this a viable process for industrial fabrication. In-situ bulk coulometry analysis of the etching process was used to, provide an accurate indication of the progress of the electrochemical etching. This in-turn, allowed for controllable lengths between 0.5 - 4.5 mm. This adds versatility to the applications available to the probes in addition to surpassing the capabilities of the basic drop-off method. The probes were experimentally shown to be viable tools for STM: Atomic resolution was achieved on HOPG at room temperature and pressure, which is the most common application for these probes. These experiments have also explored the phenomenon of shadowgraphs and tungsten trioxide formation and briefly showing a variation of the drop-off method via angled electrosharpening.

Although the experiments in this chapter have achieved their aim of finding a viable alternative to the drop-off method, there remain many unexplored areas of interest which may lead to further improvements. In particular, tungsten is not the only material that is viable for electrosharpening, (any material that can be etched to form an electrochemically inactive insulating layer will likely be usable). Many materials have been tested successfully with the

drop-off method for many different applications, which suggests they may also be viable for tungstate sharpening.<sup>35,36,37,38</sup>

In addition, because tungsten probes are inherently disposable items it would be highly desirable to increase the rate at which tungsten probes can be etched. In typical SPM work it is a common occurrence to break probes during use – and any application where the probes come into contact with another sample will likely damage their nanoscale features. Thus increasing the rate of probe production will allow them to meet the demands of their consumable nature.

Because Tungstate Sharpening is a new electrosharpening technique, which uses different parameters, with different requirements and implementations there is a very wide scope for future work. The next chapter will show how some of the challenges outlined here can be addressed, leading to many practical improvements, and then, - how even these improvements can be surpassed.<sup>39</sup>

## 2.12 References

- [1] E. W. Müller, ‘Das feldionenmikroskop’, *Z. Für Phys.*, vol. 131, no. 1, pp. 136–142, 1951.
- [2] H. W. Lee, S. H. Kim, Y. K. Kwak, E. S. Lee, and C. S. Han, ‘The effect of the shape of a tip’s apex on the fabrication of an AFM tip with an attached single carbon nanotube’, *Sens. Actuators Phys.*, vol. 125, no. 1, pp. 41–49, Oct. 2005.
- [3] G. W. Conrad, J. A. Bee, S. M. Roche, and M.-A. Teillet, ‘Fabrication of microscalpels by electrolysis of tungsten wire in a meniscus’, *J. Neurosci. Methods*, vol. 50, no. 1, pp. 123–127, 1993.
- [4] P. McDonnell, T. Graveson, C. Rackson, and W. J. Kim, ‘A detailed study of scaling behavior in electrochemical etching of tungsten wires: Effects of non-uniform etching’, *J. Phys. Chem. Solids*, vol. 74, no. 1, pp. 30–34, Jan. 2013.
- [5] D. Xu, K. M. Liechti, and K. Ravi-Chandar, ‘Mesoscale scanning probe tips with subnanometer rms roughness’, *Rev. Sci. Instrum.*, vol. 78, no. 7, p. 073707, 2007.
- [6] T. Hagedorn, M. E. Ouali, W. Paul, D. Oliver, Y. Miyahara, and P. Grütter, “Refined tip preparation by electrochemical etching and ultrahigh vacuum treatment to obtain atomically sharp tips for scanning tunneling microscope and atomic force microscope,” *Rev. Sci. Instrum.*, vol. 82, no. 11, p. 113903, 2011.
- [7] A. K. Kar, S. Gangopadhyay, and B. K. Mathur, “A reverse electrochemical floating-layer technique of SPM tip preparation,” *Meas. Sci. Technol.*, vol. 11, no. 10, p. 1426, 2000.



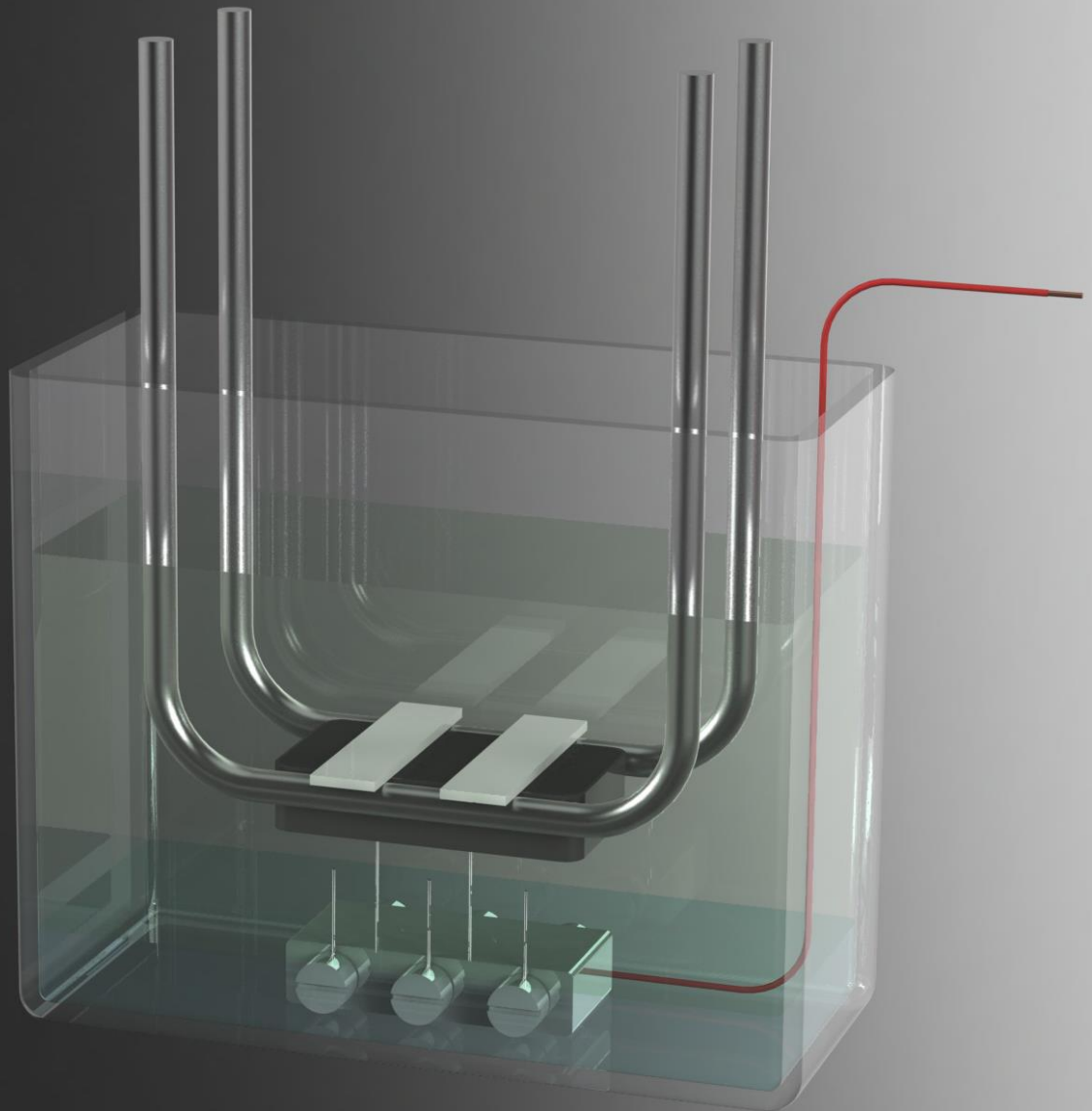
- [8] Y. Khan, H. Al-Falih, Y. Zhang, T. K. Ng, and B. S. Ooi, "Two-step controllable electrochemical etching of tungsten scanning probe microscopy tips," *Rev. Sci. Instrum.*, vol. 83, no. 6, p. 063708, 2012.
- [9] W.-T. Chang, I.-S. Hwang, M.-T. Chang, C.-Y. Lin, W.-H. Hsu, and J.-L. Hou, "Method of electrochemical etching of tungsten tips with controllable profiles," *Rev. Sci. Instrum.*, vol. 83, no. 8, p. 083704, 2012.
- [10] Z.-W. Fan and L.-W. Hourng, "The analysis and investigation on the microelectrode fabrication by electrochemical machining," *Int. J. Mach. Tools Manuf.*, vol. 49, no. 7–8, pp. 659–666, Jun. 2009.
- [11] B.-F. Ju, Y.-L. Chen, M. Fu, Y. Chen, and Y. Yang, "Systematic study of electropolishing technique for improving the quality and production reproducibility of tungsten STM probe," *Sensors Actuators Phys.*, vol. 155, no. 1, pp. 136–144, Oct. 2009.
- [12] Y.-C. Chiou, R.-T. Lee, T.-J. Chen, and J.-M. Chiou, "Fabrication of high aspect ratio micro-rod using a novel electrochemical micro-machining method," *Precis. Eng.*, vol. 36, no. 2, pp. 193–202, Apr. 2012.
- [13] H. Davy, 'The Bakerian Lecture: On Some Chemical Agencies of Electricity', *Philos. Trans. R. Soc. Lond.*, vol. 97, no. 0, pp. 1–56, Jan. 1807.
- [14] B.-F. Ju, Y.-L. Chen, M. Fu, Y. Chen, and Y. Yang, 'Systematic study of electropolishing technique for improving the quality and production reproducibility of tungsten STM probe', *Sens. Actuators Phys.*, vol. 155, no. 1, pp. 136–144, Oct. 2009.
- [15] Erik Lassner and Wolf-Dieter Schubert, *Tungsten Properties, Chemistry, Technology of the Element, Alloys, and Chemical Compounds*. Springer US, 1999.

- [16] P. Zanello, *Inorganic electrochemistry: theory, practice and applications*. Royal Society of Chemistry, 2003.
- [17] *Electrochemical Methods: Fundamentals and Applications*, Allen J. Bard, Larry R. Faulkner. Wiley, 2000.
- [18] G. Stephen Kelsey, 'The Anodic Oxidation of Tungsten in Aqueous Base', *J. Electrochem. Soc.*, vol. 24, no. 6, pp. 814–819, 1977.
- [19] J. W. Johnson and C. L. Wu, 'The Anodic Dissolution of Tungsten', *J. Electrochem. Soc.*, vol. 118, no. 12, pp. 1909–1912, 1971.
- [21] Y. Khan, H. Al-Falih, Y. Zhang, T. K. Ng, and B. S. Ooi, 'Two-step controllable electrochemical etching of tungsten scanning probe microscopy tips', *Rev. Sci. Instrum.*, vol. 83, no. 6, p. 063708, 2012.
- [20] W.-T. Chang, I.-S. Hwang, M.-T. Chang, C.-Y. Lin, W.-H. Hsu, and J.-L. Hou, 'Method of electrochemical etching of tungsten tips with controllable profiles', *Rev. Sci. Instrum.*, vol. 83, no. 8, p. 083704, 2012.
- [21] P. Kim, J. H. Kim, M. S. Jeong, D.-K. Ko, J. Lee, and S. Jeong, 'Efficient electrochemical etching method to fabricate sharp metallic tips for scanning probe microscopes', *Rev. Sci. Instrum.*, vol. 77, no. 10, p. 103706, 2006.
- [22] Y. Chen, W. Xu, and J. Huang, 'A simple new technique for preparing STM tips', *J. Phys. [E]*, vol. 22, no. 7, p. 455, 1989.
- [23] M. Nave, B. Rubin, V. Maximov, S. Creager, and K. G. Kornev, 'Transport-limited electrochemical formation of long nanosharp probes from tungsten', *Nanotechnology*, vol. 24, no. 35, p. 355702, Sep. 2013.

- [24] G. J. Edwards and P. R. Pearce, ‘A comparison of AC and DC electrochemical etching techniques for the fabrication of tungsten whiskers’, *J. Phys. Appl. Phys.*, vol. 11, no. 5, p. 761, 1978.
- [25] R. Hobara, S. Yoshimoto, S. Hasegawa, and K. Sakamoto, ‘Dynamic electrochemical-etching technique for tungsten tips suitable for multi-tip scanning tunneling microscopes’, *E-J. Surf. Sci. Nanotechnol.*, vol. 5, no. 0, pp. 94–98, 2007.
- [26] T. Hagedorn, M. E. Ouali, W. Paul, D. Oliver, Y. Miyahara, and P. Grütter, ‘Refined tip preparation by electrochemical etching and ultrahigh vacuum treatment to obtain atomically sharp tips for scanning tunneling microscope and atomic force microscope’, *Rev. Sci. Instrum.*, vol. 82, no. 11, p. 113903, 2011.
- [27] A. Schulte, ‘STM tips for in-situ scanning tunneling microscopy in aqueous solutions prepared using electrophoretic deposition of paint’, in *Micromachining and Microfabrication*, 1998, pp. 353–357.
- [28] S. L. Toh, H. Tan, J. C. Lam, L. C. Hsia and Z. H. Mai, ‘Optimization of AC Electrochemical Etching for Fabricating Tungsten Nanotips with Controlled Tip Profile’, *J. Electrochem. Soc.*, vol. 157, no. 1, pp. E6–E11, 2010.
- [29] O. L. Guise, J. W. Ahner, M.-C. Jung, P. C. Goughnour, and J. T. Yates, ‘Reproducible Electrochemical Etching of Tungsten Probe Tips’, *Nano Lett.*, vol. 2, no. 3, pp. 191–193, Mar. 2002.
- [30] G.S. Settles, *Schlieren and Shadowgraph Techniques*. Springer-Verlag Berlin Heidelberg, 2001.
- [31] M. Setvín, J. Javorský, D. Turčínková, I. Matolínová, P. Sobotík, P. Kocán, and I. Ošťádal, ‘Ultrasharp tungsten tips—characterization and nondestructive cleaning’, *Ultramicroscopy*, vol. 113, pp. 152–157, Feb. 2012.

- [32] A. J. Melmed, ‘Recollections of Erwin Müller’s laboratory: the development of FIM (1951–1956)’, *Appl. Surf. Sci.*, vol. 94, pp. 17–25, 1996.
- [33] G. Binnig and H. Rohrer, ‘Scanning tunneling microscopy’, *IBM Journal of Research and Development*, vol. 30, no. 4, pp. 355–369, 1986.
- [34] M. Cavallini and F. Biscarini, ‘Electrochemically etched nickel tips for spin polarized scanning tunneling microscopy’, *Rev. Sci. Instrum.*, vol. 71, no. 12, pp. 4457–4460, 2000.
- [35] J. S. Lloyd, A. Williams, R. H. Rickman, A. McCowen, and P. R. Dunstan, ‘Reproducible electrochemical etching of silver probes with a radius of curvature of 20 nm for tip-enhanced Raman applications’, *Appl. Phys. Lett.*, vol. 99, no. 14, p. 143108, 2011.
- [36] M. C. Baykul, ‘Preparation of sharp gold tips for STM by using electrochemical etching method’, *Mater. Sci. Eng. B*, vol. 74, no. 1, pp. 229–233, 2000.
- [37] G. Xu, Z. Liu, K. Xu, Y. Zhang, H. Zhong, Y. Fan, and Z. Huang, ‘Constant current etching of gold tips suitable for tip-enhanced Raman spectroscopy’, *Rev. Sci. Instrum.*, vol. 83, no. 10, p. 103708, 2012.
- [38] C. Albonetti, I. Bergenti, M. Cavallini, V. Dediu, M. Massi, J.-F. Moulin, and F. Biscarini, ‘Electrochemical preparation of cobalt tips for scanning tunneling microscopy’, *Rev. Sci. Instrum.*, vol. 73, no. 12, p. 4254, 2002.
- [39] F. Reymond, D. Fermin, H. J. Lee, and H. H. Girault, ‘Electrochemistry at liquid/liquid interfaces: methodology and potential applications’, *Electrochimica Acta*, vol. 45, no. 15, pp. 2647–2662, 2000.

# Chapter 3



## Enhancements to Electrosharpening

## Chapter 3: Enhancements to Electrosharpening

### 3.1 Introduction

Tungsten probes are typically used as consumables. Generally, the probes become damaged or contaminated upon interacting with other objects at the nanoscale, for example in STM it is common for tips to crash-land onto the sample surface which often makes them unusable afterwards. In addition, tungsten gradually oxidises in air which distorts the overall tip shape, and will ultimately alter any electronic properties associated.<sup>1,2</sup>

As a consumable many tungsten probes must often be produced in volume to facilitate multiple experiments. However, conventional techniques do not allow for the simultaneous fabrication of multiple probes with nanoscale tips. It has been shown to be fundamentally impossible to produce several tips simultaneously when relying on the drop-off method<sup>3</sup> introduced in Chapter 2.3.1

### 3.2 Conventional Techniques Applied to Batch Electrosharpening

An experiment was conducted using the drop-off method to test its feasibility towards batch sharpening. 3 probes were immersed in 2M KOH, attached in parallel to a metal bar with copper tape. A 4.5V power supply was used and the process stopped when the final probe was etched. Visual inspection was carried out to determine how the characteristics of the probes compare with those individually fabricated using drop-off experiments.<sup>4,5</sup>

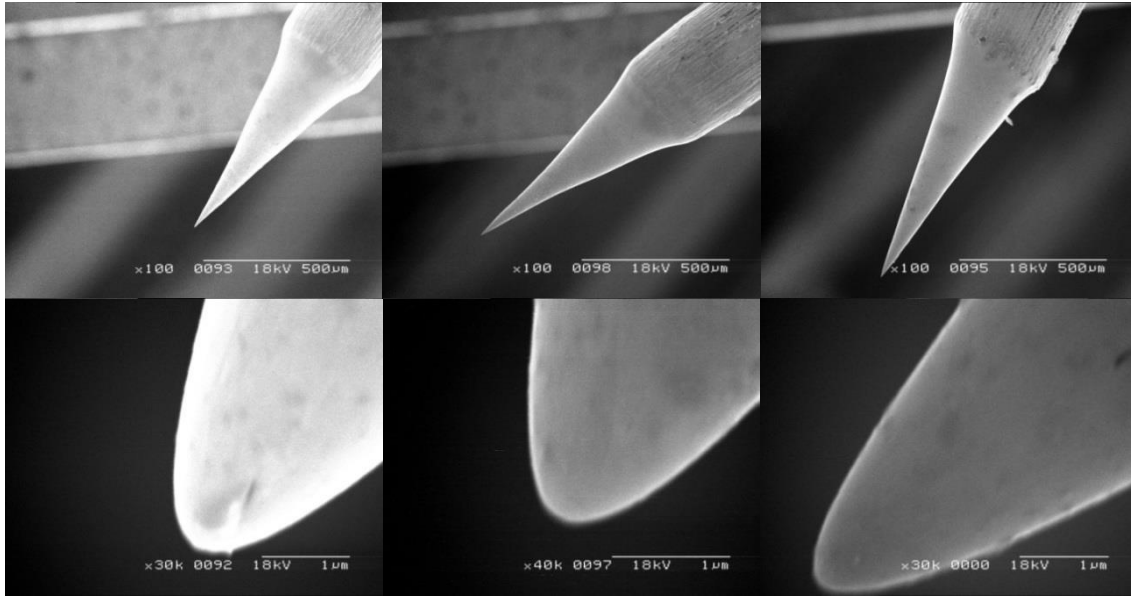


*Figure 3.1.* Three probes etched simultaneously via the drop-off method. Top row : probe profiles. Bottom row: probe tips

The SEM micrographs in Figure 3.1 show that the three probes were produced to similar geometries which indicates that repeatability of the drop-off method within this process may be possible.

However, Figure 3.1 (bottom row) indicates that the probe radii are of the order of 400 nm, far higher than that of single probe drop-offs produced under the same conditions, which is a significant disadvantage. This is due to the increased waiting time after the drop-off points which leads to a rounding of the tip. The method of control for the drop-off method is to detect a sudden decrease in current when the lower portion breaks away. However, although a small step may be noticed similar to those observed when performing tungstate sharpening continuously, as small sections from necking break off due to  $\text{WO}_3$  during tungstate sharpening. This is much more complex to automate from a microcontroller, and even more so via analogue components. As more probes are etched, the relative size of these steps decreases. Based on these findings, it would only be feasible to simultaneously etch multiple

probes to SPM specification using the drop-off method by scaling all the components for each probe – which defeats the advantages of batch processing. Thus, this experiment and fundamental limitations method suggest that unless blunt tips are required, the drop-off method is not a viable option for the mass production of tungsten probes.<sup>6,7,8</sup>

### 3.3 Tungstate Sharpening Applied to Batch Electrosharpening

*Tungstate Sharpening* does not suffer from the fundamental drawback of the drop-off method: an individual probe tip is not formed instantly; instead the sharpness is maintained over a significant period of time. This implies that *Tungstate Sharpening* may be used to form multiple probes simultaneously because it offers better potential to control process parameters – where slight variances in the probes formation do not matter even if they cause the probe to be etched at a slightly different rate.

A change in the apparatus design was necessary for tungstate sharpening batch probes to accommodate more probes. Although the use of an insulating tube for the probe to rest in is a simple solution for immersing a single probe within the electrolyte, doing so for multiple probes would require a different shape to a tube if they are to be etched in a non-linear manner. In addition, a different method for establishing contact to each probe would be required rather than a single wire, and there is an increased chance of the tube seal having to leak as the number of holes within which tungsten rod is position increases to enable simultaneous etching of multiple probes.



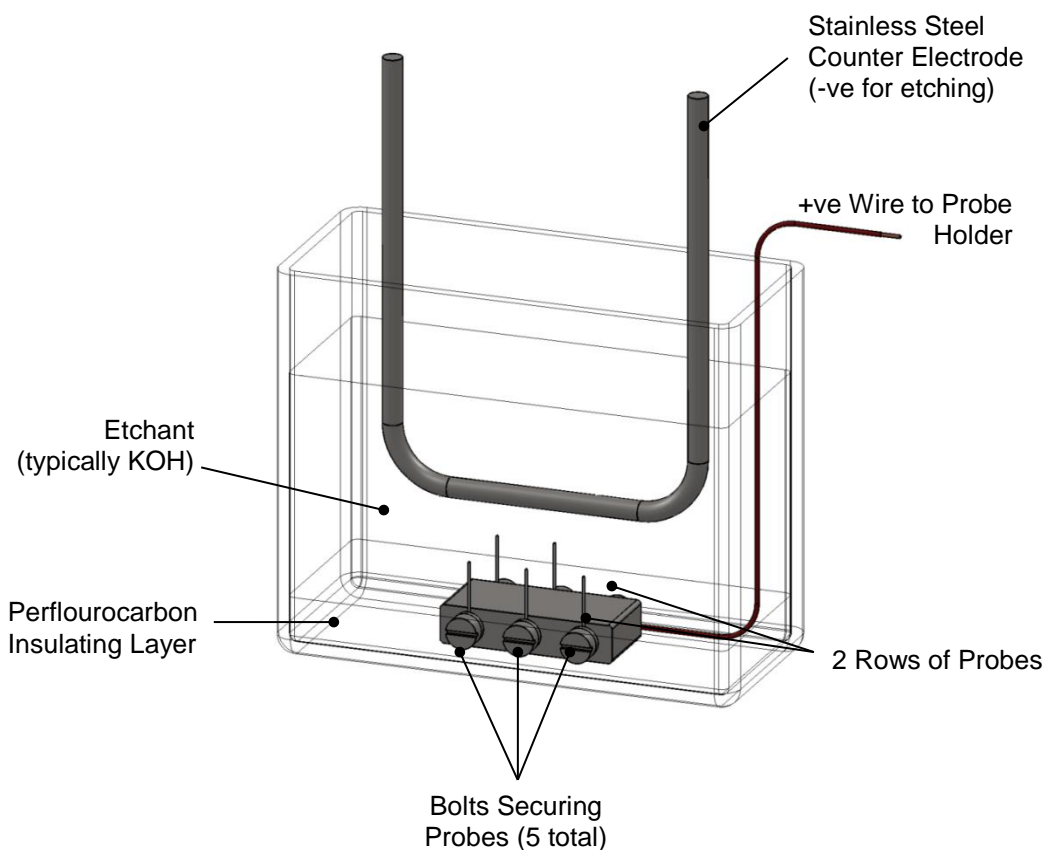


*Figure 3.2.* Basic batch electrosharpening set up.

A new set of equipment was created to solve these problems outlined in Figure 3.2. A perfluorinated carbon liquid (with carbon chains of random length) with a density over  $2 \text{ g/cm}^3$  was used as an electrochemical insulator. This was allowed to settle at the base of the electrolyte forming a 10 mm deep layer. The probes are then attached to a metal block between screwed bolts. A total of 5 probes may be attached to the block with  $15 \pm 5 \text{ mm}$  separation. A final bolt is used to connect an insulated wire from the block to the anode of the etching circuit. Instead of using a bubble barrier and L-plate counter electrode, a 5 mm U-shaped stainless steel tube is immersed above the probes to provide a significantly larger surface area than the probes, and prevent any hydrogen bubbles disrupting the process. (The

reason an electrode above the probes had not been used before for tungstate sharpening was simply for the convenience of removing the probe immediately after etching.)

Figure 3.3 displays the current as a function of etching time when 4.5 V is applied to the probes at the anode, in a 2M KOH solution.<sup>9</sup>

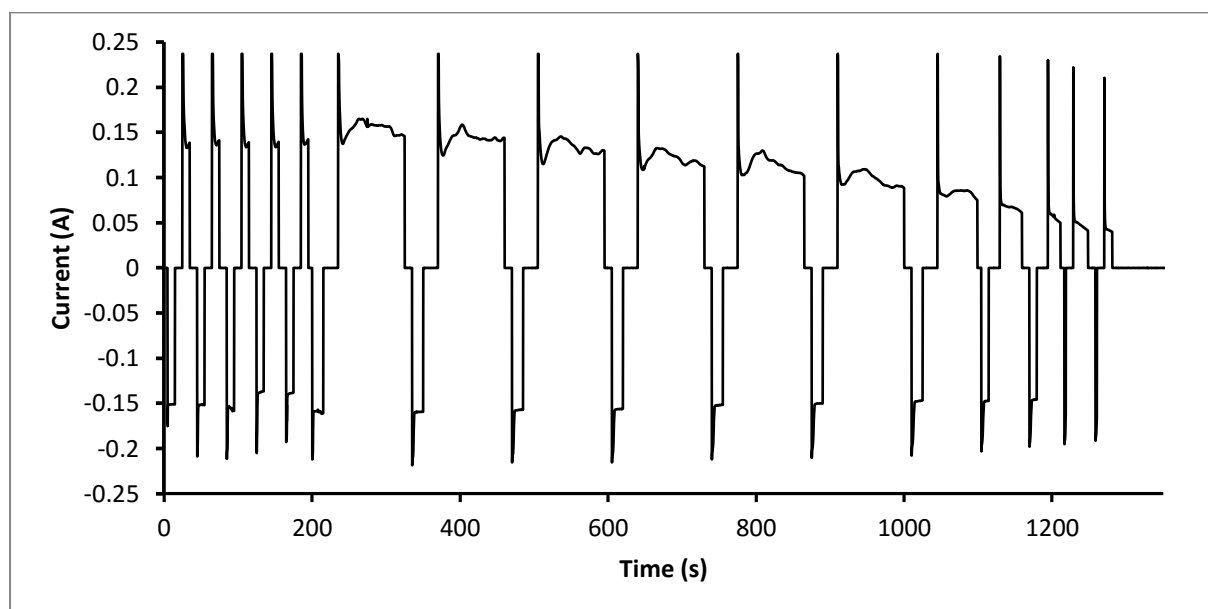


*Figure 3.3. Current analysis observed for batch electrosharpening.*

The LabView program developed for this process is mostly identical to that used for a single probe tungstate sharpening, with the exception that the current threshold values are multiplied by the number of probes used.<sup>10</sup>

The similar shape of the graph to that for a single probe tungstate sharpening enforces the assertion that the surface area may be inferred from current measurements. This process shows that with a linear change in surface area due to an increased number of probes the same multiple change in current threshold will produce almost identical timings for the duty cycle.<sup>11</sup> This also implies that either there are no current affecting parameters that change in a non-linear manner with the increased number of probes, or that several parameters may

change non-linearly but summate to an overall linear change. This implication is particularly useful when considering the length of the wire immersed, or possibly the shape of the metal to be etched.

Many probes were etched using the process described above, and used successfully for Arc Assembly, and general dielectrophoretic applications as outlined in Chapter 3. The probes were etched under identical conditions to the tungstate sharpening, albeit with the aforementioned apparatus changes made, and the multiplication of the current thresholds.

Only two of the probes maintained sharpness's under 100 nm, both of which are for lengths above 3 mm. However all probes have sharpness's beneath 1  $\mu\text{m}$ . Overall, this is an improvement over the drop-off method where for the best case scenario only one probe would have sub-100 nm sharpness.<sup>12</sup>

A dilemma with the process is that whilst there is a duration of time where multiple probes may be etched to a sharp tip, for different etching rates – the control over the length of individual probes is lost to an extent. This is because whereas the current measurements for tungstate sharpening gave an indication for the surface area of the probe, the batch probes current measurements are the summation of all the probes. Thus, one probe could be very long, while another very short – and there is no information to ascertain this over 2 medium length probes or anywhere in between their lengths.

A number of effects will cause the probes to etch at slightly different rates:

- Variation in wire starting length
- Variation in wire position
- Variation in curvature of wire (the tungsten is cut from a reel)

- Splitting of wires during cutting
- Debris attaching to probe
- Variations in electrical contact
- Distance from counter electrode
- Oxide thickness on wire
- Turbulence in the solution between probes (see below)<sup>2</sup>

The set-up for the experiments considers all of these parameters, but not all are practically prevented, and any one or a summation of these may create a difference in etching rate. Typically the difference in etching rate is very minor – and the process is still significantly dominated by the tungstate layer – but it is enough to create variations in probe length over 0.5 – 5 mm. Note: that because this is an accumulative effect the instantaneous current threshold values are still valid. Two solutions were proposed to counteract these effects: Probe separation to minimise the influence of turbulence, and a magnetic enhancement to introduce a new reinforcing effect which will counteract all the disruptive ones listed.

### 3.4 Modelling Fluid Flow Within Batch Electrosharpening

One of the significant effects which caused the probes to etch at different rates was identified as the turbulence within the solution. Whilst the other effects may be limited by experimental procedure, turbulence is caused by the fluid dynamics of the tungstate layer as it flows down the side of the probes. To solve this problem, a software based simplified model was constructed to simulate the conditions of the probes and assess any changes within the process that are likely to reduce the turbulence.

SolidWorks contains a flow simulator, designed for modelling fluid flow over objects to assess factors such as drag, stress, temperatures and turbulence. Over fluid regions SolidWorks solves the Navier-Stokes equations 3.1 – 3.3, which govern the mass, momentum and energy conservation laws:<sup>13</sup>

$$\frac{\partial \rho}{\partial t} + \frac{\partial(\rho u_i)}{\partial x_i} = 0 \quad 3.1$$

$$\frac{\partial(\rho u_i)}{\partial t} + \frac{\partial}{\partial x_j}(\rho u_i u_j) + \frac{\partial P}{\partial x_i} = \frac{\partial}{\partial x_j}(\tau_{ij} + \tau_{ij}^R) + S_i \quad 3.2$$

$$\frac{\partial \rho H}{\partial t} + \frac{\partial \rho u_i H}{\partial x_i} = \frac{\partial}{\partial x_j}(u_j(\tau_{ij} + \tau_{ij}^R) + q_i) + \frac{\partial \rho}{\partial t} - \tau_{ij}^R \frac{\partial u_i}{\partial x_j} + \rho \varepsilon + S_i u_i + Q_H \quad 3.3$$

$$H = h + \frac{u^2}{2} \quad (\text{substitution})$$

$u$	=	fluid velocity
$\rho$	=	fluid density
$\tau_{ik}$	=	viscous shear stress tensor
$q_i$	=	diffusive heat flux
$S_i$	=	mass distributed external force (buoyancy)
$Q_H$	=	heat source/sink per unit volume

Where 3.1 represents mass continuity equation, 3.2 represents the conservation of momentum equation, and 3.3 represents a modified conservation of energy equation. By solving all of these equations together it is possible to accurately model the fluid flow of systems with defined boundary conditions and starting conditions over finite element analysis.

The simulator calculates a solution from a finite element analysis of a mesh enveloping the object and user selected initial conditions and boundary conditions. The mesh may be seen in Figure 3.4.

The batch electrosharpening set-up for probes was modelled as with all dimensions identical to those observed in experiments, but where the insulating layer of perfluorocarbons is a solid block of 150x150x10 mm. The liquids used are a surrounding fluid of density 1250 kg/m<sup>3</sup> and a liquid which is formed on the surface of the probes of density 3100 kg/m<sup>3</sup>. These represent solutions of 7.5M NaOH and saturated Na<sub>2</sub>WO<sub>4</sub> (the by-product of hydrolysis with NaOH) respectively. The probes are modelled as an outlet with a radial flow of Na<sub>2</sub>WO<sub>4</sub> at 5 mm/s of fully developed flow perpendicular to all exposed surfaces of the cylinder. Within the same simulation two sets of probes are analysed in a layout similar to that used for the batch sharpening. A set of three probes have 3 mm separation while another set of two probes are separated by 6 mm. The only parameter changed in this case is the insertion of a third probe. This is to assess the role of probe separation distance which has been observed to influence fluidic motion in experiments via shadowgraphs. Two parameters, fluid density and turbulence intensity<sup>14</sup> are simulated to determine the nature of this motion.

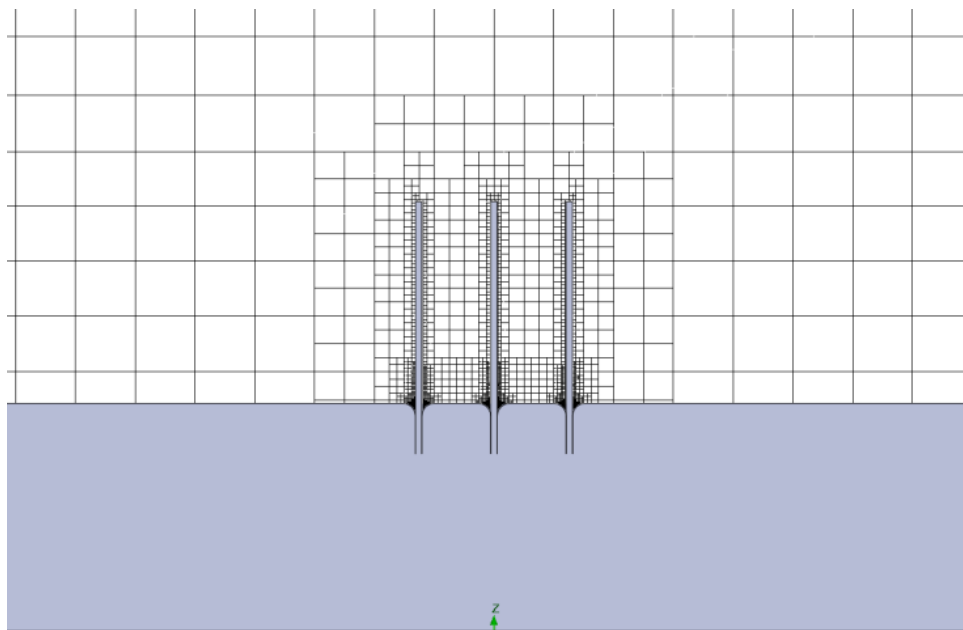


*Figure 3.4.* Mesh distribution for finite element analysis. The mesh shows the resolution of the calculations performed.

It should be noted that the interface between the etched probe and the insulation is different from tungstate sharpening to batch electrosharpening. In tungstate sharpening the probe is perpendicular to the insulation – the curvature of the tube is insignificant due to their relative sizes. However, in batch electrosharpening the aqueous solution forms a meniscus downwards as seen in Figure 3.5.

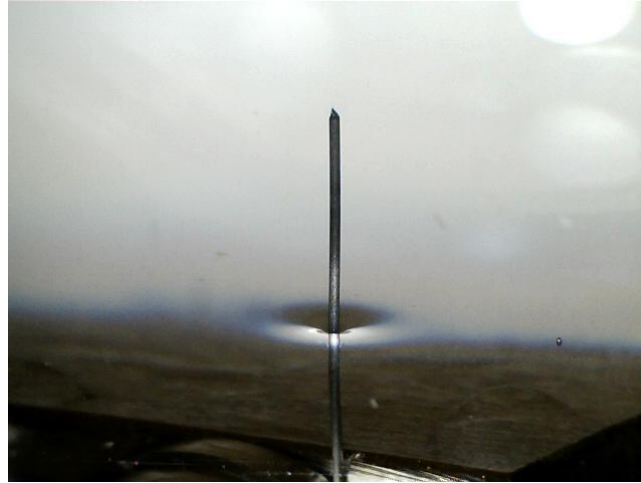


*Figure 3.5.* Reverse surface meniscus observed between KOH and Perfluorocarbons

This causes a region for tungstate to accumulate and extends the insulating region, which affects the shape of the probe towards the base. This is shown later in Figure 3.13 as a more conical shape than the as-modelled exponential contour of a typical tungstate sharpening. The meniscus is commonly modelled as two intersecting circles, where one denotes the surface tension of the fluid and the volume while the other accounts for the wettability of the solid-liquid interface. However, in this case, the meniscus is modelled by a single circle of 0.375 mm radius as measured by microscope imaging in Figure 3.6.

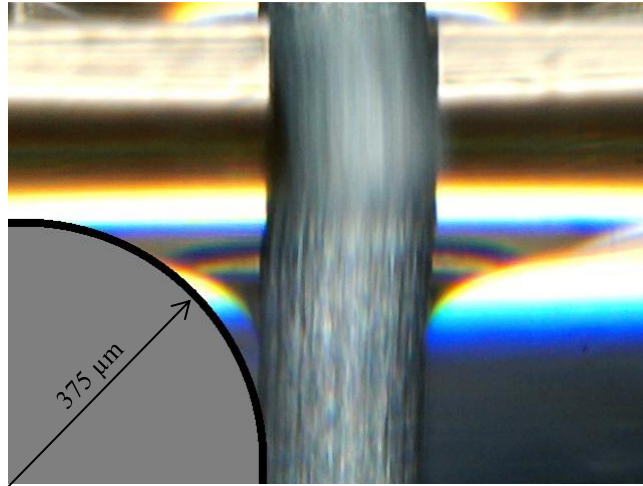


*Figure 3.6.* An approximation of the surface meniscus between the electrolytic/insulating boundary for batch sharpening.

Figure 3.7 shows the simulation results for turbulence intensity as light blue regions between the probes. The turbulence reaches intensities between 20-30% for both sets of probs. However, this turbulence is spread over a much larger area, i.e 6 mm separation and is much more uniform next to the probes. The effects of turbulence extend over the entire probe length, above the insulating layer. The same intensity of turbulence is only present for a fraction of the 2 mm separated probes and does not extend over the entire length of the probes. The results suggest that the same intensity of turbulence is expected between the probes irrespective of separation. However, this turbulence may not be evenly distributed.



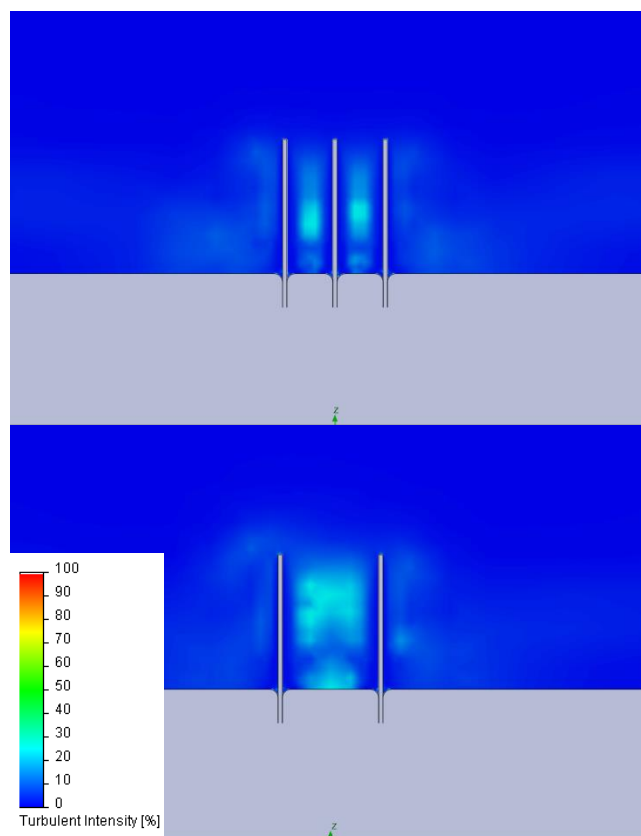


*Figure 3.7.* Turbulent intensity of the electrolyte between different probe separations during etching.

Figure 3.8 shows the simulation results for fluid density. The simulation shows a dense region accumulating down the probes, similar to that observed in experiments. For the two probes, this remains relatively symmetrical. However, for three probes the  $\text{Na}_2\text{WO}_4$  appears to rise again in the solution, rather than continuing to flow downwards. This would suggest that an additional fluidic flow is taking place which forces the dense region upwards.

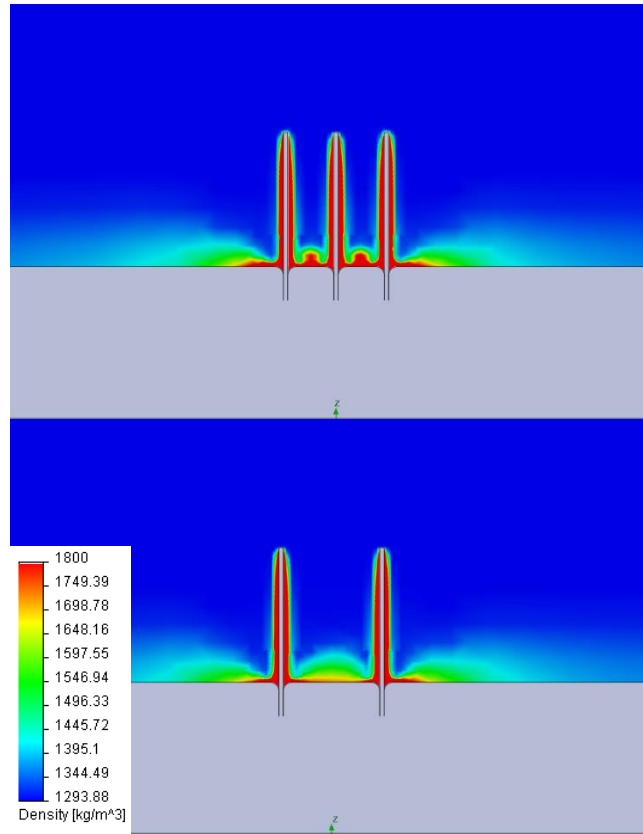


*Figure 3.8.* Modelled density of the Tungstate/electrolyte mixture in the probe etching system

In the context of electrosharpening, this accumulation of tungstate between confined probes, along with the implication of an increased fluidic flow taking place, could greatly affect the etching rate. This may occur either by the fluidic flow disrupting the tungstate layer - as may happen with unevenly distributed turbulence, or alternately it may decrease the etching rate for a probe. Both these scenarios have been observed with a central probe remaining far longer than surrounding probes - or forming a necking point and collapsing. For either explanation, the implication is that the probe sharpening is less likely to be disrupted by fluidic effects if the probes are separated further apart <sup>15</sup>.

### 3.5 Lorentz Force Theory

The Lorentz force is a phenomenon observed over charged particles whereby they experience 2 forces from electric and magnetic fields when in motion. It was first described as a product of these two fields by Michael Faraday.<sup>16</sup> An accurate model was developed through many iterations by different authors until the complete relationship was expressed by Hendrik Lorentz<sup>17</sup> in 1892:

$$F = q(E + v \times B) \quad 3.4$$

Where

$F$  is the force acting on the particle

$q$  is the charge of the particle

$E$  is the electric field

$v$  is the velocity of the particle

$B$  is the magnetic field.

The particle experiences a resultant force from the electric field acting on the charge of the particle, and from the magnetic field acting on the velocity of the particle in a direction perpendicular to the plane of the velocity and the magnetic field. For example, if an ion is considered in an electrolyte with an electromotive force its response under a magnetic field would be displayed as sketched in Figure 3.9.

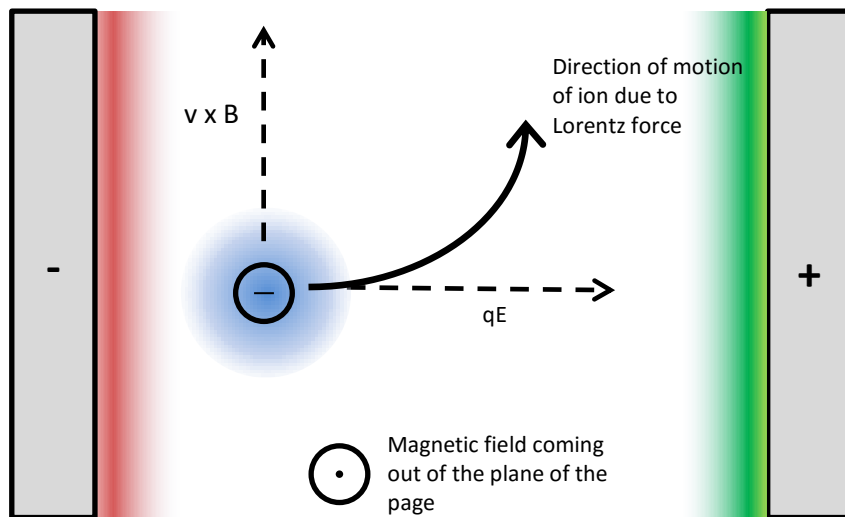


*Figure 3.9. Ion deflection due to the Lorentz force*

The resulting motion would be applied to all ions within the electrolyte. Since this affects mass transport, the entire fluid will experience a motion in the same direction. When the Lorentz force is applied to the bulk motion of ionic fluids it is considered a branch of “magnetohydrodynamics” – first established by Hannes Alfvén in 1942 (for which he was awarded a Nobel Prize in Physics)<sup>18</sup>. It currently has many applications in propulsion<sup>19</sup>, sensing<sup>20</sup>, microfluidics<sup>21</sup> and modelling cosmic events.<sup>22</sup> This thesis will elaborate on how this field is relevant to electrochemical sharpening, and in particular, the invention of etching sub-micron sharp probes and razor blades.

### **3.5.2 Application Within Electrosharpening**

The Lorentz force is experienced on any moving charged particle in both an electric field and magnetic field perpendicular to the directions of the fields. This has a significant bearing on the tungstate etching process. This means that for a tungsten probe where ions are electrochemically affected by the electric field and a magnetic field is applied down the probe

the ions will rotate around the probe instead of moving in a direct path to the electrode shown in Figure 3.10.

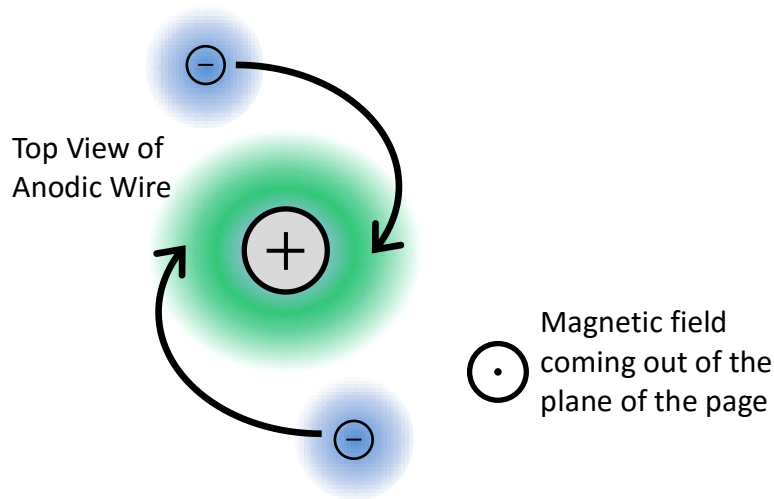


*Figure 3.10.* Sketch of Lorentz force acting on the radial movement of ions

This rotation causes a stirring motion in the fluid which will disrupt the tungstate layer. If the magnetic field diminishes in strength along the length of the probe, then the level of disruption will also decrease in strength. Thus towards the top of the probe the tungstate layer will be at a very low density by virtue of a higher magnetic field strength which stirs the accumulating tungstate into the surrounding solution. The etch rate in this top region of the probe will increase as a result. In turn, at the base of the probe where the magnetic field strength is gradually weaker, the tungstate layer follows a more linear flow which accumulates and is characterised by a low rate of etching.

The implication of this effect for batch electrosharpening is that it enforces a greater gradient of etching down the probe by virtue of the differential tungstate (decreasing), concentration along the probe length but within the KOH solution. This extra effect increases the gradient beyond the normal effect of the tungstate layer, and is expected to increase the gradient through similar disruption of the diffusion layer, in a manner similar to that observed when

the bulk solution is stirred in other electrochemical systems. The key parameters interacting under a Lorentz force applied to the tungstate sharpening process may be outlined as follows.

- The diffusion layer reaches a steady state based on the ion mobility limited by the  $\text{WO}_4^{2-}$  layer in any region on the probe.
- The  $\text{WO}_4^{2-}$  layer reaches steady state based on its production from the electrochemical reaction and removal by fluidic motion (induced by the Lorentz force) away from the probe as well as general dissolution.
- The effect of the Lorentz force induced stirring on the bulk solution will be determined by the sum of the motion of the ions which is governed by the tungstate layer and the diffusion layer.
- Equilibrium will be reached between these three parameters as the tungstate layer will increase as the diffusion layer is removed and the rate of the reaction increases. And as the rate of the reaction increases the Lorentz force on the bulk solution will increase exponentially increasing the tungstate layer until the tungstate layer is sufficient to reduce the differential increase of ion mobility to zero.

This shows the relationship between the divergent magnetic field on an individual probe and this creates a probe of different profile geometry and sharpness based on the nature of this field. However there is another implication for the invention: as the amount of etching is greatly increased if within a stronger the magnetic field it implies that a probe closer to the magnet will etch faster. This means if multiple probes are present in the field any probe which may have a different length/etching rate due to differences in immersion depth, angle and position will have a tendency to etch at the same rate to more similar lengths during the reaction.<sup>23,24</sup>

It is unclear if the general fixed parameters such as temperature, bulk electrolyte mobility, reaction route are similar or identical to non-magnetic systems. However the key parameters of the tungstate layer, diffusion layer and bulk stirring are assumed to be the dominating over these effects.

### 3.6 Magnetic Enhancements to Batch Electrosharpening

The Lorentz force is experienced on any charged particle in both an electric field and magnetic field perpendicular to the directions of the fields. This means that for a tungsten probe where ions are close to the electric field applied for etching and a magnetic field is applied down the probe the ions will rotate around the probe instead of moving in a direct path to the electrode. This rotation will cause a stirring motion in the fluid which will disrupt the tungstate layer. If the magnetic field diminishes in strength along the length of the probe, then the level of disruption will also decrease in strength. Thus towards the top of the probe the tungstate layer will be at a very low density as it is stirred into the surrounding solution allowing for an increased rate of etching in this region, but at the base of the probe the tungstate layer follows a more linear flow and accumulates forming a low rate of etching. This enforces a greater gradient of etching down the probe, with the intention of overcoming the differences in etching between multiple probes. This effect is sketched in Figure 3.11.

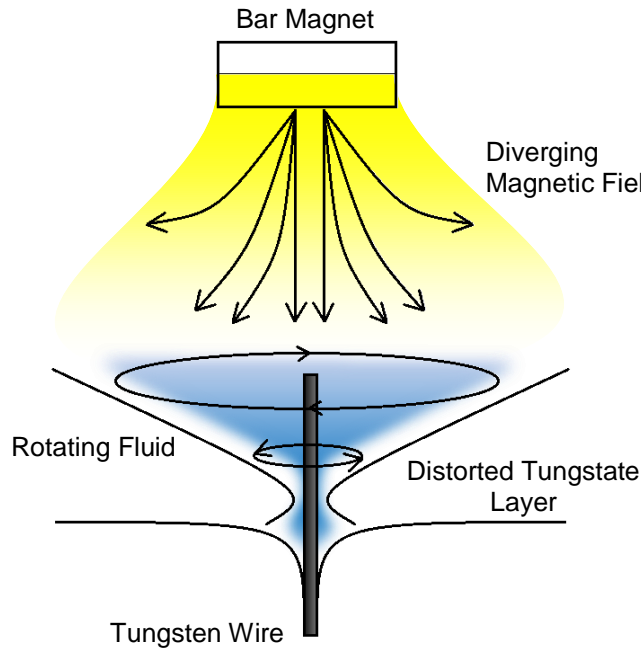


*Figure 3.11.* Sketch of overall Lorentz force for electrosharpening

The complete set up for magnetic batch electrosharpening can be seen in Figure 3.12. A second stainless steel counter electrode is placed to support a bar magnet which is insulated from the electrodes. The second electrode also serves the purpose of keeping an equal distance between the multiple anodes and cathode, This set up allows the magnet to be adjusted from contact with the probes to suspended 30 mm away – but at the expense of the surface area of the cathode (however this has a negligible effect provided it is still far greater than the surface area of the anode). Otherwise the apparatus is identical to the one used for normal batch electrosharpening.

$$F = \frac{B^2 A}{2\mu_0} \quad 3.5$$

Rearranged to give:



$$B = \sqrt{\frac{2F\mu_0}{A}} \quad 3.6$$

For a 50x25x10 mm bar magnet (using the largest side) with a 1.2 kg pull strength this gives a magnetic field strength of 0.154 T. This field strength is easily reproducible for a wide range of sources, and provides a starting point for further experimentation. Future work may include the manipulation of electromagnets, which will introduce feedback to the process with hall sensors, and may also be changed in orientation throughout the process.

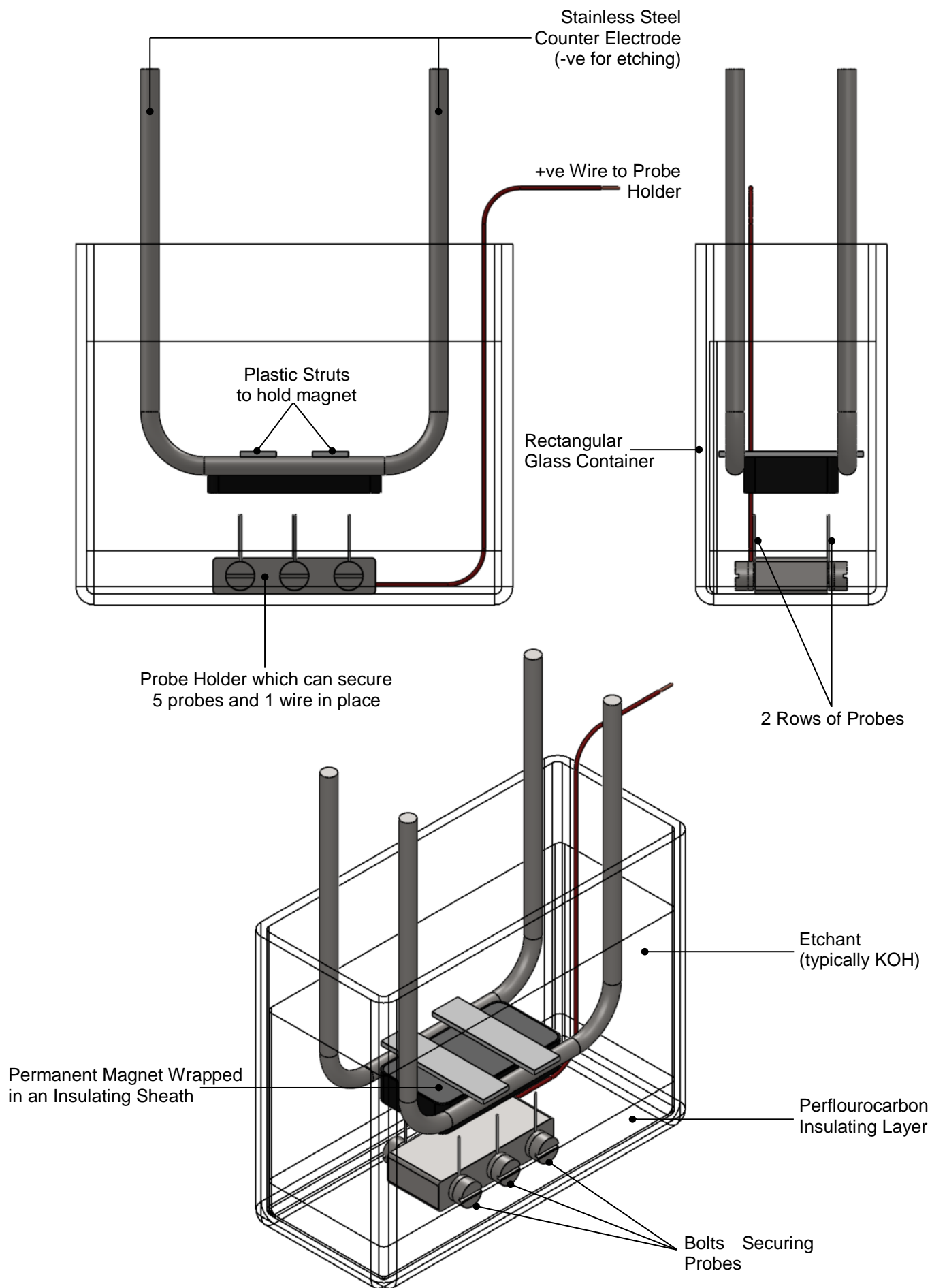


*Figure 3.12.* Elevated Views and Isometric Views of Magnetically Enhanced Batch etching

### 3.7 Evaluation of Batch Electrosharpening

Five probes were etched simultaneously using the magnetically enhanced batch electrosharpening technique. All the probes produced exhibited tip radii below 1  $\mu\text{m}$  however, only 2 obtained tip radii beneath 100 nm. The shape of the probes suggests that they were experiencing different gradients of etching. 3 probes emerged with relatively symmetrical conical shapes, which is a highly desired shape for tungsten probes due to its mechanical stability and vibration resistance. However, 1 probe possesses the typical exponential contour while another was characterised by an asymmetrical shape. These differences may be due to the position of the probes within the magnetic field.

Despite the differences in geometries and tip radii, the probes etched in batch and under the magnetic field were within  $2.2 \pm 0.7$  mm length which is a lower variation than without the magnetic field. The conical shapes also suggest that the magnetic field is causing the desired effect which is implied by the steeper gradient of etching and less accumulation of tungstate at the base of the probe. This is because the tungstate layer is stirred into the surrounding electrolyte rather than being allowed to flow down the probe and settle.

Although these results are currently not as optimal as etching an individual probe via tungstate sharpening, they show that the general concept of batch processing under a magnetic field is still a viable route to mass-producing sharper probes, unlike the drop-off method.

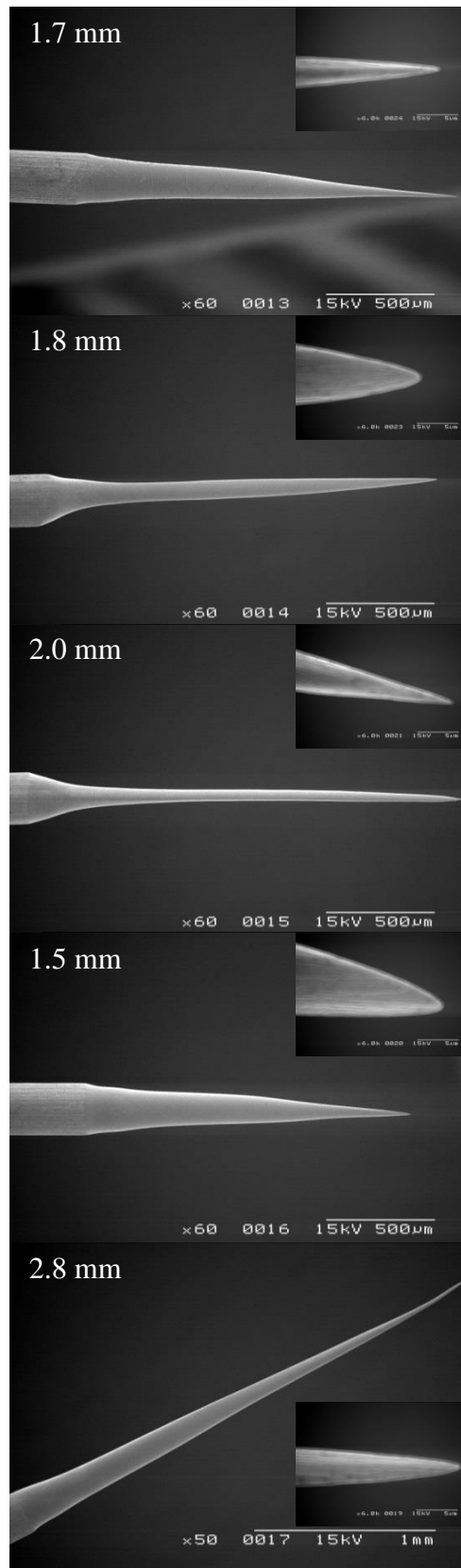
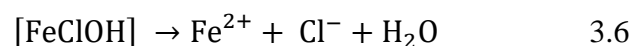
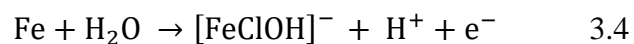


*Figure 3.13.* A set of 5 probes fabricated via magnetically enhanced batch etching.

### 3.8 Fabrication of Razor Blades

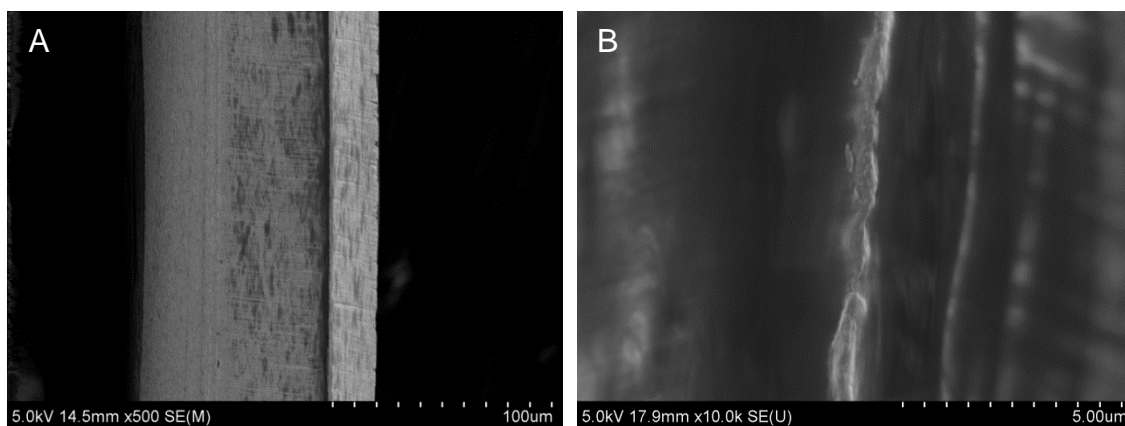
Typically electrosharpening techniques have only been applied towards making one dimensional (1D) probes. However, in 1993, G.W. Conrad et al<sup>25</sup> successfully modified the drop-off method to produce microscalpels for biological applications. However, this has received little reciprocation from the research community since, possibly due to inherent limitations to any variations on the drop-off method and the inability of the technique to achieve mass production. Given the success of Tungstate sharpening in overcoming the limitations of the drop-off method there is no obvious reason why the techniques cannot be applied to two dimensional (2D) objects, provided that a gradient of etching is maintained over the sharpened region due to the by-products (such as tungstate) formed during the electrochemical reaction.

Given tungsten is less frequently sold in the form of a sheet, and the fact that it is not a typical material for razor blade applications, 316-stainless steel was selected for etching. Due to the fact that 316 stainless steel is highly resistant to corrosion from chloride ions, and is used in many marine applications, so is the ‘worst-case’ steel to use in this application. Therefore, it is expected that if successful results are obtained with 316-stainless steel, it will pave the way for other steels or metals to consider as viable 2D materials for the bespoke etching process developed in this work. However, a caveat to this is that other steels may have a higher carbon content which is a relatively electrochemically inert material and could cause selective etching and de-alloying.<sup>26,27,28,29,30</sup> The principle reaction for the anodic dissolution of steel (assuming the transfer of 2 electrons) will be for iron<sup>31</sup>:



Although the majority of the material is iron, it is likely that the actual mechanism is far more complex, particularly with stainless steel containing 16-18% chromium and 10-14% nickel, and 7 other trace constituent elements.<sup>32</sup> In addition, unlike tungstate, the by-products of the electrochemical reaction do not readily dissolve into the surrounding electrolyte and can precipitate onto regions of the blade being etched. For this reason the experiments have been most successful with the application of magnetic electrosharpening, as the added motion in the fluid removes any precipitate via a continuous stirring effect.

#### Grinded Blades:



#### Magnetically Electrosharpened Blades:

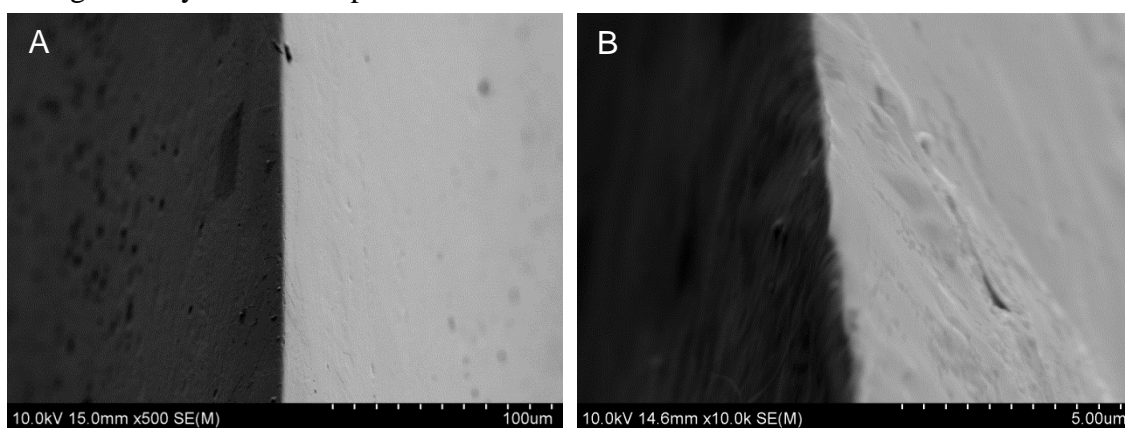


*Figure 3.14.* Comparison between conventional physically ground blades (top) to electrochemically etched blades via an equivalent to the Tungstate Sharpening method.

The electrosharpened blades have sharpness's down to 40 nm, almost an order of magnitude sharper than the 300 nm sharpness measured on commercially available blades. However, the sharpness of the electrosharpened blades diminishes towards the edges of the 2D metal plate, attributable to rounding which occurs due to the Lorentz force creating eddies around the corners of the blade. These eddies increase the rate of reaction as mass transport is increased.

It is not yet known if more complex 2D shapes can be sharpened, or how the rounding observed may be eliminated. However, the concept holds promise for unconventional sharpening and it is expected to be viable, provided that a gradient of etching is maintained

over the entire region to be sharpened and any precipitate is immediately removed via a stirring or equivalent method. At the very least, these results indicate opportunities and potential to expand further the field of electrochemical-sharpening research.

### 3.9 Conclusion

In the previous chapter *tungstate sharpening* was demonstrated as an essential alternative to the out-dated drop-off method. However, the concept was initially shown to only fabricate probes individually – a problem also faced by the drop-off method. Given that these probes are used as consumables, it would be very advantageous to develop a method that could facilitate faster production of probes with the desired characteristics. This chapter shows how this was accomplished. Furthermore, the tungstate sharpening process was shown to be versatile and may be coupled with Lorentz force to provide a better process control. The magnetohydrodynamic effect was exploited to demonstrate that probe with consistent lengths can be produced. Likewise the technique was successfully applied to the fabrication of razor blades from a plate of stainless steel, which demonstrates the versatility and potential to extend the technique to further applications.

This chapter introduced how impractical batch sharpening was with the drop-off method, due to the conflicting requirements to stop the process quickly, and yet continue the process for other probes at the expense of blunting other tips in the same batch. A new method for etching multiple probes simultaneously was introduced, based on Tungstate Sharpening, and facilitated by a unique liquid-liquid (perfluorocarbon - KOH) interface. This completely avoided the conflicting requirements of the drop-off method by allowing probes to obtain



sharp tips, and retain them whilst other probes are sharpened. This chapter also explored flow simulations to provide insights into the movement of  $\text{Na}_2\text{WO}_4$ , including the density and turbulence of the fluid. These showed that the small movement in the  $\text{WO}_3$  layer had a significant effect on the density – which is crucial due to the diffusion limited nature of this process. In addition to this, the simulations indicated that increasing the number of probes being etched (compared between two and three probes) would also increase the turbulence of the system if the increase in probes came at the expense of space between them (i.e. there is a minimum density of probes/area for batch probe etching).

Once established, the batch sharpening process was shown make use of enhancements from a divergent magnetic field which alters the profile of the probes in addition to improving consistency with their lengths. Furthermore, the magnetic batch electrosharpening could also be adapted to be used on 316 stainless steel sheets - a far more complex alloy, with varied electrochemical reactions. This implies that the process can be adapted to etch more complex 2D shapes and may lend itself to applications beyond just electrosharpening.

### 3.10 References

- [1] F. Reymond, D. Fermin, H. J. Lee, and H. H. Girault, ‘Electrochemistry at liquid/liquid interfaces: methodology and potential applications’, *Electrochimica Acta*, vol. 45, no. 15, pp. 2647–2662, 2000.
- [2] P. Zanello, *Inorganic electrochemistry: theory, practice and applications*. Royal Society of Chemistry, 2003, 10.1039/9781847551146.
- [3] W.-T. Chang, I.-S. Hwang, M.-T. Chang, C.-Y. Lin, W.-H. Hsu, and J.-L. Hou, “Method of electrochemical etching of tungsten tips with controllable profiles,” *Rev. Sci. Instrum.*, vol. 83, no. 8, p. 083704, 2012.
- [4] B.-F. Ju, Y.-L. Chen, M. Fu, Y. Chen, and Y. Yang, “Systematic study of electropolishing technique for improving the quality and production reproducibility of tungsten STM probe,” *Sensors Actuators Phys.*, vol. 155, no. 1, pp. 136–144, Oct. 2009.
- [5] D. Xu, K. M. Liechti, and K. Ravi-Chandar, ‘Mesoscale scanning probe tips with subnanometer rms roughness’, *Rev. Sci. Instrum.*, vol. 78, no. 7, p. 073707, 2007.
- [6] Y.-C. Chiou, R.-T. Lee, T.-J. Chen, and J.-M. Chiou, “Fabrication of high aspect ratio micro-rod using a novel electrochemical micro-machining method,” *Precis. Eng.*, vol. 36, no. 2, pp. 193–202, Apr. 2012.
- [7] Z.-W. Fan and L.-W. Hourng, “The analysis and investigation on the microelectrode fabrication by electrochemical machining,” *Int. J. Mach. Tools Manuf.*, vol. 49, no. 7–8, pp. 659–666, Jun. 2009.

- [8] B.-F. Ju, Y.-L. Chen, and Y. Ge, ‘The art of electrochemical etching for preparing tungsten probes with controllable tip profile and characteristic parameters’, *Rev. Sci. Instrum.*, vol. 82, no. 1, p. 013707, 2011.
- [9] R. Stone, M. Rosamond, K. Coleman, M. Petty, O. Kolosov, L. Bowen, V. Dubrovskii, and D. Zeze, ‘Tungstate sharpening: A versatile method for extending the profile of ultra sharp tungsten probes’, *Review of Scientific Instruments*, vol. 84, no. 3, pp. 035107–035107, 2013.
- [10] B. Zhang and E. Wang, ‘Fabrication of STM tips with controlled geometry by electrochemical etching and ECSTM tips coated with paraffin’, *Electrochimica acta*, vol. 39, no. 1, pp. 103–106, 1994.
- [11] H. Davy, ‘The Bakerian Lecture: On Some Chemical Agencies of Electricity’, *Philos. Trans. R. Soc. Lond.*, vol. 97, no. 0, pp. 1–56, Jan. 1807.
- [12] E. W. Müller, ‘Das feldionenmikroskop’, *Z. Für Phys.*, vol. 131, no. 1, pp. 136–142, 1951.
- [13] Dassault Systèmes SOLIDWORKS Corp, “Flow Simulation 2012 Technical Reference”, 2012.
- [14] Francois Gurniki, ‘Turbulent convective mass transfer in electrochemical systems’, Technical Reports from Royal Institute of Technology Department of Mechanics, 2000.
- [15] M. Kulakov, I. Luzinov, and K. G. Kornev, ‘Capillary and Surface Effects in the Formation of Nanosharp Tungsten Tips by Electropolishing’, *Langmuir*, vol. 25, no. 8, pp. 4462–4468, Apr. 2009.

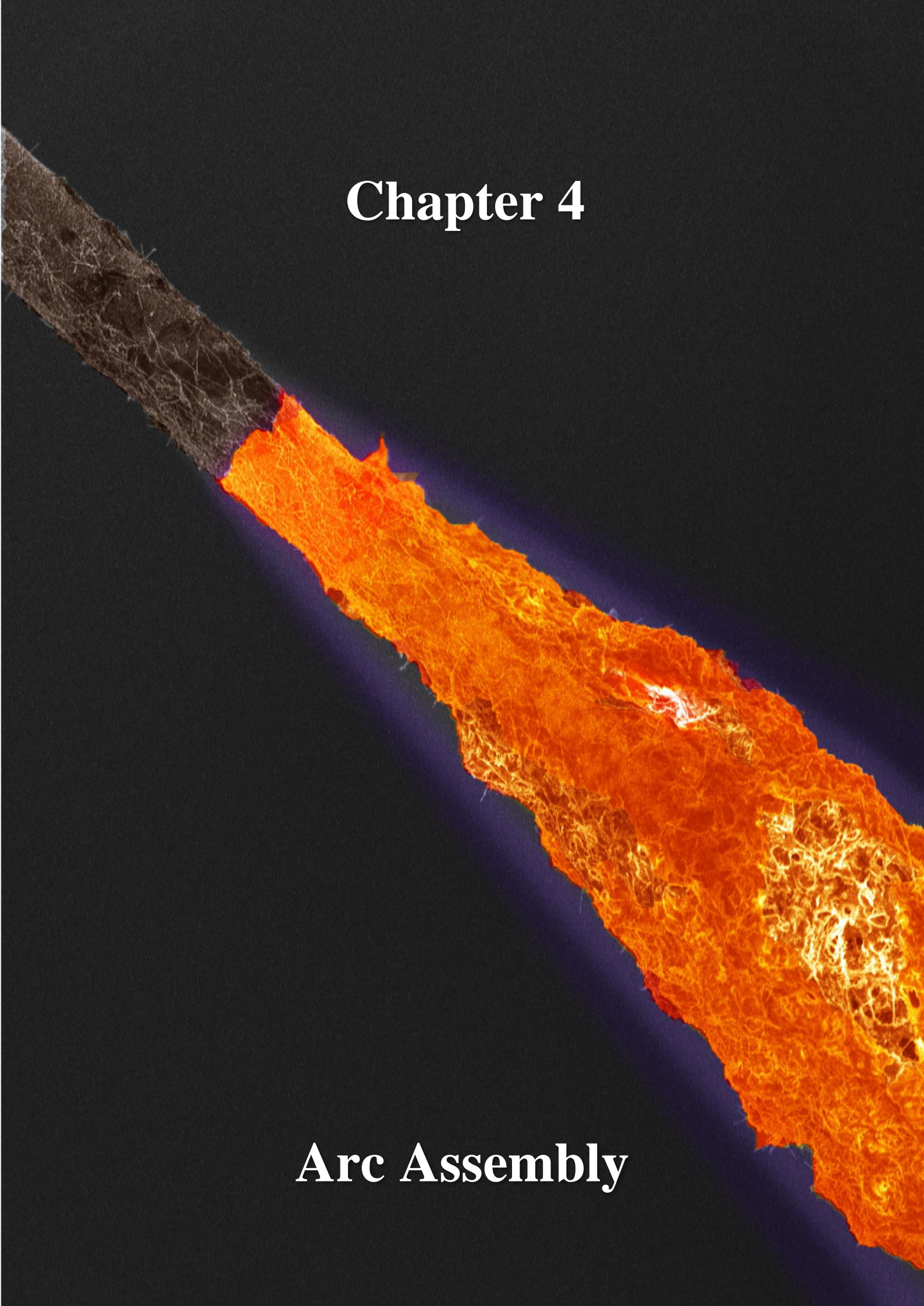
- [16] M. Faraday, 'Experimental Researches In Electricity', Philosophical Transactions of 1831-1838, vol. 1, p. 55, 1849.
- [17] H. A. Lorentz, *La théorie électromagnétique de Maxwell et son application aux corps mouvants*, vol. T. XXV. E.J. Brill, 1892.
- [18] H. Alfvén, 'Existence of Electromagnetic-Hydrodynamic Waves', *Nature*, vol. 150, no. 3805, pp. 405–406, 1942.
- [19] S. Takezawa, H. Tamama, K. Sugawawa, and H. Sakai, 'Operation of the thruster for superconducting electromagnetohydrodynamic propulsion ship "YAMATO1,"' *Bulletin of the MESJ*, vol. 23, no. 1, p. 46, 1995.
- [20] J. C. . Eijkel, C. Dalton, C. . Hayden, J. P. . Burt, and A. Manz, 'A circular ac magnetohydrodynamic micropump for chromatographic applications', *Sensors and Actuators B: Chemical*, vol. 92, no. 1–2, pp. 215–221, Jul. 2003.
- [21] S. Qian and H. H. Bau, 'Magneto-hydrodynamics based microfluidics', *Mech. Res. Commun.*, vol. 36, no. 1, pp. 10–21, Jan. 2009.
- [22] C.-G. Fälthammar, 'The discovery of magnetohydrodynamic waves', *Journal of Atmospheric and Solar-Terrestrial Physics*, vol. 69, no. 14, pp. 1604–1608, Oct. 2007.
- [23] G. Stephen Kelsey, 'The Anodic Oxidation of Tungsten in Aqueous Base', *J. Electrochem. Soc.*, vol. 24, no. 6, pp. 814–819, 1977.
- [24] J. W. Johnson and C. L. Wu, 'The Anodic Dissolution of Tungsten', *J. Electrochem. Soc.*, vol. 118, no. 12, pp. 1909–1912, 1971.

- [25] G. W. Conrad, J. A. Bee, S. M. Roche, and M.-A. Teillet, 'Fabrication of microscalpels by electrolysis of tungsten wire in a meniscus', *J. Neurosci. Methods*, vol. 50, no. 1, pp. 123–127, 1993.
- [26] L. Cagnon, V. Kirchner, M. Kock, R. Schuster, G. Ertl, W. T. Gmelin, and H. Kück, 'Electrochemical micromachining of stainless steel by ultrashort voltage pulses', *Zeitschrift für Physikalische Chemie/International journal of research in physical chemistry and chemical physics*, vol. 217, no. 4/2003, pp. 299–314, 2003.
- [27] T. Hryniewicz and K. Rokosz, 'Polarization characteristics of magnetoelectropolishing stainless steels', *Materials Chemistry and Physics*, vol. 122, no. 1, pp. 169–174, Jul. 2010.
- [28] M. Stöver, M. Renke-Gluszko, T. Schratzenstaller, J. Will, N. Klink, B. Behnisch, A. Kastrati, R. Wessely, J. Hausleiter, A. Schömig, and E. Wintermantel, 'Microstructuring of stainless steel implants by electrochemical etching', *Journal of Materials Science*, vol. 41, no. 17, pp. 5569–5575, Jun. 2006.
- [29] L. S. Andrade, S. C. Xavier, R. C. Rocha-Filho, N. Bocchi, and S. R. Biaggio, 'Electropolishing of AISI-304 stainless steel using an oxidizing solution originally used for electrochemical coloration', *Electrochimica Acta*, vol. 50, no. 13, pp. 2623–2627, Apr. 2005.
- [30] Y. D. Gokdel, S. Mutlu, and A. D. Yalcinkaya, 'Self-terminating electrochemical etching of stainless steel for the fabrication of micro-mirrors', *Journal of Micromechanics and Microengineering*, vol. 20, no. 9, p. 095009, Sep. 2010.
- [31] *Electrochemical Methods: Fundamentals and Applications*, Allen J. Bard, Larry R. Faulkner. Wiley, 2000.

- [32] P. A. Selembo, M. D. Merrill, and B. E. Logan, ‘The use of stainless steel and nickel alloys as low-cost cathodes in microbial electrolysis cells’, *Journal of Power Sources*, vol. 190, no. 2, pp. 271–278, May 2009.

# Chapter 4

## Arc Assembly



## Chapter 4: Arc Assembly

### 4.1 Carbon Nanotube Overview

#### 4.1.1 Interest in Carbon Nanotube Yarns

Carbon nanotubes (CNTs) have a variety of “record-breaking” material properties, in particular, their high mechanical strength, varied electronic conductivity and high thermal conductivity.<sup>1</sup> However, these properties are only exhibited over the size of the nanotubes – typically up to  $\sim 10\mu\text{m}$  in length.<sup>2</sup> There is a drive to exploit these properties on the macro-scale, where they could replace inferior materials in any tensile, and/or conducting industry.<sup>3</sup>

However, no pure nanotube yarn to date has exceeded 1.3 GPa in tensile strength yet, i.e. the measured tensile strength of individual CNTs is 63 GPa. This is because there is no effective method for extending the  $\text{sp}^2$  bonding within the CNTs between adjacent CNTs. Instead, yarns are constructed using the relatively weak Van der Waals forces between the particles.

Although many research groups claim to be taking advantage of CNTs unique properties to make yarns, unless thorough research is undertaken to overcome the lack of molecular bonding between individual CNTs, these fibres are simply elaborate conglomerates.<sup>4,5,6,7</sup>

‘Arc Assembly’ is a new process which builds materials from nanoparticles, in this particular case, CNTs. It utilizes the chemical changes formed by the plasma within arc discharges and the motion of nanoparticles induced by dielectrophoresis (DEP). The process demanded an



electrode capable of generating a strong electric field gradient whilst temporarily withstanding the conditions of an arc discharge. For these reasons, the aforementioned ultra-sharp tungsten probes were ideal tools to act as disposable electrodes to develop this process.

This chapter explores the background of carbon nanotubes, a general observed mechanism and a variety of material and nanoscopic analytical techniques to inform the experimental development of Arc Assembly.

#### **4.1.2 Carbon Nanotube Characteristics**

Carbon nanotubes are an  $sp^2$  allotrope of carbon whereby 2D sheets of graphene are rolled into cylinders. Most likely, they were first observed in 1952 by Rasdushkevich & Lukyanovich as “tubular carbon filaments”.<sup>8</sup> However, the breakthrough of CNTs into the scientific community came from Iijima’s 1991 work from high purity samples, high quality images and relevant analysis.<sup>9</sup>

As an  $sp^2$  allotrope, CNTs have a hexagonal lattice. As this lattice is folds around itself, it may be orientated in different chiral directions. This orientation is called the chirality of the CNTs and is referred to using (n,m) notation for the direction of the unit cell axis which are perpendicular to the length of the tube as seen in Figure 46. The CNT chirality is known as “zigzag” and “armchair” for  $m = 0$  and  $n = m$ , respectively. The chirality describes the shapes created from the hexagonal lines in those directions. All directions other than armchair and zigzag are known as “chiral”. The chirality can determine various electronic properties of a CNT as the band structure changes based on the direction of transport across the lattice. When  $(n-m = 3q)$  where  $q$  is an integer a tube is metallic (thus 1/3 of chiral and zigzag nanotubes are metallic) while all armchair CNTs are metallic.<sup>10,11,12,13</sup>

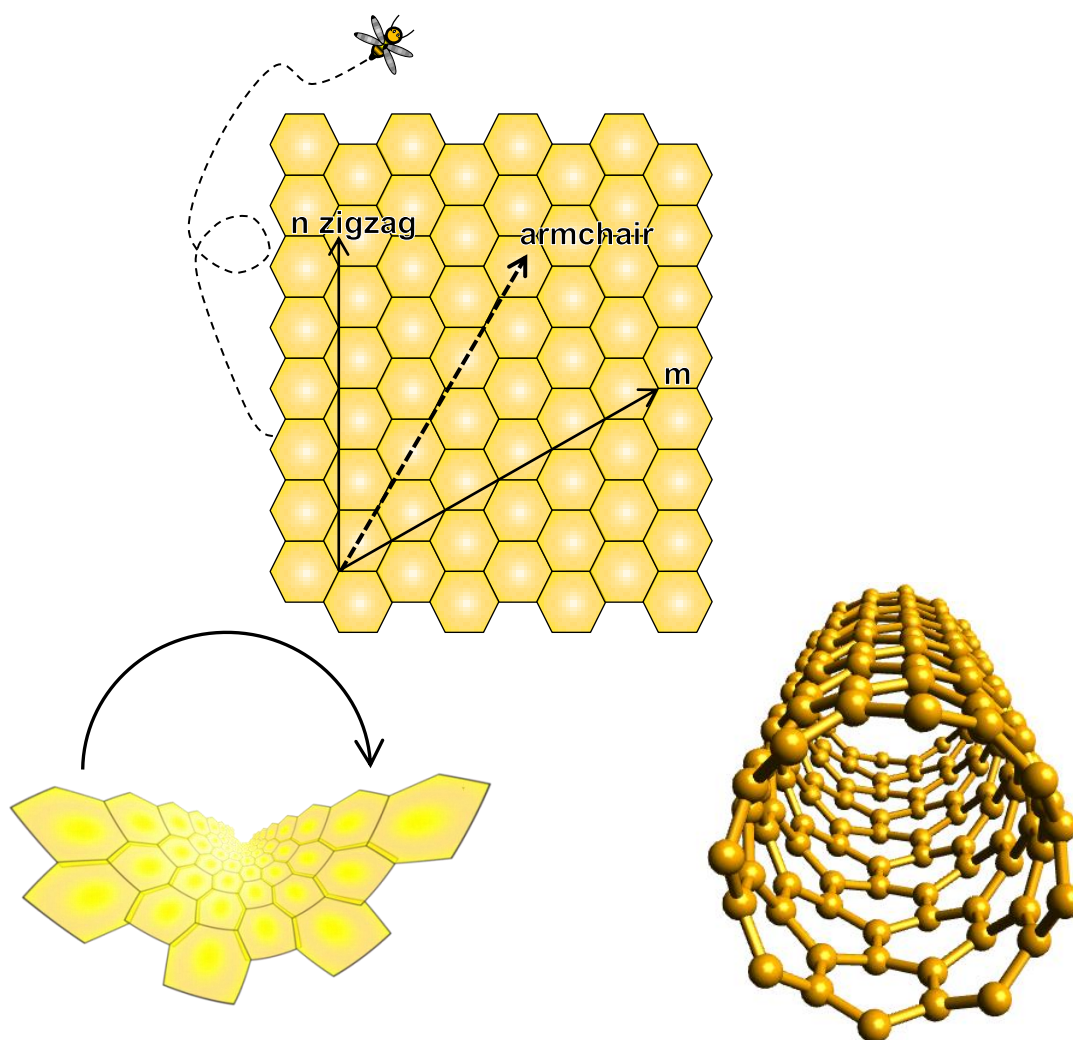


*Figure 4.1. Carbon  $sp^2$  hexagonal lattice*

Author's Note: nanoscopic bees are conjecture and have yet to be observed.

### 4.1.3 Synthesis of Carbon Nanotubes

There are a wide variety of methods for the synthesis of carbon nanotubes typically involving a pure carbon or hydrocarbon source, high temperatures and transition metal catalysts. The most common is chemical vapour deposition CVD – (and many variations on CVD growth)

but other growth techniques include laser ablation<sup>14</sup>, plasma torch<sup>15</sup>, flame synthesis<sup>16</sup>, solar synthesis.<sup>17</sup> It is also possible for carbon nanotubes to form in nature.<sup>18</sup>

Of a particular interest to this thesis is the Arc Evaporation method which was historically the method that led to the first observation and characterisation of CNTs by Iijima<sup>19</sup> and remains a competitive method of mass manufacturing both single walled nanotube (SWNT) and MWNT varieties. The apparatus consists of two carbon electrodes within a ~2.5 kPa – 67 kPa atmosphere and the initial growth was carried out under a He atmosphere to prevent any unwanted chemical reaction which could affect the quality of the CNTs grown. However the atmosphere does not necessarily have to be inert<sup>20</sup>. This was based on apparatus used for synthesising C<sub>60</sub> fullerenes, however a key difference in CNT production is that the separation distance between the electrodes is maintained, rather than being driven into contact when arcing. To synthesise the CNTs an arc discharge takes place at 20V over ranges or current between 50 – 100A. Carbon is vaporised from the anode and condenses on the cathode forming “soot” which contains ratios of SWNT and MWNT of different diameters, depending on conditions. Typically the yield for arc discharge synthesis is up to 30%<sup>21</sup>, albeit, claims have been made for 97% yields<sup>22</sup>. The first synthesis of carbon nanotubes by arc evaporation within a liquid nitrogen environment was conducted by Alex Zettl et al.<sup>23</sup>. This has since led to a niche area of research within arc evaporation where many other examples of liquid environments such as water<sup>24</sup> and NaCl solutions.<sup>25</sup> have been successful.

There is no complete model which explains the mechanism for carbon nanotube growth via Arc Evaporation and it is currently, practically impossible to observe or take measurements from arc discharges at nanoscales. Current models encompass many different mechanisms for growth via vapour, liquid and solid states, in addition to crystallisation effects and effects of

the electric field on the electrodes. However, no model has been completely verified and they are often complicated by differing results from various groups.<sup>26,27,28,29</sup>

However, although there is no explanation for arc evaporation growth, what is particularly relevant to this thesis and to the fabrication of nanotube threads is the fact that amorphous carbon is removed during the arc processes, MWNT caps remain open during arcing and bulk portions of carbon nanotubes survive the process once formed. If this is true, then it suggests that other processing method involving arc discharges may be employed to alter the material characteristics of MWNTs without significantly damaging them.

## 4.2 Introduction to Dielectrophoresis

One method for creating CNT yarns is dielectrophoresis. This phenomenon was first observed by Pohl et al. in 1951. It describes a resultant force experienced by a particle in a non-uniform electric field. Between 2 parallel electrodes the electric field is uniform, and an induced dipole charge on a particle will experience equal forces between each plate. However, any difference in the geometry of the electrodes will create a non-linear electric field causing the particle to experience a resultant force where the dipole is subjected to a stronger force towards (or away from) one electrode than the other. The dipoles orientation is determined by the frequency of the electric field and its surrounding medium. The strength of the force is then determined by the size of the particle and the electric field gradient. The phenomenon is described by the following equations: <sup>30,31,32,33</sup>

For spherical particles:

$$\bar{F}_{DEP} = 2\pi r^3 \epsilon_m \operatorname{Re} \left( \frac{\epsilon_o^* - \epsilon_m^*}{\epsilon_o^* + 2\epsilon_m^*} \right) \nabla |E|^2 \quad 4.1$$

For particles with a high aspect ratio, such as CNTs:

$$\bar{F}_{DEP} = \underbrace{\frac{\pi r^2 l}{6}}_{\text{Geometry of Particle}} \epsilon_m \underbrace{\operatorname{Re} \left( \frac{\epsilon_o^* - \epsilon_m^*}{\epsilon_m^*} \right)}_{\text{Modified Clausius-Mossotti Function}} \underbrace{\nabla |E|^2}_{\text{Gradient of Electric Field}} \quad 4.2$$

$\overline{F}_{DEP}$	<i>Dielectrophoretic Force</i>
$E$	<i>Electric Field</i>
$r$	<i>Object Radius</i>
$l$	<i>Object length</i>
$\epsilon_m$	<i>Permittivity of Medium</i>
$\epsilon_m^*$	<i>Complex permittivity of Medium</i>
$\epsilon_o^*$	<i>Complex permittivity of Object</i>

The equations show that  $\overline{F}_{DEP}$  is proportional to the volume of the particle and its shape in addition to  $\epsilon_m$ , the dielectric permittivity of the medium. Also,  $\overline{F}_{DEP}$  is orientated along the gradient of the electric field with its sign and magnitude dependent on the real part of the Clausius-Mossotti function (defined as  $\text{Re}(K)$ ). Thus the type of CNTs used, the fluid they are immersed in, and the electrode geometry will all play a role in determining the dielectrophoretic effect in experimentation.

## 4.2.2 The Clausius-Mossotti Function

This function indicates the polarisation of 2 adjacent different regions, a particle and its surrounding medium, in this case. Typically it is bound between 1 for  $\epsilon_o^* \gg \epsilon_m^*$  and - 0.5 for  $\epsilon_m^* \gg \epsilon_o^*$ . However, this is modified for cylindrical objects. The Clausius-Mossotti function shows that for high frequencies a conductive particle within a dielectric medium will experience a positive force towards the maxima in the electric field gradient. However a conductive particle at low frequencies will experience a negative force away from the maxima of the electric field. This is because a conductive particle (a poor dielectric) will polarise to the surrounding medium instead of the electric field. As the frequency increases the permittivity of the surrounding medium will decrease because dielectric relaxation causes

the polarisation to move out of phase with the electric field. In this case, the particle will exhibit a polarity opposite to the medium, and thus opposite to the electric field. The particle will experience an attractive force towards the region where the electric field is strongest as a result.<sup>34,35</sup>

### 4.3 Dielectrophoresis for Arc Assembly of Carbon Nanotubes

Arc assembly is the result of applying a dielectrophoretic signal at a significantly higher voltage which can overcome the dielectric breakdown strength, such that an arc occurs between the dipole chains as they connect together. This is outlined in Figure 4.2 which shows how a tungsten probe is used to assemble chains of carbon nanotubes acting as dipoles within the high frequency field.

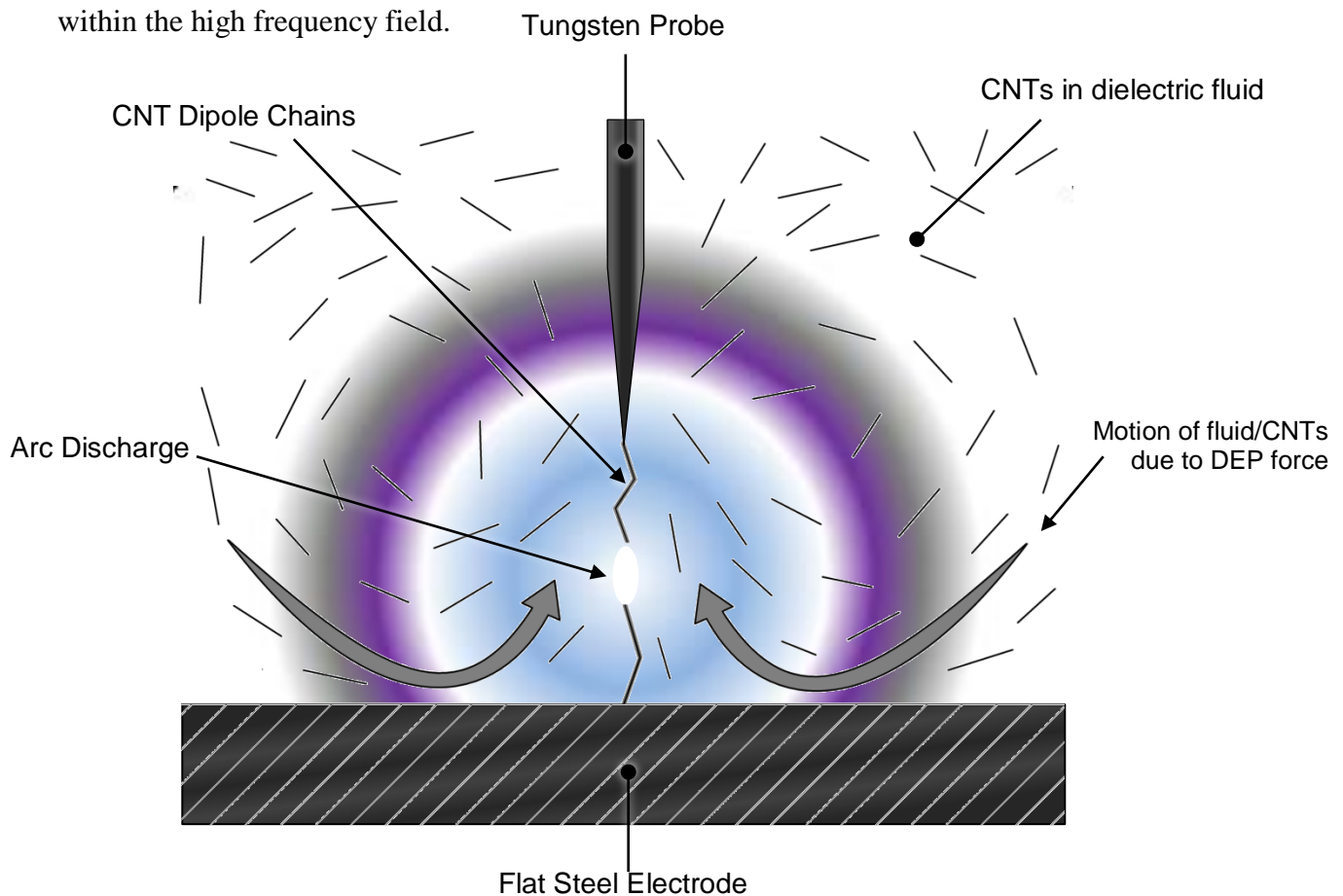
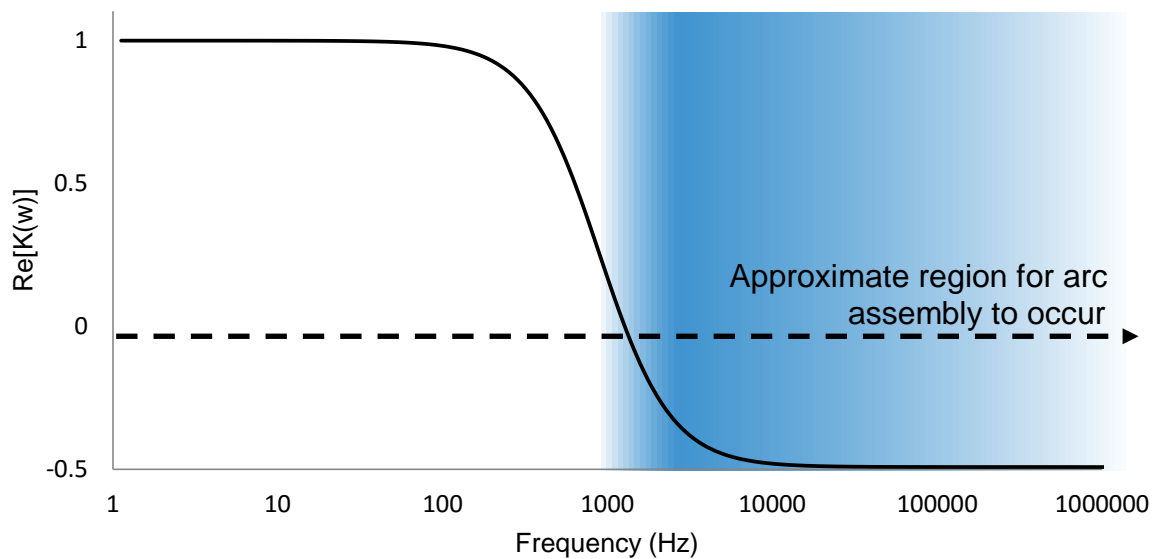


Figure 4.2. Diagram of Arc Assembly Process

The frequency requirement for dielectrophoretic attraction between MWNTs has experimentally been observed to be above ~50 kHz and the voltage required for arcing is ~300 V at 10  $\mu\text{m}$  in oleic acid. Generally voltages of 5 – 20 V are used for the dielectrophoretic alignment of CNTs at frequencies of 1 – 20 MHz. However, at high frequencies, high voltages cannot be continuously applied as the motion of the particles is too great to form any dipole chains. Additional dielectric medium have also been used such as Polydimethylsiloxane (PDMS) and Octamethylcyclotetrasiloxane (OMCTS) which require different voltages and frequencies for arc assembly to occur.<sup>36</sup>



*Figure 4.3.* Approximate plot of  $\text{Re}(K)$  from observations of DEP in various mediums

The graph shows a theoretical plot of the equation for the frequency dependence of  $\text{Re}(K)$  based on particles with ohmic loss (note the difference between this and  $\text{Re}(K)$  of previous equations



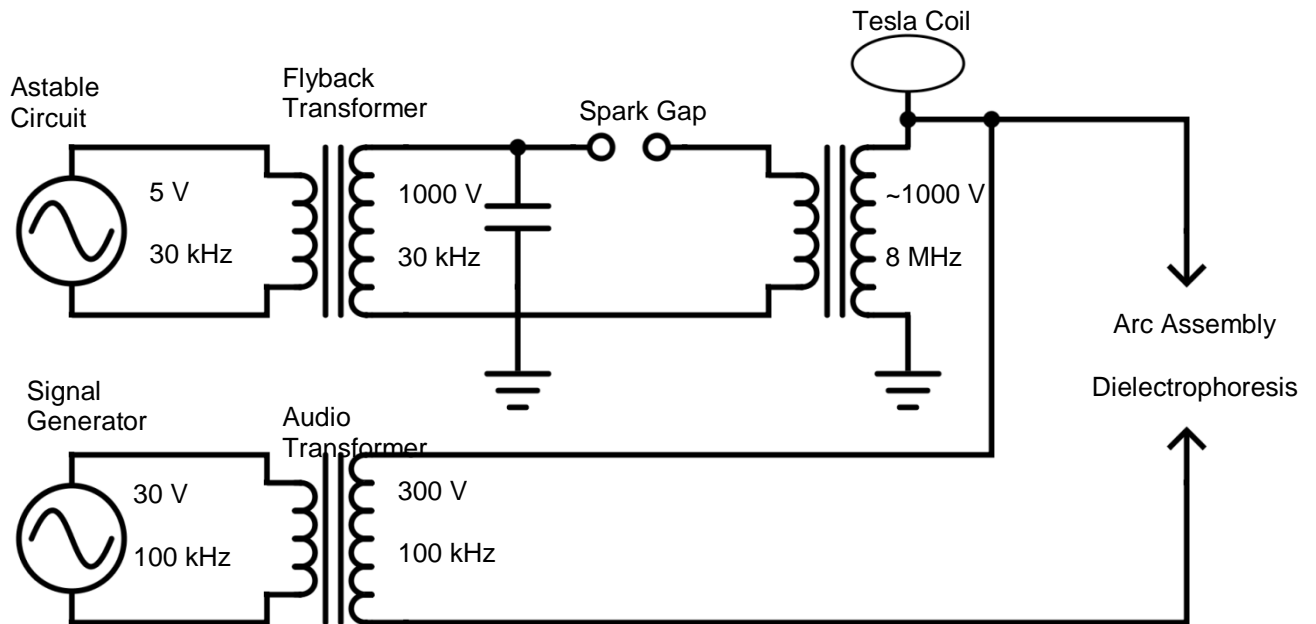
The graph serves to illustrate the region in which arc assembly is most effective during experimentation, the drop off at higher frequencies is expected to be due to the Q-factor of the circuit but may also be due to multiple layer Maxwell-Wagner relaxations (which may possibly be expected in MWNT of different chiralities).

Note the region of arc assembly varies greatly on particle/medium permittivity and conductivity. In some cases dipole chains were still observed when  $\text{Re}(K)$  was less than 1 and could still bridge the electrodes, however this effect was always temporary.

## 4.4 Arc Assembly Implementation

### 4.4.1 Intermittent Arc Assembly Circuit

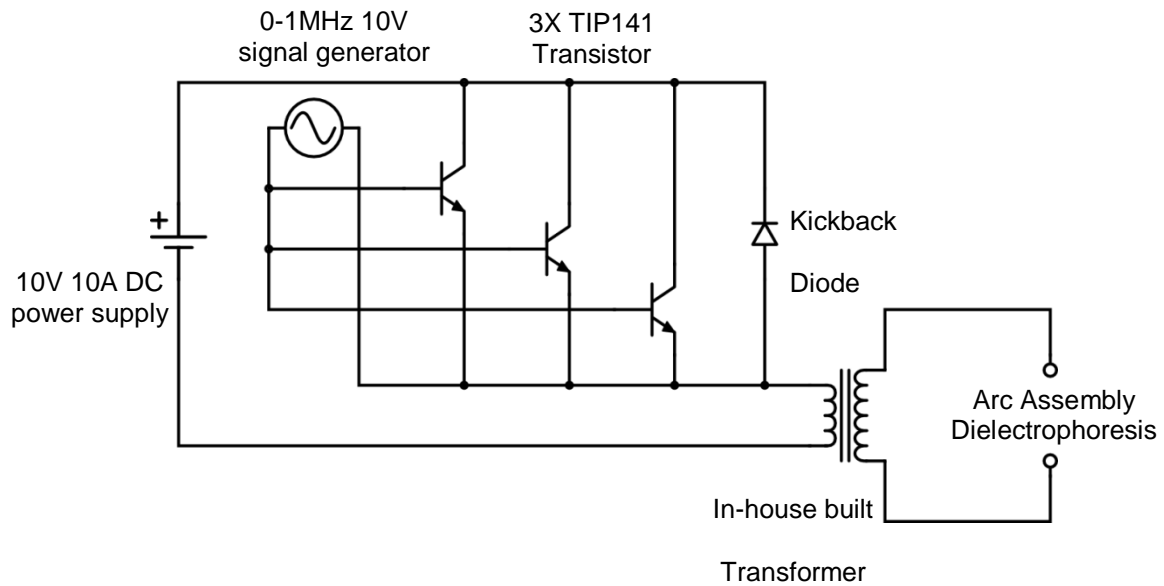
The design for circuits to focus on the  $\sim 100\text{kHz}$  region was not entirely due to the observed increase in arc assembly in this region but due to the limitations of constructing an in-house high voltage, high frequency circuit. A Tesla coil circuit was designed to overcome this problem, figure 4.4. Initially a circuit that amplified the voltage from 30V to 300 V from a signal generator at 100 kHz was used to obtain, the results shown in Figure 4.6. However 100 kHz at 300 V is close to the minimum requirements for Arc Assembly, and may not provide a strong enough dielectrophoretic force, or energetic arcs. To supplement this circuit a small Tesla coil was constructed with a resonant frequency of 8 MHz and voltage in the order of 1000 V. This was directly added to the continuous 100 kHz signal and creates impulses. The impulses prevent excessive fluidic motion that would otherwise be observed for an 8 MHz signal. The overall circuit can be seen in Figure 4.4.



*Figure 4.4.* Schematic of circuitry used for arc assembly. Astable circuit is prefabricated and not included. All grounds are earthed via the same connection

#### 4.4.2 Continuous Arc Assembly Circuit

For continuous arc assembly, a high voltage high frequency circuit needed to be designed, with an emphasis on greater current output. The previous circuits (Figure 4.4) achieved high voltages and high frequencies, which was enough to show that intermittent Arc Assembly could occur, however continuous Arc Assembly requires that a single arc is maintained over a prolonged period of time.



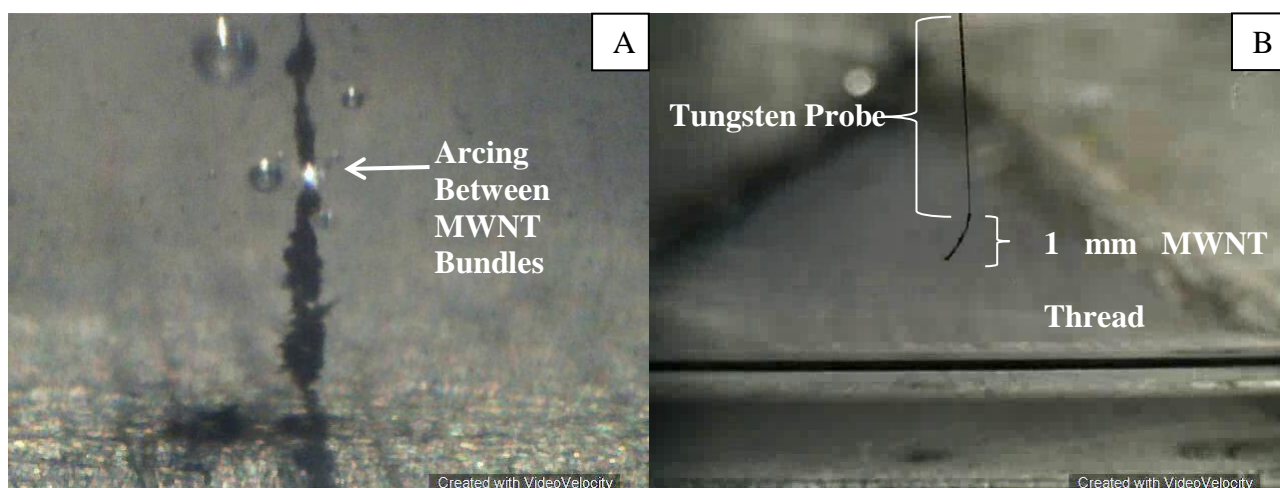
*Figure 4.5.* Circuit diagram for single wave high voltage high frequency arc assembly

Figure 4.5 shows a ‘redundant’ common emitter circuit. The common emitter is a simple amplifier typically used in radio frequency applications. The purpose of the circuit is to amplify the signal generator signal with a 10 A power supply to drive an in-house wide band transformer. The transformer has winding impedances primary:  $11\ \Omega$  secondary  $112\ \Omega$  both with 28 Gauge wire in a single ferrite core shell arrangement. The circuit typically takes a 10V of 0 – 1 MHz signal to approximately 500V. Three transistors were used to distribute the current and prevent overheating, in addition to  $50 \times 30 \times 10$  mm heatsinks attached to each transformer and an additional cooling fan run over them. A 10 A kickback diode is also placed over the 3 transistors to prevent inductive surges which can damage the transistors.

### 4.4.3 General Arc Assembly Mechanism

A mechanism for creating a multi walled nanotube (MWNT) threads has been observed and is described as follows:

1. A tungsten probe is immersed in ~10 ml of insulating liquid medium with ~10mg MWNTs dispersed over an aluminium electrode.
2. A 300 – 1000 V , 0.1-8 MHz signal is applied between the 2 electrodes.
3. Dielectrophoresis aligns MWNTs beneath the tip in a loose bundle.
4. As the bundles accumulate at a distance ~10  $\mu\text{m}$  the medium breaks down and an arc occurs as in Figure 4.6 A.
5. This arc bonds the nanotube bundles together at this point and short circuits the electrodes.
6. With no DEP force holding the MWNTs in place the bundles drift apart.
7. As the bundles separate the circuit is opened again and another arc breakdown occurs.
8. This mechanism repeats until the entire length of thread is strong enough to remain intact during the short circuit (i.e with no DEP force holding them together).
9. The tungsten probe may then be withdrawn by a short distance (~20  $\mu\text{m}$ ) to create a new gap in the thread and allow MWNTs to accumulate, and this mechanism repeats.
10. Ultimately the thread may be removed from the fluid without the assistance of DEP, as this mechanism strengthens the thread at any point which would otherwise collapse without a DEP force. This is observed in Figure 4.6B



*Figure 4.6.* A) Arc breakdown between a thread formed on the counter electrode and a thread attached to the tungsten probe B) CNT thread removed from the dispersion adhered to tungsten probe.

Continuous Arc Assembly has been observed to follow the same observed mechanism as intermittent Arc Assembly with the exception of point 5. Where, instead the bundles of CNTS do not form a short circuit due to the high intensity of the arc discharge or greater fluidic movement. CNTs gradually adhere onto the probe tip and form a thread, and the arc discharge is maintained by manually withdrawing the tip as more CNTS adhere. A 5 mm completed CNT thread from Continuous Arc Assembly may be seen in Figure 4.7.

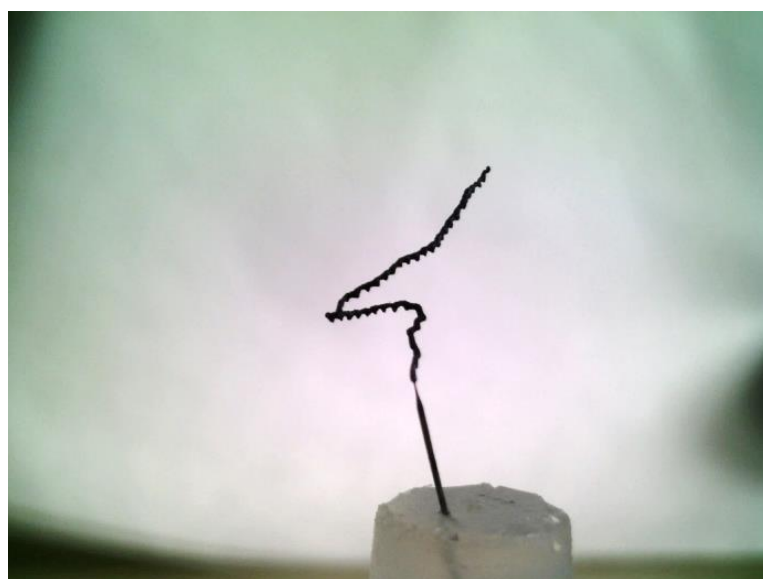


*Figure 4.7.* A 5mm continuous Arc Assembled thread attached to a tungsten probe

## 4.5 COMSOL Models of Electric Field Strength

### 4.5.1 Principles of Model

To provide support for the theory behind the dielectrophoresis experiments, a 2D COMSOL model was produced to establish parameters which were deemed important for influencing the electric field gradient. These include the droplet shape, probe sharpness, and electrode separation. In addition, the model can be adjusted to resemble observations made in experiments so inferences to an experiments outcome may be obtained.

The model consists of 4 main parts (refer to Figure 4.8)

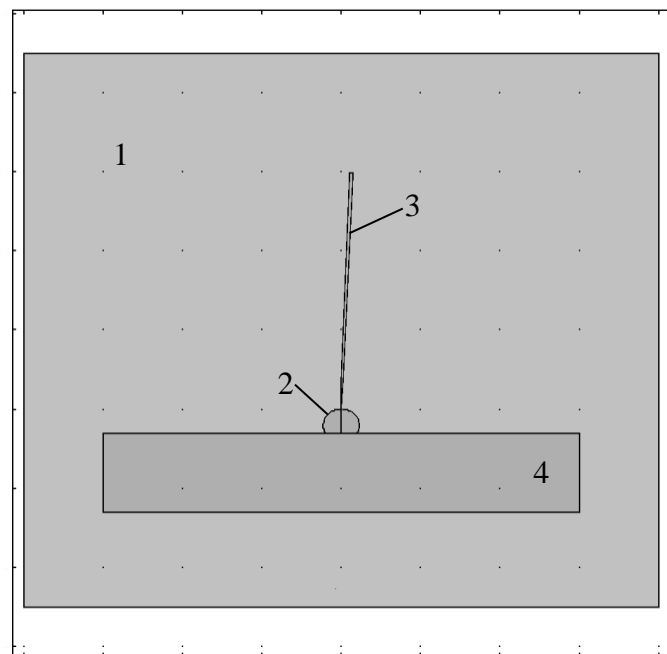


*Figure 4.8.* The structure of a COMSOL Model for assessing electric fields over a droplet.

The 4 objects of this model may be referred to in the following text.

1. The background atmosphere which is air and cannot be changed

2. A droplet where the following can be changed:
  - a. Volume of liquid
  - b. Surface tension of liquid
  - c. Type of liquid (this changes just the electrical constants)
  - d. Wettability of liquid (Contact angle)
  
3. A probe where the following can be changed;
  - a. Probe tip radii
  - b. Probe aspect ratio
  - c. Probe angle
  - d. Probe material
  - e. Probe separation distance (from substrate)
4. The metallic substrate strip of changeable material enlarged to a block significantly bigger than either the probe or droplet this cannot be changed

#### **4.5.2 Substrate and Atmosphere**

Modelling of the substrate and the surrounding atmosphere was trivial and they both consist of 2 rectangles. The atmosphere is 3.5 x 4 mm whilst the substrate is 3.0 x 0.5mm. These dimensions do not correspond to the actual scale but for the convenience and simplicity of the model these dimensions are used. The atmosphere has a relationship to the model to maintain its centre about the probe's tip irrespective of the tips angle. The substrate can be moved vertically in relation to the probe's tip. It should be noted that this entire model holds the tip stationary whilst the model's relationships move around the tip – this may be contrary to what happens in actual experiments but for the sake of modelling the geometry it is assumed that this will not make a difference.

### 4.5.3 Geometry of the Droplet on a Surface

The droplet's shape is more complex and requires a model which can allow for alterations wettability angle, surface tension and volume. The droplet's overall shape can be simplified to 2 identical circles within a larger circle whose circumference coincides with those of the 2 smaller circles. The droplet shape is constructed by then removing the portion of the larger circle outside the 2 small circles but between the point of contact with the circumferences and the surface. This is shown in Figure 4.9

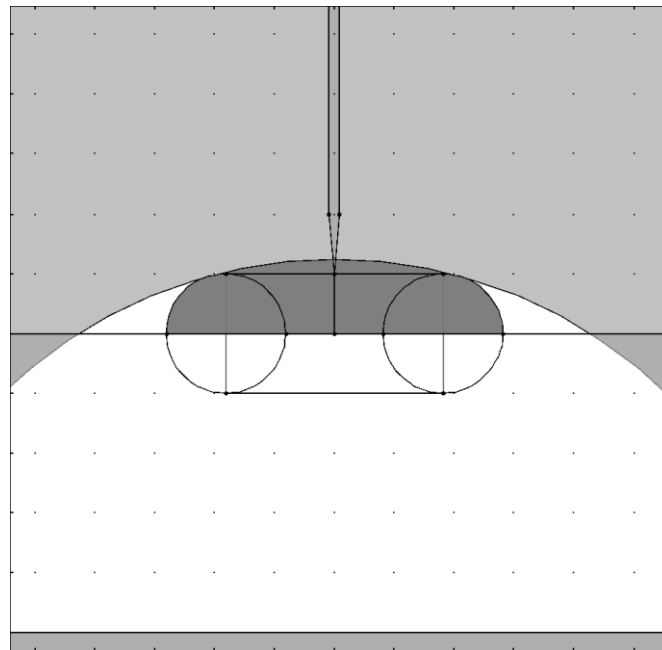


*Figure 4.9.* COMSOL components for modelling a droplet. The dark grey region is the final droplet formed by the intersecting 3 circles (2 small, 1 large)

For a very large volume of liquid the height of the droplet can be assumed to be constant for a given surface tension and wettability by equation 4.3:



$$Height = \sqrt{\frac{2 \times SurfaceTension \times (1 - \cos(ContactAngle))}{Gravity \times Density}} \quad 4.3$$

However, as the droplets being measured will be of 100 µl or less this equation does not hold and instead the surface tension, volume and contact angle are modelled separately and are based on observed dimensions instead. However a relationship between the circles discussed for modelling an overall droplet shape and these separate parameters must still be constructed to ensure the geometry holds for any change implemented on these parameters.

To ensure the point of contact on the smaller circles to the substrate matches the given angle trigonometry is applied to find the correct positioning of these smaller circles. The point of contact between the circumference of the larger circle and these 2 smaller circles is found by projecting the angle to the point where the gradient is the same on both circles. The larger circle is then repositioned to this point. This contact point for the size of droplets in these experiments is a combination of volume and surface tension, the exact relationship is unknown for this model. A diagram showing how the 2 angles connect from the smaller circles to the larger circle and the substrate is demonstrated in Figure 4.10.

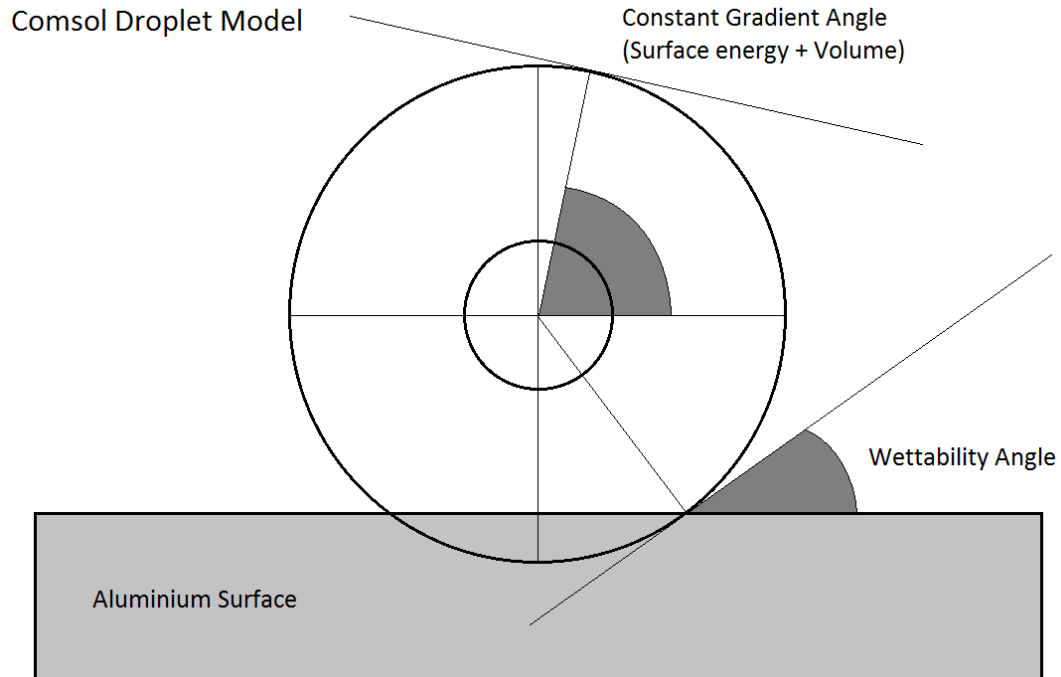


*Figure 4.10.* Part of geometry used to merge circles within model to form droplet shape

#### 4.5.4 Geometry of the Probe

The probe is modelled as a rectangle with a triangle attached to it with a circle cropping the point of the triangle to form the probe tip as shown in Figure 4.11

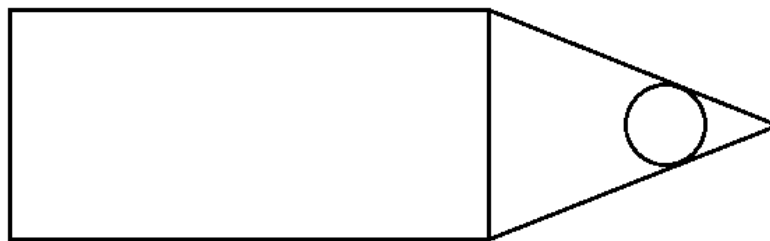


*Figure 4.11.* Geometry used to construct overall probe

As mentioned the model is orientated with the probe tip at the centre. However as the tip radius changes this point moves and the model must be adjusted to maintain parameters such

as the gap distance between the substrate and probe. Also as the tip radius changes the aspect ratio of the tip - defined by the length of the triangle - must join the circular tip at the same point of gradient on the circle. This leads to the following relationship within the probe geometry:

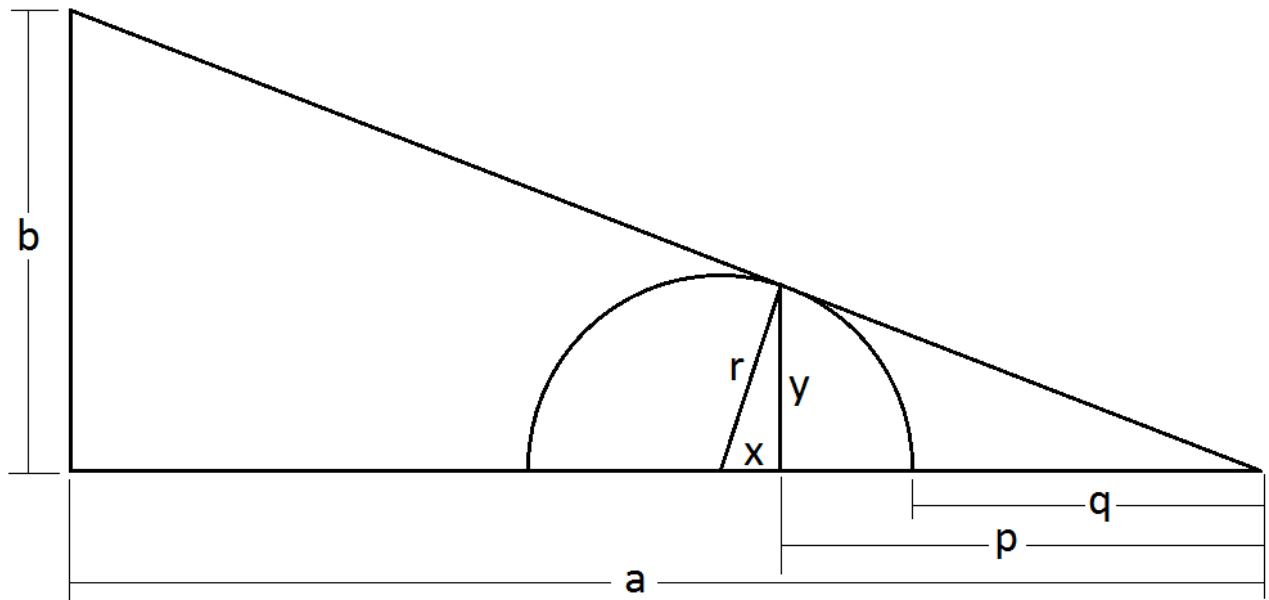


*Figure 4.12.* Geometric parameters used to calculate the difference in probe length with changing tip radii

Looking at half of the probe, given a fixed gradient for the triangle defined by the length of the triangle  $a$  with the height of the triangle  $b$  as  $g$

$$g = \frac{b}{a} \quad 4.4$$

For the point where this gradient intersects the circle it is :

Equation of circle:

$$x^2 + y^2 = r^2 \quad \rightarrow \quad y = \sqrt{r^2 - x^2} \quad 4.5$$

Gradient of circle:

$$\frac{dy}{dx} = \frac{-x}{\sqrt{r^2 - x^2}} \quad 4.5$$

Thus the intersection from the origin of the circle is:

$$g = \frac{-x}{\sqrt{r^2 - x^2}} \rightarrow g^2 r^2 - g^2 x^2 = x^2 \rightarrow \sqrt{\frac{g^2}{1 + g^2}} \times r = x \quad 4.6$$

To measure the amount needed to be adjusted from the triangle to leave just tip the radius a distance  $q$  needs to be removed from the model, and thus  $y$  and then  $p$  need to be found:

$$q = p - (r - x) \quad 4.7$$

$$y = \sqrt{r^2 - x^2} \quad 4.8$$

$$p = \frac{1}{g} \times y \quad 4.9$$

Substituting  $y$  into  $p$  and then  $p$  and  $x$  into  $q$  we obtain:

$$q = \frac{1}{g} \times \sqrt{r^2 - \left(\frac{g^2}{1 + g^2}\right)r^2} + \sqrt{\frac{g^2}{1 + g^2}}r - r \quad 4.10$$

Thus by moving the model by a value of  $q$  the tip of the probe will always remain in the same point regardless of how the other tip parameters change.

For this thesis the model has been presented as a way of accurately depicting changing tip radii to a fixed distance – it is hoped a similar effect may be useful for modelling sharpening processes, however this would also involve introducing a relationships for a  $\Delta q$  based on an electrochemical “modifier” for the electric field subsequently described.

## 4.6 Findings and implications from COMSOL simulations

### 4.6.1 Matching Simulation to Experiments

With the adjustable relationships for the different sections of the model it was possible to reconstruct an experiment with the probe in a droplet to the dimensions measured from a microscope.

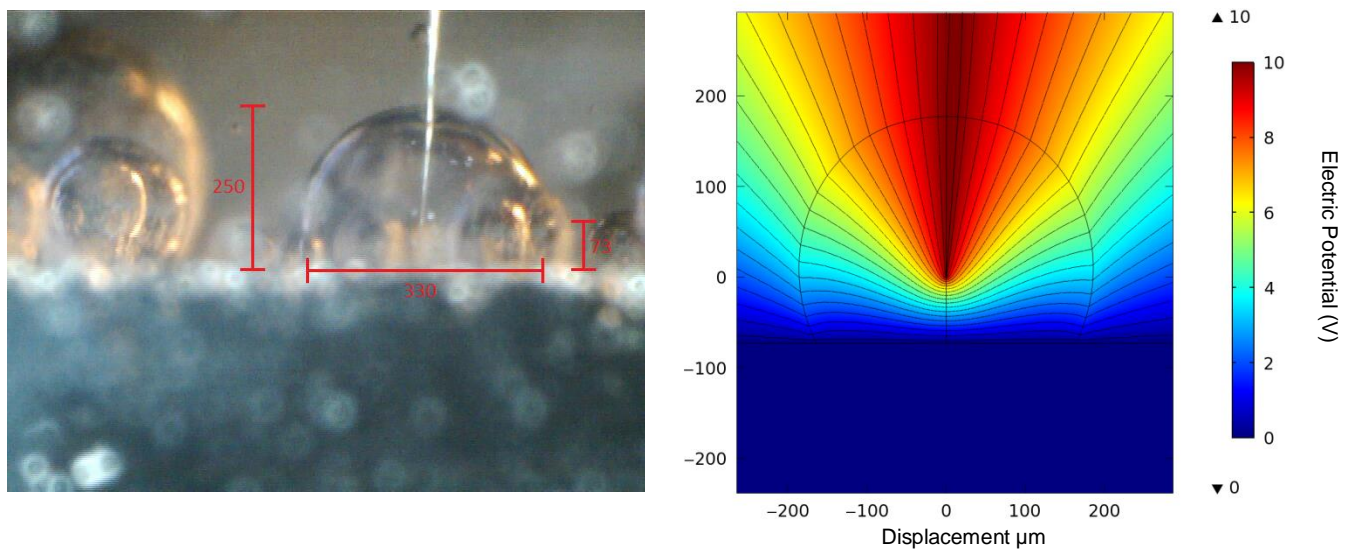


*Figure 4.13.* COMSOL model used to represent dimensions as occurred in an experiment

Figure 4.13 shows a microscope image with dimensions added and the corresponding COMSOL model which has been adjusted to the same scale. The overall height of the bubble was measured in ImageJ to be 250  $\mu\text{m}$  with a diameter of 330  $\mu\text{m}$  and a contact angle of  $60^\circ$ . The separation between the electrodes was 73  $\mu\text{m}$  and the probe sharpness had a gradient of  $1/25$  (width/height), the radius was modelled at 100 nm and an angle of  $2.5^\circ$  to the vertical axis. Figure 4.13 shows the electric field distribution between the tip and the counter-electrode. This shows that it is possible to reconstruct the 1D and 2D electric field distribution present in the experiment and thus calculating parameters such as the forces

experienced by surrounding CNTs should be possible in the future stages of this project. Furthermore analysis directly underneath the probe can be obtained and theoretical distributions for a range of parameters in the same situation can now be made.

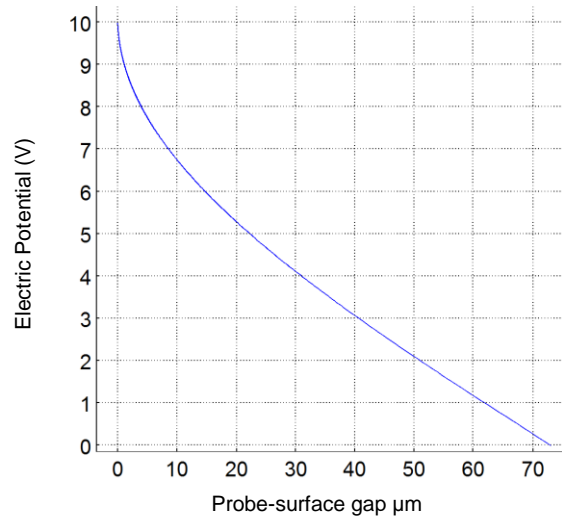


*Figure 4.14.* Graph of electric potential distribution for model used in Figure 4.13

#### 4.6.2 Electrode Distance Analysis

Fig. 4.14 shows graphs of the gradient of the electric field immediately beneath the probe tip for the first 500nm. The graphs are measured for various separation distances between the tip and counter-electrode. The magnitude of the gradient has a direct link to the force of the dielectrophoresis as mentioned previously.

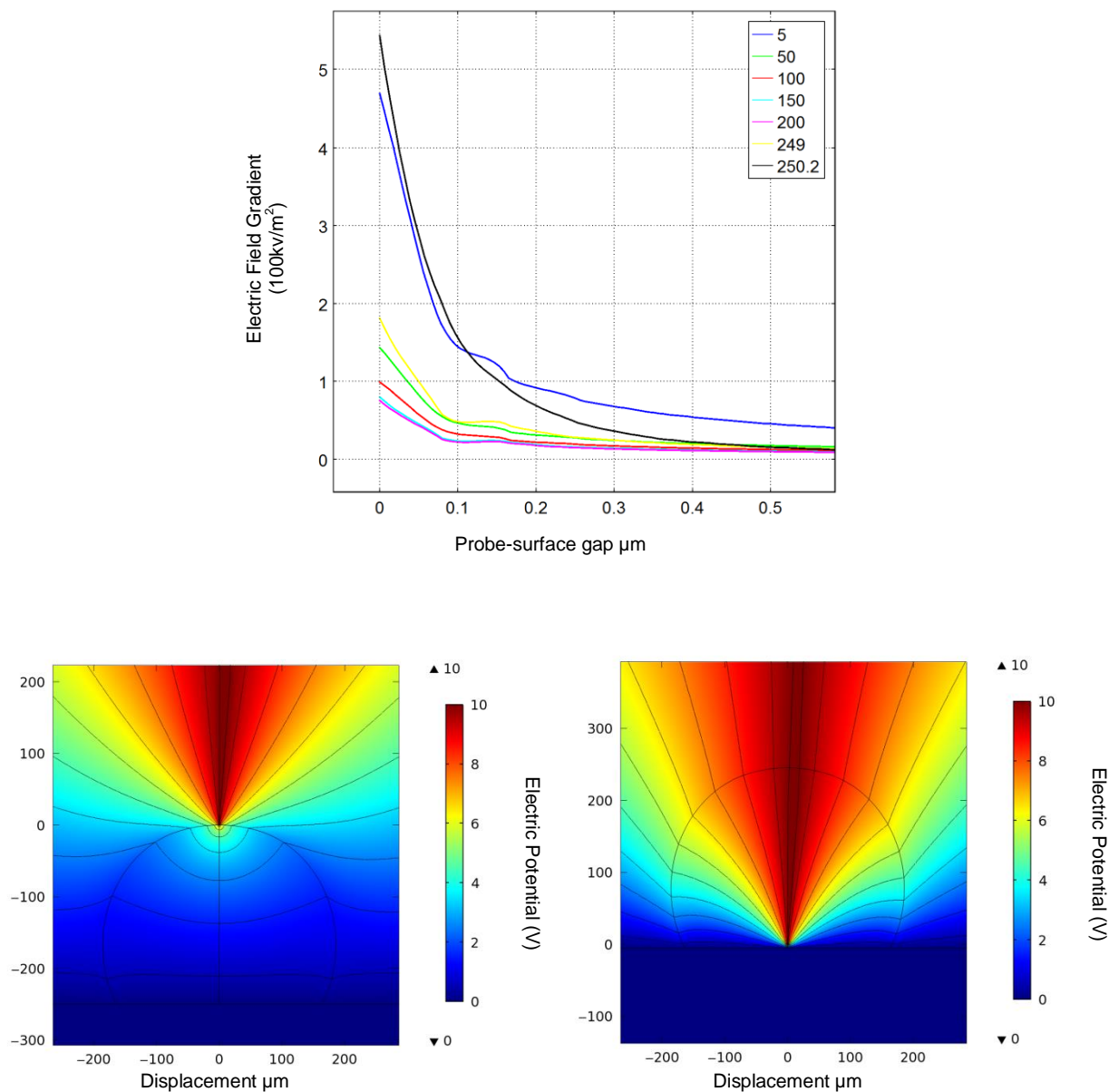


Figure 4.15. Distribution of electric field gradients for varying plasma gaps

The COMSOL model shows that as expected there is a higher gradient approaching the counter-electrode, but also surprisingly a high gradient at the tip of the bubble surface – this is due to the electric field being dropped over the curvature of the bubble – which changes the gradient. Figure 4.15 shows a 2D representation to compare these differences. This may provide a new point for attaching CNTs at a safer distance from the counter-electrode whilst not sacrificing the strength of the dielectrophoretic force. Insights such as this may prove

useful for later experiments in the project and help justify the use of modelling to aid experimentation.

#### 4.6.3 Probe Sharpness Analysis

Further simulations were carried out to find out to what extent the tip radius influenced the electric field gradient. As would be expected according to gauss's law the smaller the tip radius the greater the electric field strength towards the tip.

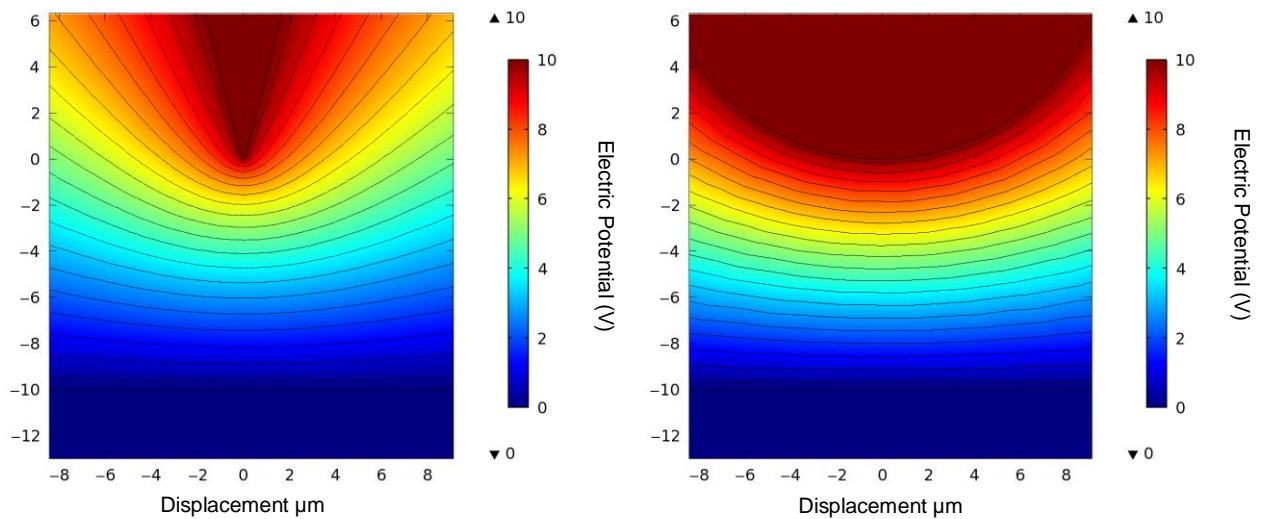


*Figure 4.16. Electric field distributions for changing tip radius at 100nm and 10 $\mu\text{m}$*

These simulations confirm this, and allow models to be produced for dielectrophoresis calculations where the field gradient will be largely controlled by the tip radius produced from the electrosharpening experiments discussed in Chapters 2 & 3. In addition to this the measurements show that the probe geometry is likely to have a strong influence over the DEP process within the model given the difference in probe size, that can be seen in Figure 4.16 and the expected results produced in Figure 4.17.



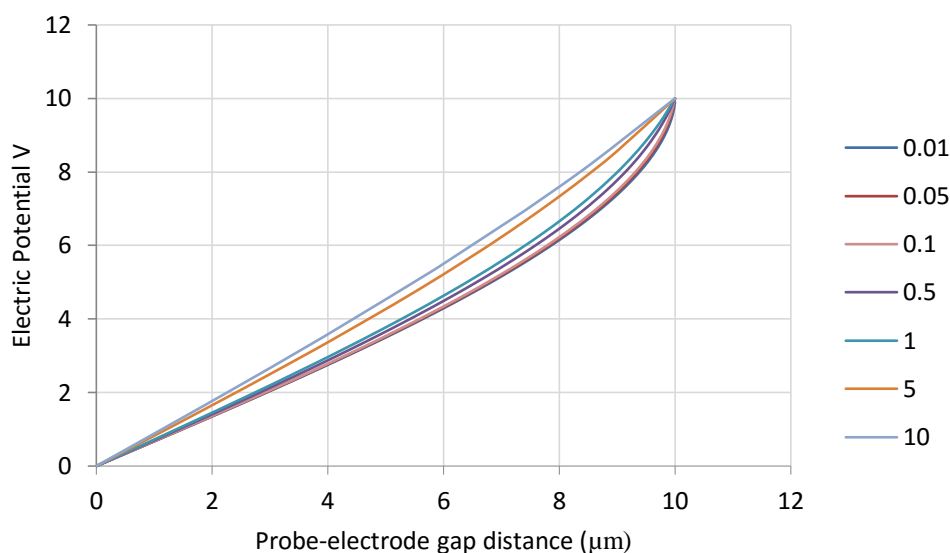


Figure 4.17. Graph based on COMSOL model of electric field for a variety of tip radii

#### 4.6.4 Preliminary SEM Results

To further guide experimentation SEM images were taken of threads created via intermittent arc assembly shown in Figure 4.18. Of particular interest was the extent and crystallinity of the adhesion, and the influence of the fluid medium (in this case, oleic acid). An analysis of the SEM images from Figure 4.18 and the implications for further experiments follows:

(A) & (B) Show an extensive porous network of MWNTs. The thread measures >1mm however is curled up slightly. It has been found that the threads can be ‘unfurled’ by application of more than 500V DC to create electrostatic repulsion within the thread, but they collapse after the voltage is removed. The thread is strong enough to remain attached to the tungsten probe and moved manually, but has not been tested for mechanical strength.

(C) In the foreground shows a group of nanotubes that are linked together over a length greater than the 10 μm length of the MWNTs used. This implies that the MWNT are not

changing in shape, but are attaching together. In the background the image shows an amorphous structure with nanotubes visibly contained within it. Either the nanotubes are breaking during the process, and reforming as an amorphous material, or additional material is being added from the oleic acid.

(D) Indicates a clean Y-branch, possibly between 2 or 3 nanotubes. Y-branching in nanotubes is well established in the literature, and typically exhibits a continuation of the  $sp^2$  crystal structure. Although this image does not confirm such a structure, the lack of any obvious amorphous structures makes this a possibility. Such bonding is highly sought after as this extends the characteristics of the MWNT, whereas an amorphous joint would likely cause a break in the continuation of any characteristics.

(E) & (F) Show what are thought to be MWNTs that are linked together, but the nature of the bonding is unclear. However, the surface of the MWNTs in (5) appears to have obtained a roughness not attributed to many of the others. In (6) the MWNTs have a different surface structure, where a complete covering of growths have formed. It is unclear as to why such structures would occur, however it is unlikely to possess the typically desired characteristics of the MWNTs.

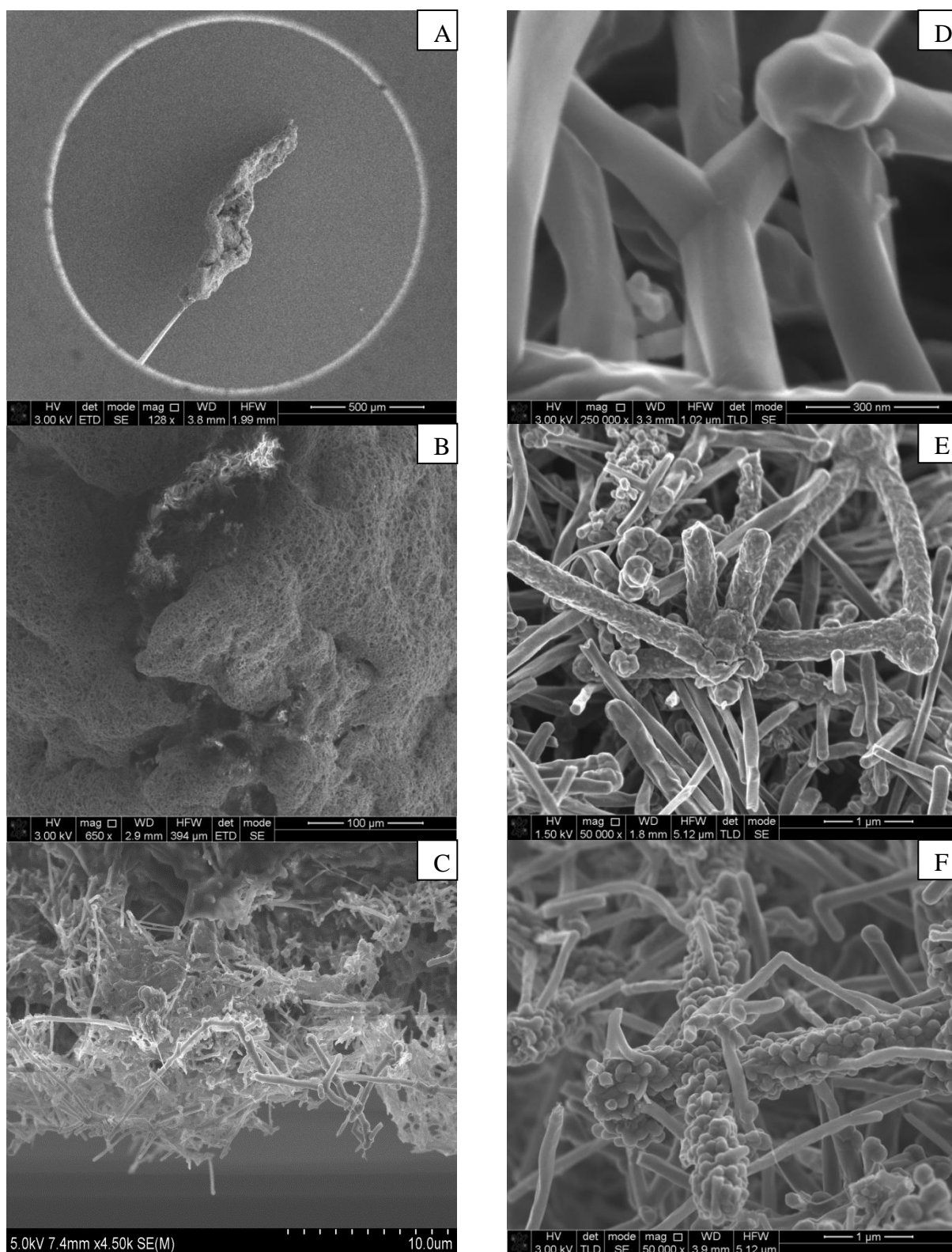


Figure 4.18. SEM images taken over a single  $\sim 1\text{mm}$  thread of intermittent arc assembled carbon nanotubes.

#### 4.6.5 Evidence for Fluidic Motion Within Continuous Arc Assembly

Given the high electric field generated by the tungsten probe and propagated by the MWNTs within the solution it was demonstrated that a continuous arcing process could be applied to create very long threads up to  $\sim 5$  mm in length. Figure 4.2 (section 4.3) shows a sketch of how the MWNTs move within a positive DEP force. Here figures 64 and 65 shows forming a vortex around the plasma region where the MWNTs are fused together. This fluid motion combined with the high current delivery of the redundant common emitter circuit shown in Figure 4.5 and a constant probe gap separation allows the arc assembly to avoid the intermittent nature previously described. Furthermore, because of the high temperature due to the much larger plasma region (shown in Figure 4.19) the threads appear stronger within the solution.



*Figure 4.19.* Left: The larger plasma region, the 0.25 mm wide tungsten probe can be seen in the centre top of the image. Right: the random motion of the arc assembled thread due to fluidic motion is seen leaving arc-eroded marks on the protective copper tape.

Further evidence for the vortex within continuous arc assembly is seen in Figure 4.20. The Lichtenberg figures on the surface of MWNT suggest the arc is composed of multiple smaller

arcs, and the arcs are spreading tangentially to the direction of thread removal. However, this is only indicative of the end of the thread where the arc assembly naturally stops.<sup>37</sup>

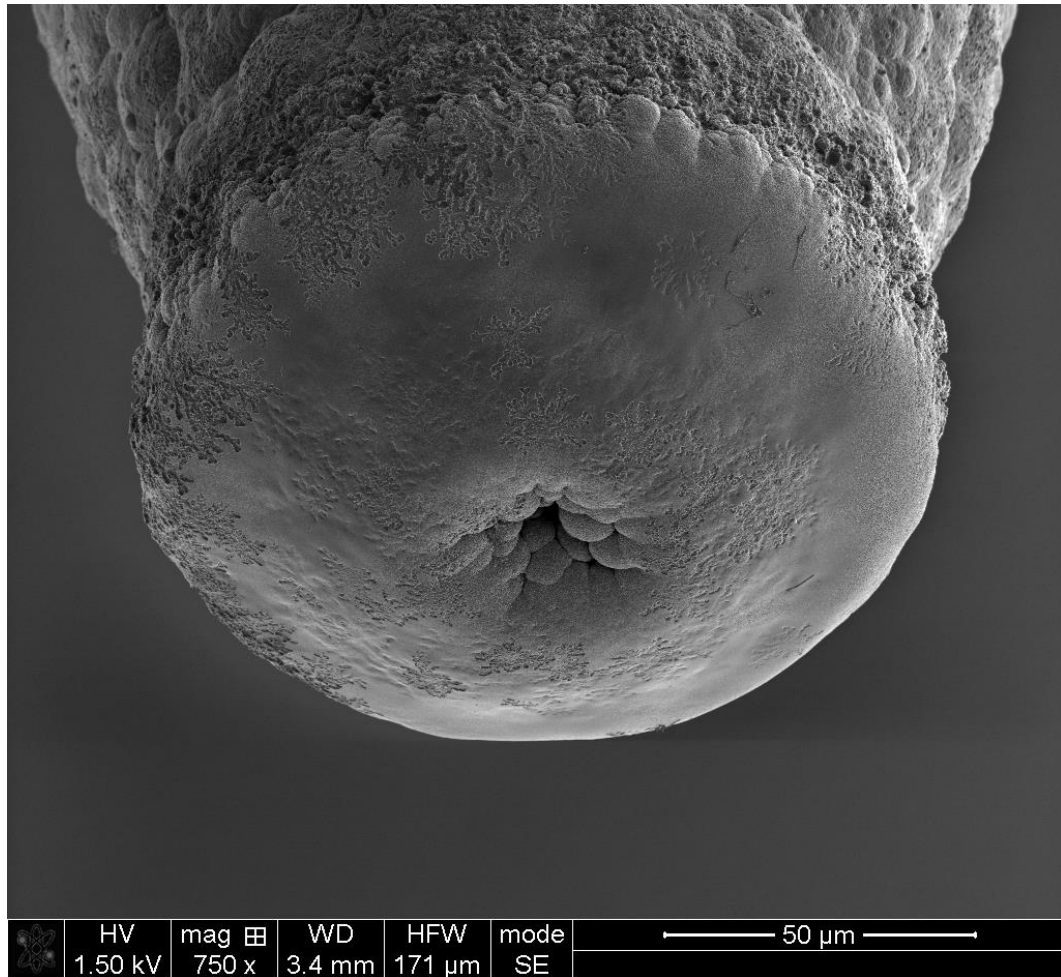


*Figure 4.20. End of Arc Assembled CNT thread*

Also of interest is the hole present in the base of the thread which appears to be a common characteristic for arc assembled threads. It is proposed to be a result of the vortex created within the plasma/fluid creating a vacancy of particles as they are pulled towards and then pushed away from the centre of the thread due to the motion of the fluid/plasma. Other complex holes have been observed not just at the base of the thread as seen in Figure 4.20 suggesting the vortices may be creating micro-fluidic tunnels within the threads.<sup>38</sup>

#### 4.6.6 Initial Electrical Measurements

Measurements of the in-situ resistivity of the OMCTS polymer thread were taken during the arc assembly process. It was observed to maintain an irregular resistance that lay between 2-3 k $\Omega$  for the duration of the process when measured between the tungsten and counter electrodes.

Further electrical measurements were taken of the triglyceride sample showing resistive values ranging from 50 k $\Omega$  to 290 k $\Omega$  depending on the position of the electrodes (the electrodes were kept at 1 mm distance). For comparison a single dielectrophoretically suspended chain of nanotubes over a length of 1 mm has a resistance of 900 k $\Omega$ . These values are similar to the literature's values for undoped CNT fibres. No measurements could be taken of the OMCTS thread due to the thick external polymer layer.

The irregularity of the measurements implies that the carbon thread may possess multiple conducting pathways between the electrodes. The most conductive route is found directly between the tungsten and counter electrodes which would occur due to the self-propagating system of assembly.<sup>39</sup>

These findings for the electrical measurements provide evidence for the arc assembly mechanism as it is dependent on at least partial conductivity of the thread assembled. In addition to this it suggests that these threads may find applications within electronic and electrical applications.

## 4.7 Arc Assembly TEM

*Figure 4.21 A – D are from a variety of sites on an MWNT and Oleic acid triglyceride thread similar to the one shown in Figure 4.18.*

(A) Shows a series of aligned nanotubes connected between two amorphous regions, possibly to a much longer nanotube running horizontally beneath them. This may indicate uniformity in the adhesion as multiple MWNTs have attached in the same manner and approximately the same alignment over this region. Alternatively, this may indicate that multiple MWNTs participate in the same adhesion simultaneously during the process.

(B) Two separate MWNTs (lighter shaded in the background) are visible with strands of solid amorphous material between them. This provides evidence that the amorphous material binds the nanotubes together. Additionally it suggests that the MWNTs are coated to some degree with the material, which could not be removed with IPA.

(C) A series of amorphous joints between MWNTs in a complex formation with multiple nanotubes connecting at the same joint can be observed. The joints contain a mixture of amorphous and crystalline structure. This shows adhesion between MWNTs which has occurred without being embedded within the amorphous material.

(D) This is a higher magnification of one of the joints in (C). The joint is crystalline with some amorphous material surrounding it. The joint appears similar to Figure 4.21 D, which may indicate crystalline joints can occur in combination with amorphous material either forming with the joint or coating it. This may also indicate that the apparent amorphous bonds observed in the SEM images have crystalline components.

*Images E – H are from two sites which showed exposed MWNTs. Typically most of the nanotubes were embedded within the OMCTS polymer and could not be imaged.*

(E) This image shows a fragment from CNT + OMCTS thread after grinding. This particle gave an opportunity to image exposed nanotubes for indications of crystallinity and the nature of it merging with the polymer in close proximity. Two nanotubes are visible with a third possibly coated in amorphous material also overlapping the crossing point.

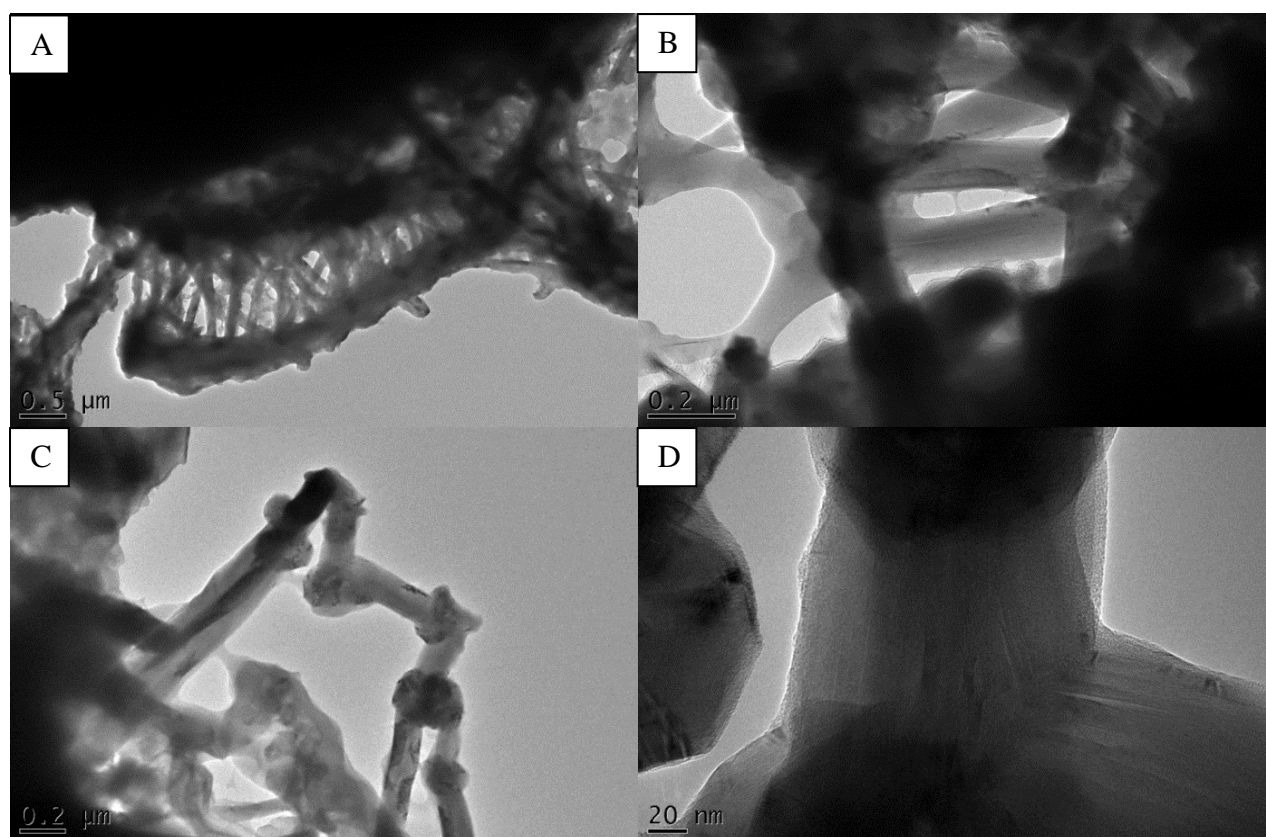
(F) Shows a view of a single MWNT merging with amorphous material at a different site. The amorphous material appears similar to the particulate site in (E). The MWNT is also partially embedded within the material with no indication of connecting to any other MWNT.

(G) The crystalline structure of the MWNT can be observed adhered to the amorphous material. The crystalline structure continues without break beyond this region which provides further evidence that the structure of the MWNTs is not significantly damaged by the process.

(H) Shows a cap of one of the MWNTs in (E). The cap has a crystalline structure, however there is also amorphous material at the top, this may be a localised coating, or a by-product from the deformities associated with MWNT capping. However, it may also indicate a region where arcing has occurred at the top of the MWNT forming a deposition of amorphous material.



# CNT + Triglyceride Polymer



# CNT + OMCTS

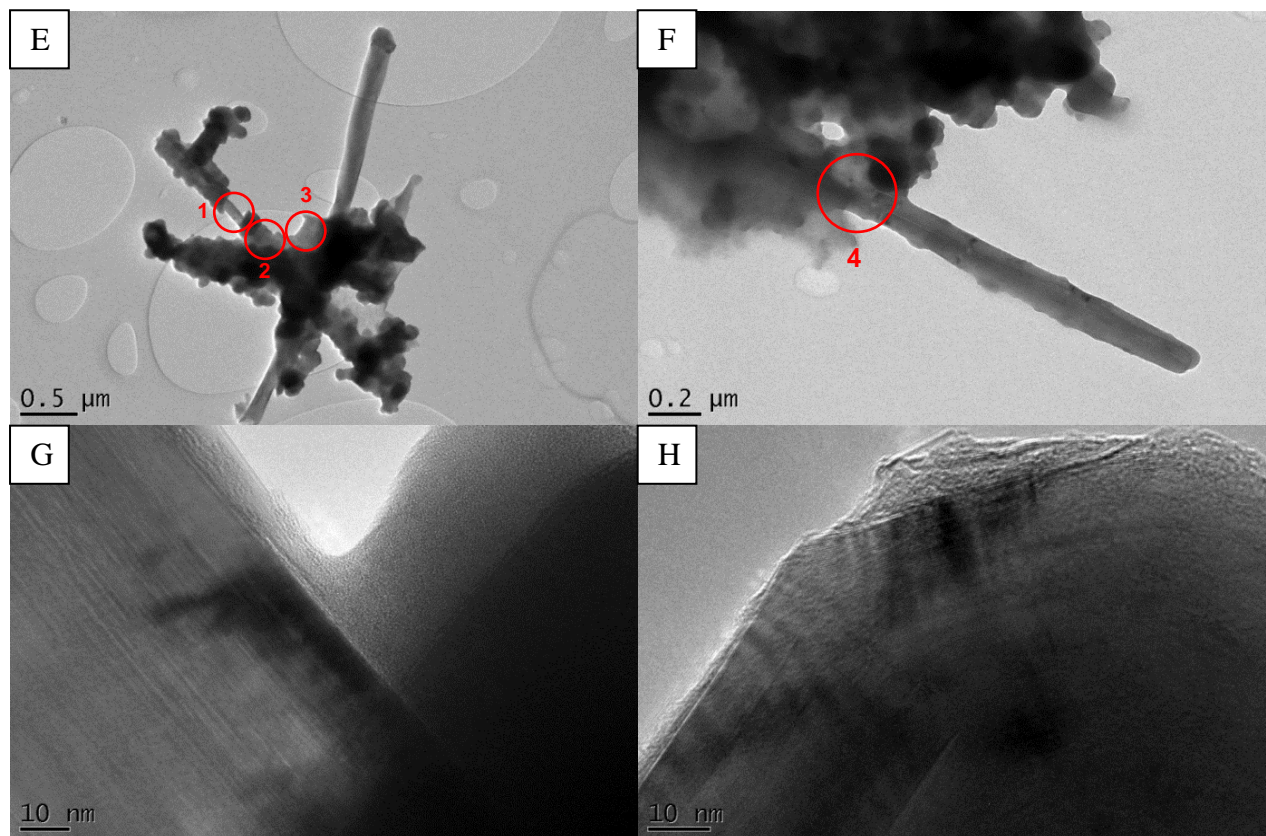
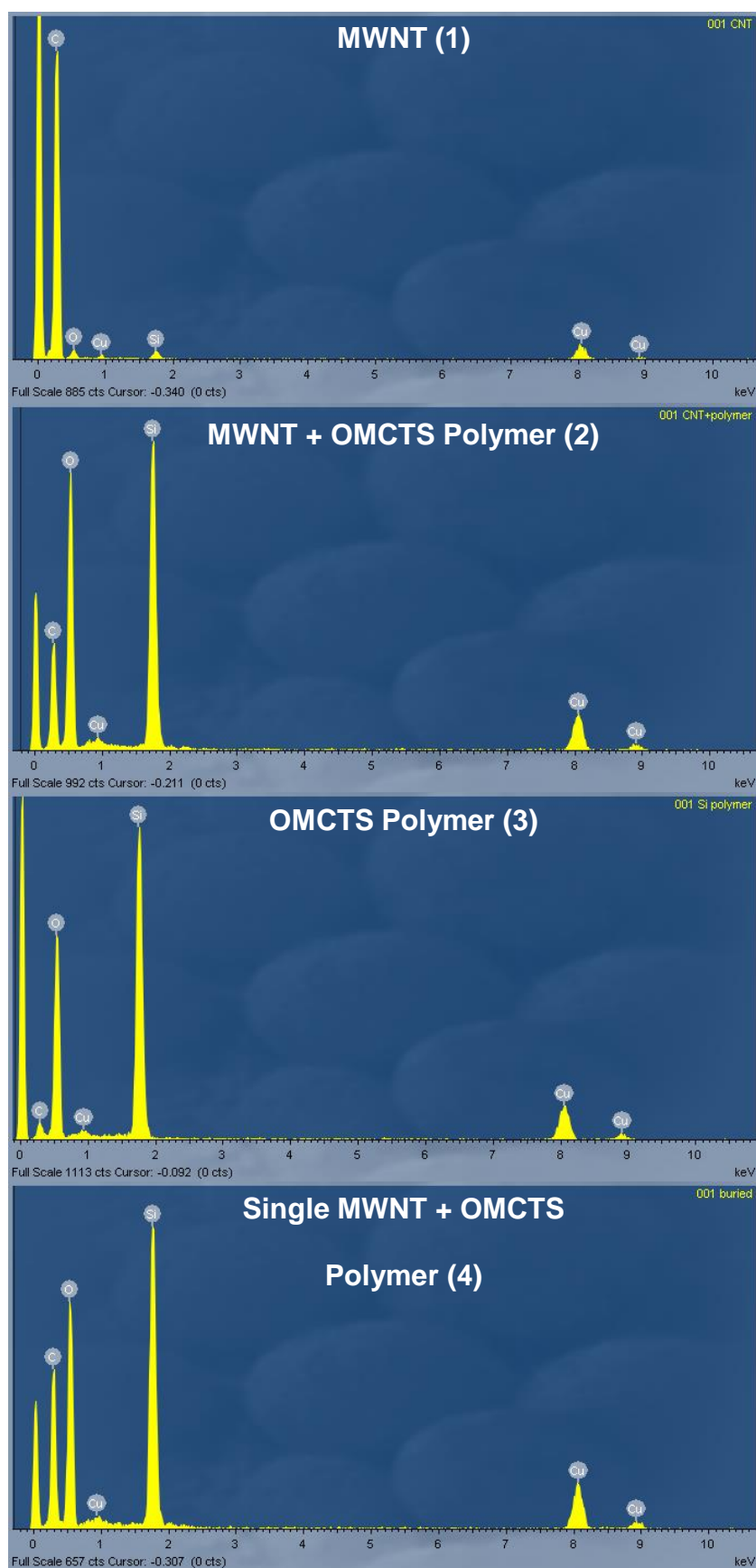


Figure 4.21. A selection of TEM images of MWNTs in Triglyceride and OMCTS polymer. The red circles indicate the regions for the EDX spectra in Figure 64.

## 4.8 EDX Spectroscopy of TEM results

Energy Dispersive X-ray (EDX) spectra (seen overleaf in Figure 4.22) were obtained from the fragment of MWNTs and OMCTS polymer shown in Figure 4.22 E & F, the red circles are the sites used. The data was taken from the silicon polymer to provide a difference in the spectra to indicate the presence of the polymer instead of amorphous carbon – which may be similar in appearance. Thus, no EDX data was obtained for the triglyceride based thread, as only carbon would be observed. The CNT (1) EDX spectrum shows only the presence of carbon, with trace elements of silicon, which may be detected from surrounding material outside the target site. This indicates that the MWNTs have maintained a high level of carbon purity, and have not been contaminated by the process. Furthermore, the MWNTs may not always be coated by the OMCTS polymer, despite being completely immersed in the liquid – suggesting that polymerisation may only occur at specific sites of the MWNT. However, it is possible that during the preparation of the sample, particularly the grinding; parts of the polymer were removed leaving sections of the MWNT exposed. The MWNTs + OMCTS polymer (2) spectra show the presence of the MWNT within the polymer, confirming that the two materials are merged or embedded together and there is a significant depth to this, i.e the MWNTs are not just protrusions starting at the edge of the amorphous material. The OMCTS Polymer (3) spectra shows only trace amounts of carbon. This suggests that the amorphous material is almost entirely a product of the OMCTS polymer and very little of the MWNTs are being damaged to form amorphous carbon. In addition, the carbon component of the polymer may have been removed during the process. The Single MWNT + OMCTS polymer (4) spectra was taken at a different site to (1 - 3) to confirm the previous EDX data and as a further indication that the amorphous material combining with the MWNT is not entirely amorphous carbon.



*Figure 4.22.* EDX spectra taken from the sites highlighted in Figure 4.21. The sites were selected to indicate the chemical composition of the thread as MWNTs merge with the amorphous material.

## 4.8 TEM Electron Diffraction Patterns

Electron diffraction patterns were obtained from the TEM images to provide further analysis of the atomic crystal lattice structure within the MWNT branches. The electron beam is diffracted when passing through a lattice such that the path of the electrons is altered by specific angles so that beams from different points in the lattice can add to form sharp spots or lines on an image recorded beneath the sample.<sup>40,41</sup>

In SWNTs these spots and lines give indications towards the curvature of the SWNT, the chirality, the nanotube diameter and crystallinity. However, for MWNTs the data is more difficult to interpret as the multiple layers within the tube all contribute to the same pattern, and the properties between the layers are often different. However, it has been shown that the crystallinity of the MWNTs may still be found from the sharpness of the spots in an electron diffraction pattern. Therefore in this thesis, electron diffraction is critical to investigate whether or not the crystallinity of the MWNTs is preserved during the arc assembly process.

Three sites were chosen towards the end of a 110 nm diameter MWNT, where the electric field is the strongest and thus damage from the plasma is most likely to have occurred. The presence of any possible damage is of interest as this will indicate that the nanotube is participating in the arc assembly process and that the plasma is sufficiently strong to break the  $sp^2$  bonds. The onion shown in Figure 4.23 A & C on the end of the nanotube could be a defect caused by the growth of the nanotube, or could be explained as a result of arcing to that point, as is observed from CNT growth in arc synthesis.<sup>42,43</sup>

At the top of the onion Figure 4.23 A & B both by the TEM image and the electron diffraction pattern amorphous material may be observed surrounding the visible lines of the carbon lattice, and few distinct spots are visible which may be as a result of this, if they are

otherwise too diffuse caused by a lack of crystallinity or the multi-directional nature of the many overlapping layers.

Figure 4.23 C & D show a highly ordered carbon lattice entering the onion region, and the diffraction pattern gives a line of distinct peaks, suggesting that a large degree of crystallinity has been preserved, and/or is visible through the other layers of the MWNT.

Figure 4.23 E & F show a straight lattice, with only amorphous carbon/OMCTS residue around the outside. The diffraction pattern reflects this with a clear line of distinct spots, and no smearing effect that is visible the rings in Figure 4.23 D.

The possible implications from these results are:

- *This particular CNT was not exposed to arcing.* This explains the strong preservation of crystallinity – yet given the CNT bonded with other local CNTs, so the ends of the nanotubes. The bonding between the nanotubes may not be related to the arcing occurring (which contradicts the general observations of the removability of the thread from the dispersion.) However, it at least suggests that the nanotube is capable of withstanding nearby arcing, even if the nanotube itself does not participate in the discharge.
- *The nanotube was exposed to arcing, but was not damaged by it.* This has been observed in cases such as Bower et al where nanotubes can form part of field emitters in vacuum environment<sup>44</sup>, and hence may contribute to a plasma in a liquid. However if this is the case, it would not allow for any adhesion to form from the nanotube at this point.



- The nanotube was exposed to the arcing and the crystalline adhesion was caused by it. This would be the most encouraging interpretation for the applicability of Arc Assembly as this would allow for direct crystalline bonds between nanotubes.

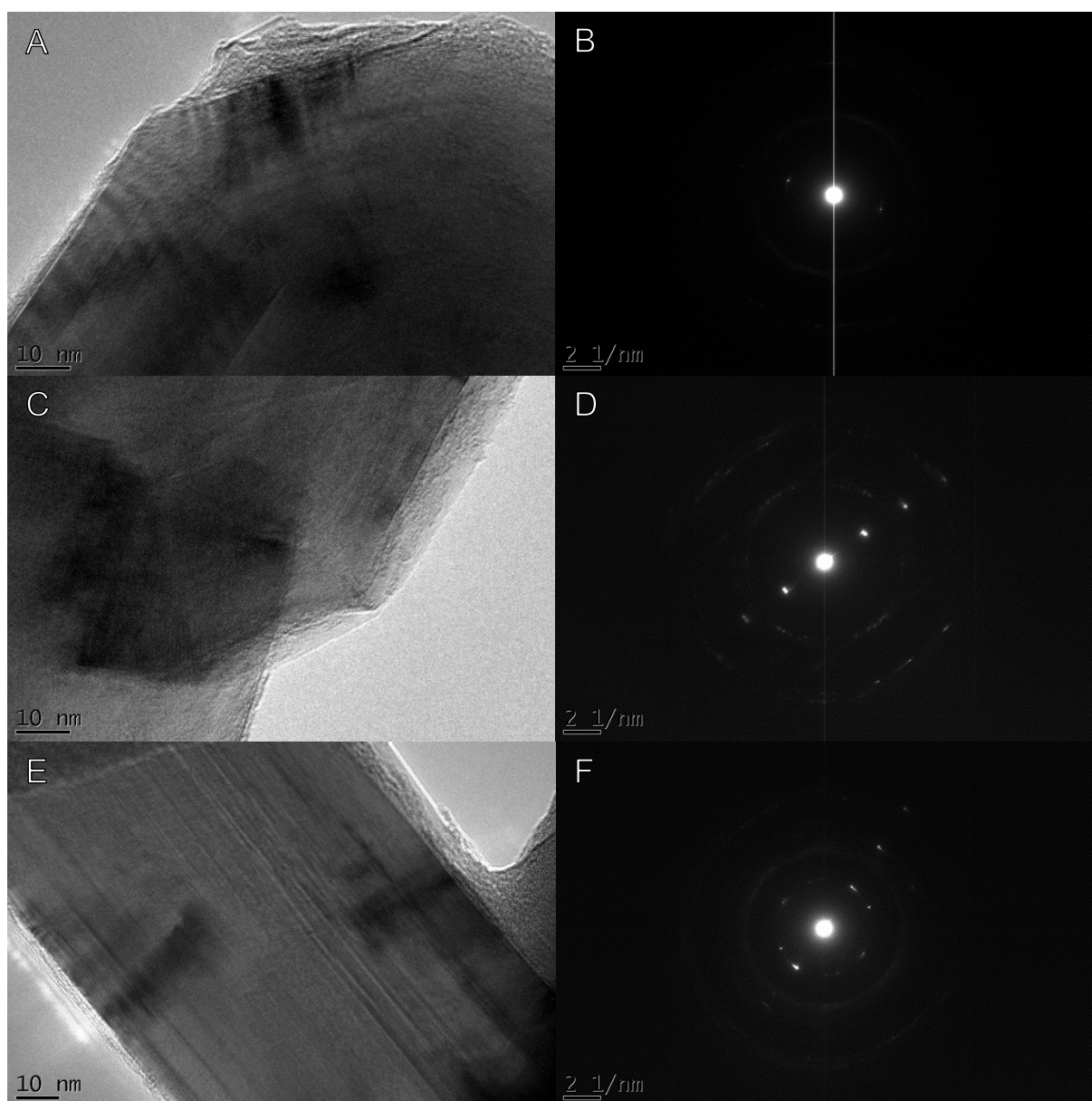


*Figure 4.23.* A Top of onion at end of nanotube B diffraction pattern of site on A C) Bottom of onion at end of nanotube. D) Diffraction pattern of site on C. E) MWNT beneath the aforementioned onion. F) Diffraction pattern of site on E.

Another three sites were chosen on a branch between 2 nanotubes from arc assembled triglyceride dispersion. This branch could be caused during growth, but is of interest as it may have instead been formed during the arc assembly process. The sites were picked in the centre of the merging of the 2 lattices from  $\sim 90^\circ$  degrees and two sites nearby to this shown in Figure 4.24 D.

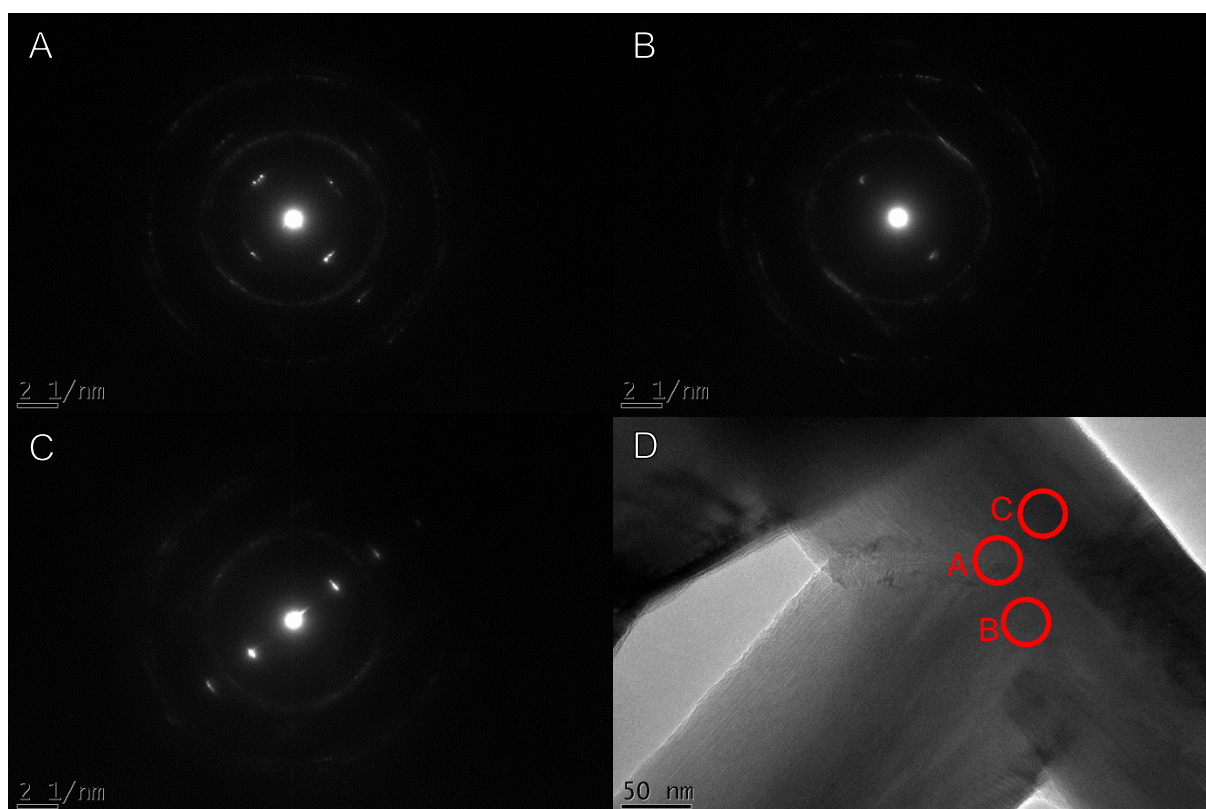


Figure 4.24. A,B,C are electron diffraction patterns from sites annotated on D.

Although the point of connection of the branch in Figure 4.24 D looks as if the connecting structure may be amorphous, the diffraction pattern shows only slightly smeared, but distinct spots from 2 directions suggesting that the 2 crystal lattices have bonded whilst preserving crystallinity. It may be possible that the outer most layers are not entirely crystalline but a diffraction pattern is still formed from internal crystalline layers. Furthermore Figure 4.24

B,C show sharp spots suggesting that crystallinity has also been preserved around the joint. This is also apparent in the TEM image where the lines of the carbon lattice are visible.

In a similar manner to the interpretation of Figure 4.18 D, if this branch was formed via arc assembly it would indicate that the process can create crystalline links between nanotubes, however it is possible – and has been observed with control samples, that these branches could be formed from the original synthesis of the nanotubes themselves.<sup>45</sup>



## 4.10 Raman Spectroscopy

Raman spectroscopy is an analytical technique for measuring the vibrational states of chemical bonds. When photons from a laser of a specific wavelength interact with molecular vibrations of the sample, the photons may experience inelastic scattering as energy is lost, or in some cases gained from the chemical bond. This loss/gain in energy corresponds to a shift in wavelength which can be measured as a difference to the original wavelength of the incident photon. In this way information is gained on the nature of the chemical bonds within a compound – which is of particular use for assessing carbon nanotubes which can have many different forms. A sketch of this process is shown in Figure 4.25:

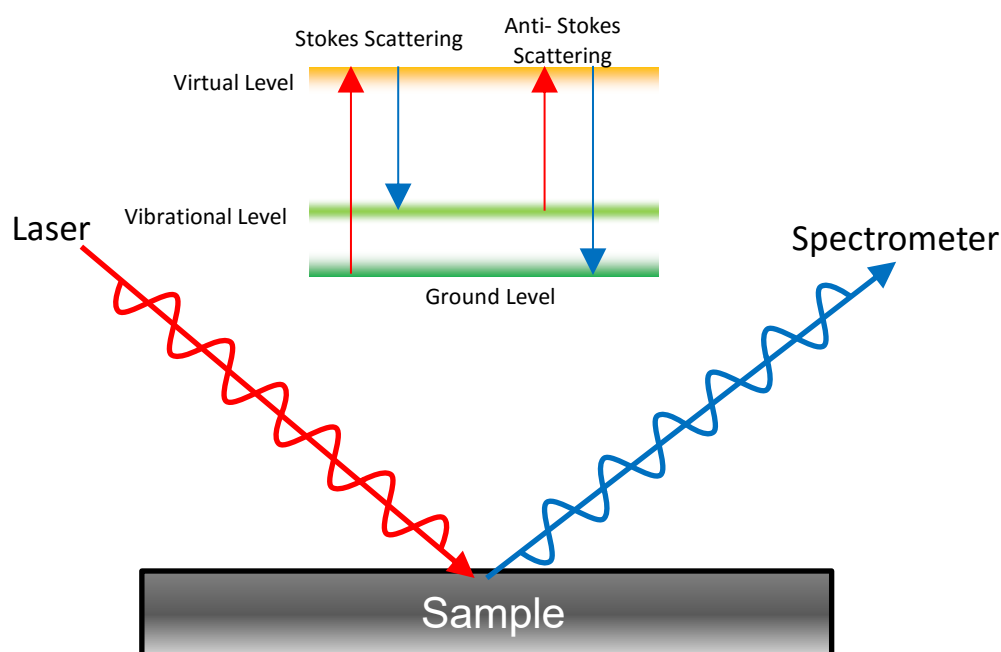


*Figure 4.25.* Sketch of basic mechanism for Raman scattering. With relevant energy transitions for Stokes and Anti-Stokes Scattering.

The possible loss and gain in energy is specifically attributed to Stokes and anti-Stokes scattering. The incoming photons can interact with the electrons of the molecule at the ground level or the vibrational level and raise the energy of the photon to the “virtual level”

(an unobservable quantum state) from which the photon is scattered inelastically such that the energy of the molecule is returned to either the ground or vibrational level. This can create a difference in energy on the molecule and thus a transfer of energy on the photon: Stokes refers to the loss of energy – an increase in wavelength; anti-Stokes refers to the gain of energy - a decrease in wavelength. It is these differences in wavelength (referred to as shifts) that are measured and assessed in Raman spectroscopy to determine the properties of the material.

The radial breathing mode ( $100\text{--}300\text{ cm}^{-1}$ ) is typically used to assess SWNTs however as the diameter of the tubes increases the tubes approximate to a graphene sheet, and is not included on the spectrum for MWNTs.<sup>46,47</sup> The spectrum for raw MWNTs may be seen below in Figure 4.26.

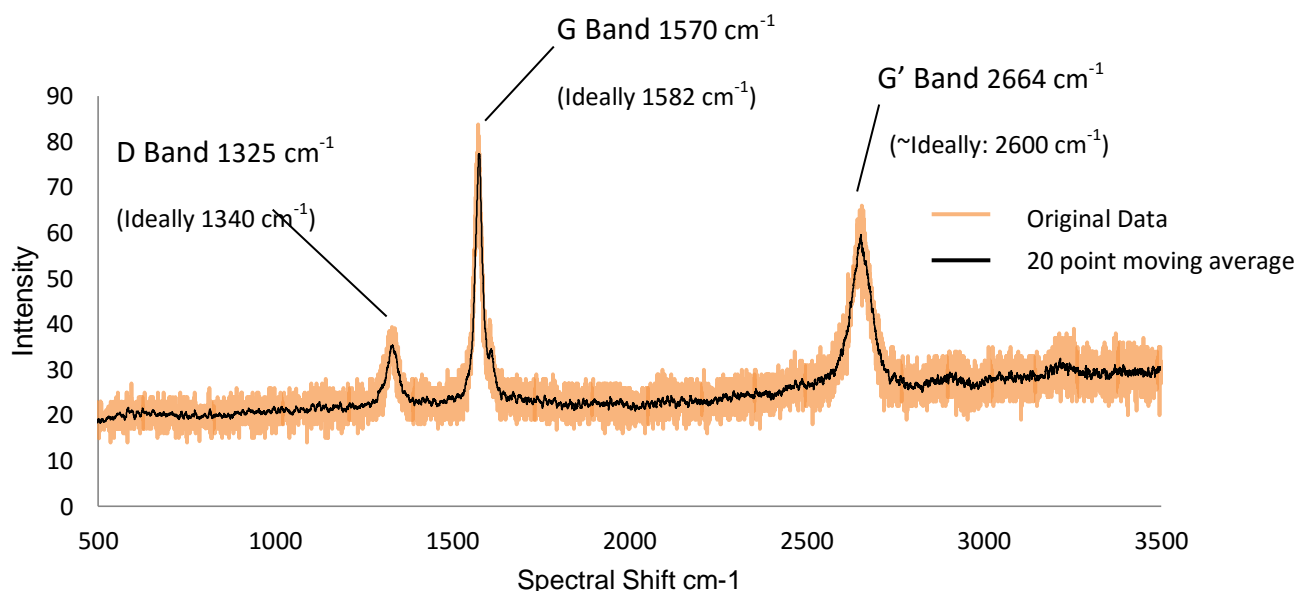


*Figure 4.26.* Raman Spectra of unprocessed MWNTs used for arc assembly.

The D-band at  $1340\text{ cm}^{-1}$  is associated to the out of plane vibrations, usually implying that defects within a graphitised structure which in-turn, implies the presence of  $\text{sp}^3$  bonded

carbon. For pure graphitic material, the in-plane vibrations of the G-band are at  $1582\text{ cm}^{-1}$ . However, there may be a number of peaks around this line. For SWNT, a G+ and a G- line may also be present at around  $1590\text{ cm}^{-1}$  and  $1570\text{ cm}^{-1}$ . However, for MWNTs, these are not always visible, if the innermost tube has a large diameter.

A G' band is a second order harmonic or 'overtone' (as twice the frequency dispersion) of the D-band, and has been shown as a way of assessing the interaction and number of multiple crystalline carbon as a single graphene sheet will produce a sharp peak at approximately  $2600\text{ cm}^{-1}$ , whilst graphite will create a higher shifted and dispersed peak due to the scattering of multiple layers adding together.<sup>48,49</sup> This Raman spectroscopy was carried out to give a further indication to the nature of any changes in the material properties of the CNTs, given previous SEM, EDX and TEM showed contrasting results of amorphous and crystalline bonding between the CNTs.

#### 4.10.1 Raman Spectrum of Continuous Arc Assembled Thread

The following results are typical of carbon. The original MWNT sample gave a very noisy response, which is thought to be due to the powdered form of the sample, leading to an uneven and porous surface to image on, i.e. not all regions would have been in focus, and diffraction could occur around edges as a result. A 20 point moving average was included with the graphs for clarity. The arc assembled thread was rinsed thoroughly in IPA to remove any nanotubes that may have remained on the surface after the process, and the reduction in noise from the original MWNT sample shows the surface was relatively smooth with few loose nanotubes. All the samples exhibit a shoulder on the G-band, which is often analysed using a deconvolution to show multiple contributing peaks from a combination of different bonding types affecting the G-Band. However, this technique requires a reasonable estimation of what those bonds are. Currently, as there is no established premise for estimating results from an arc assembly process, the deconvolution has been omitted.

A sample MWNT thread is shown in Figure 4.27 with the complete Raman spectra for 3 sites of interest selected along the thread's length. Site 1 is on the edge of the terminating end of the MWNT thread (similar to Figure 4.20). Site 2 is on the straight portion of the thread where the continuous arc assembly was most consistent. Site 3 is on the curved section of the thread, near the beginning of the arc assembly process, where the thread position moved during the process. These sites are revisited in Figures 4.28 for a more detailed look at the G-band and G'-band. The primary interest from the Raman data is how  $sp^2$  crystallinity is preserved throughout the arc assembly process.<sup>50,51</sup>

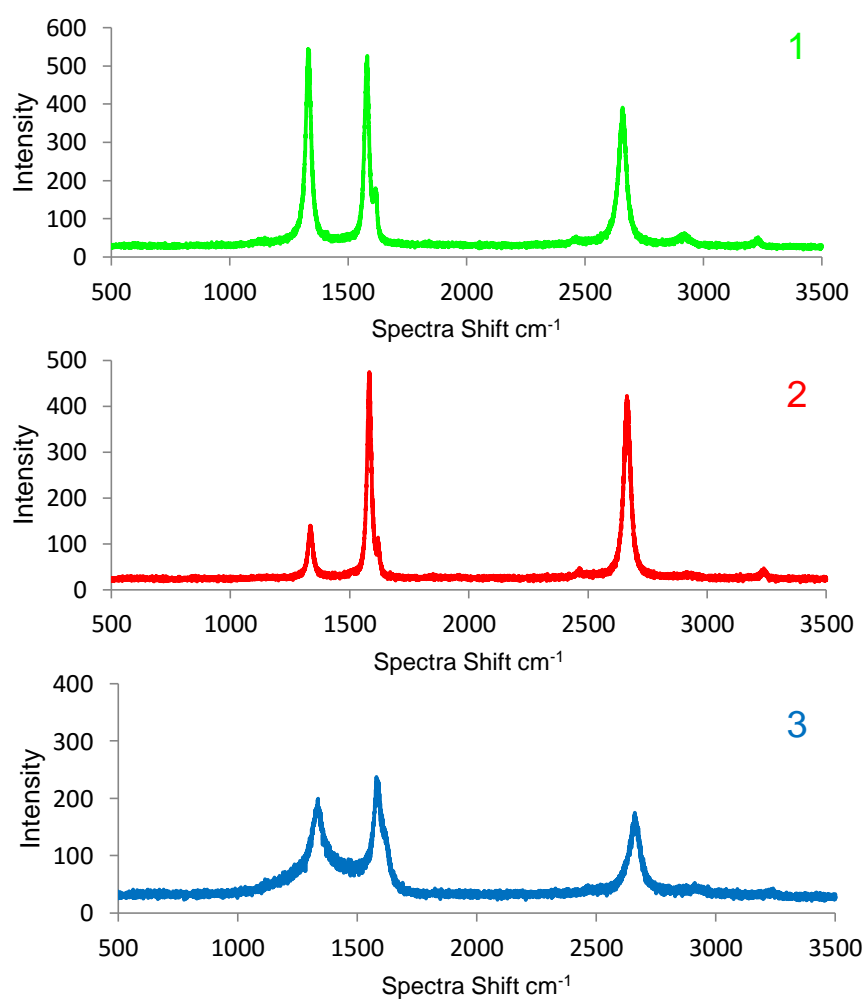
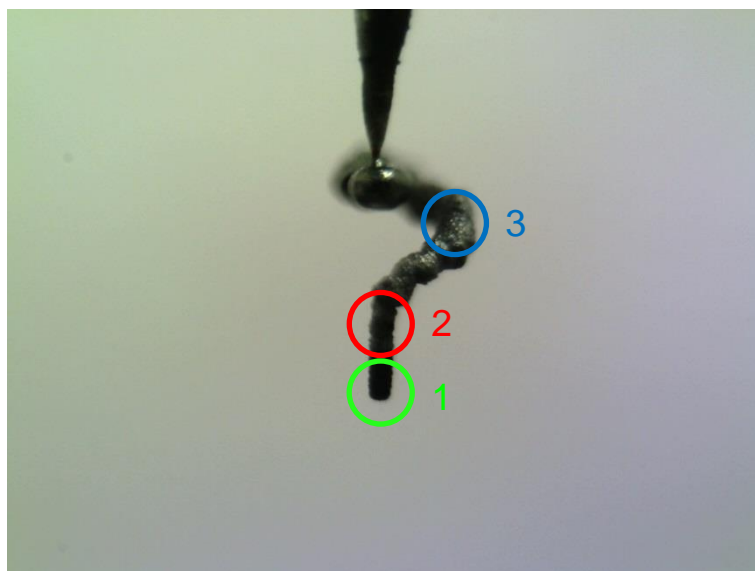
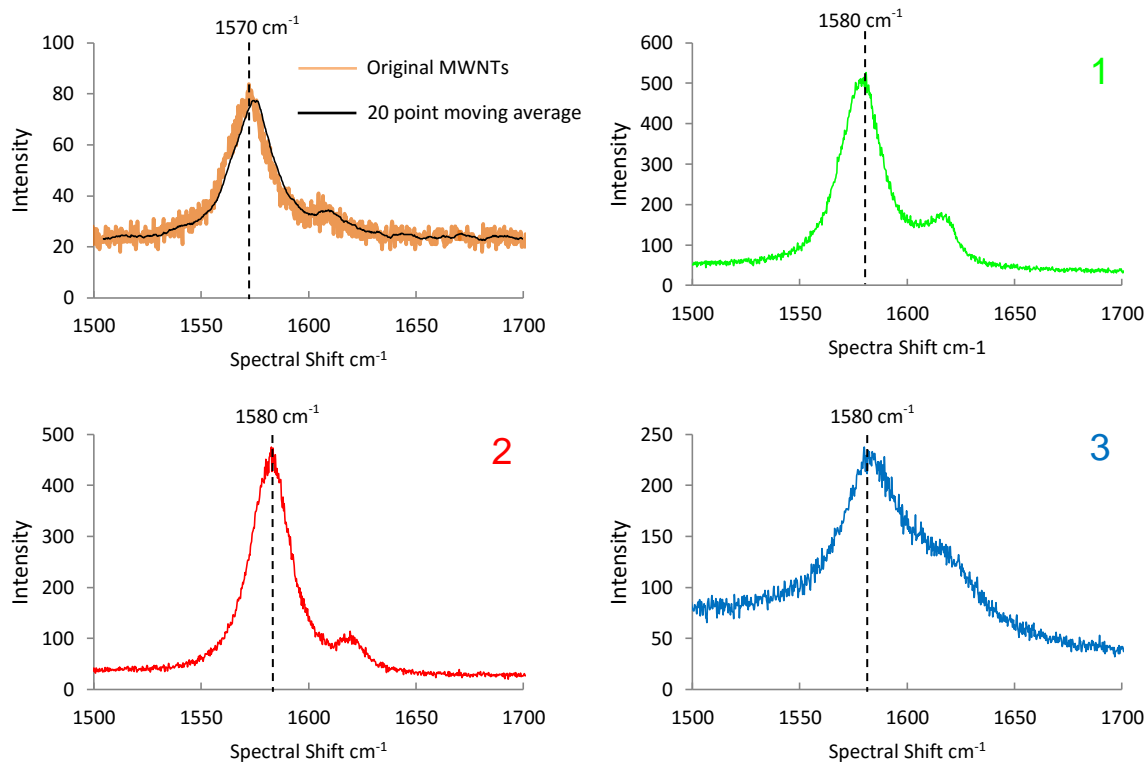


Figure 4.27. Complete Raman Spectra along the points of an Arc Assembled Thread

## 4.10.2 Raman Spectroscopy of G-Bands



## Raman Spectroscopy G` Bands

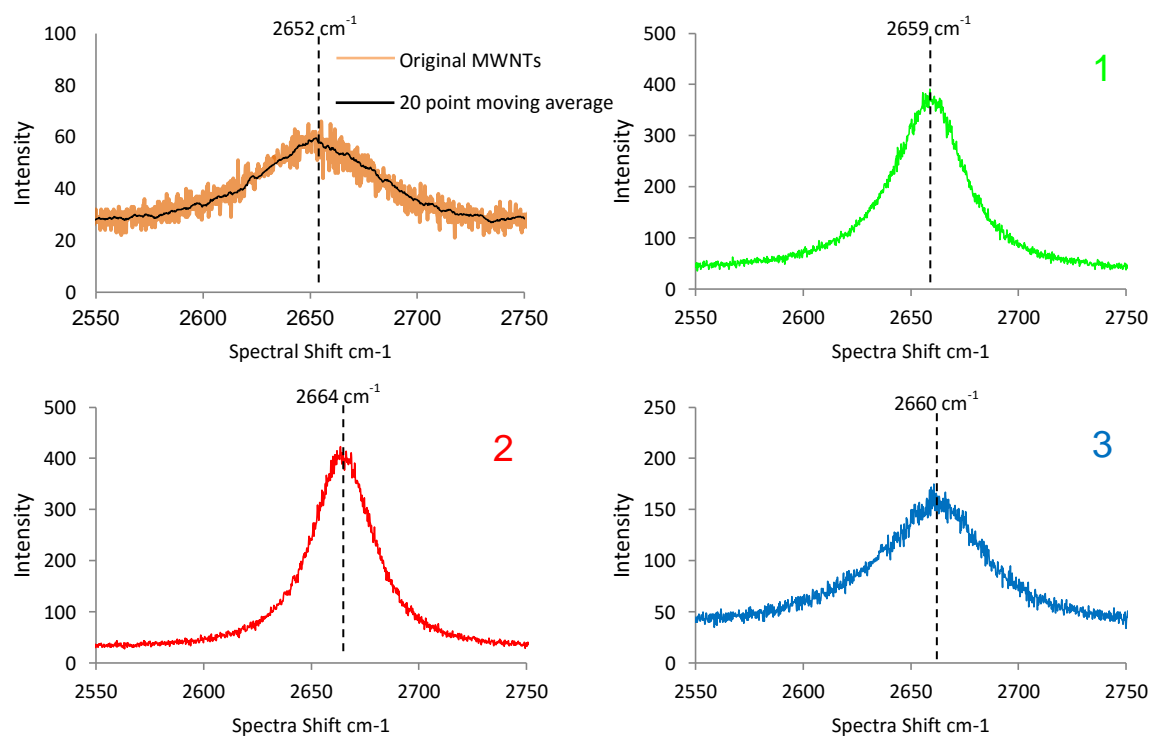


Figure 4.28. G Bands for Unprocessed MWNTs(a) and various locations along a MWNT thread as shown in Figure 4.26 (1,2,3)

### 4.10.3 Evaluation of Raman Spectroscopy Results

The intensity D-band indicates the number of defects whilst the G-band measures the number of  $sp^2$  bonds within a sample (area analysed). The ratio between these bands is an indication of quality of the CNTs with a higher ratio indicating greater graphitization. Therefore we can see in Table 4.1 that the original MWNTs have a high purity, (marketed as 99% pure.) However the arc assembly process has introduced defects, particularly towards the start and end of the process near the curve of site 1, and the end of the thread at site 3 where the Raman data suggests a high proportion of amorphous carbon. Interestingly, these sites coincide with the regions where the arc assembly process was not under control. This may be due to an overabundance of CNTs in the medium towards the start, and a depletion towards the end. In addition, it is possible the rate of removal for the tungsten probe did not perfectly match the rate of assembly.

Both of these parameters could also contribute to the stopping of the arc assembly process. Site 2 shows a remarkable result given the purity/quality of the CNTs appears to increase. This may be due to purification effect of amorphous carbon being burnt off via the plasma, (as pure  $sp^2$  crystalline structures are more stable within a plasma environment and baking of nanotubes is a common purification process.) However, it may also be due to the change in surface texture, allowing for less noisy measurements of the Raman data. Either way, a crucial point is nevertheless made: *for a region within the arc assembly process graphitisation is preserved.*

Sample	D-Band : G-Band Intensity
Original MWNTs	2.47
Site 1	0.97
Site 2	3.44
Site 3	1.19

*Table 4.1.* A Table of the ratio of D-Band to G-Band as a measure of Graphitization.

#### **G' Band** (or first order D-band)

The G' band presented as part of the raw MWNT sample is as expected with a shifted and dispersed peak due to the large number of crystalline layers within a 110 nm diameter carbon nanotube, and as observed via the TEM images. However, after a period of arc assembly the peak sharpens and shifts closer towards the  $2660\text{ cm}^{-1}$  which is often associated with graphene. SEM imaging supports this analysis by showing possible graphene exfoliation from the nanotubes is observed on a different thread, although fabricated under identical conditions in Figure 4.27 –which was split in half with tweezers.



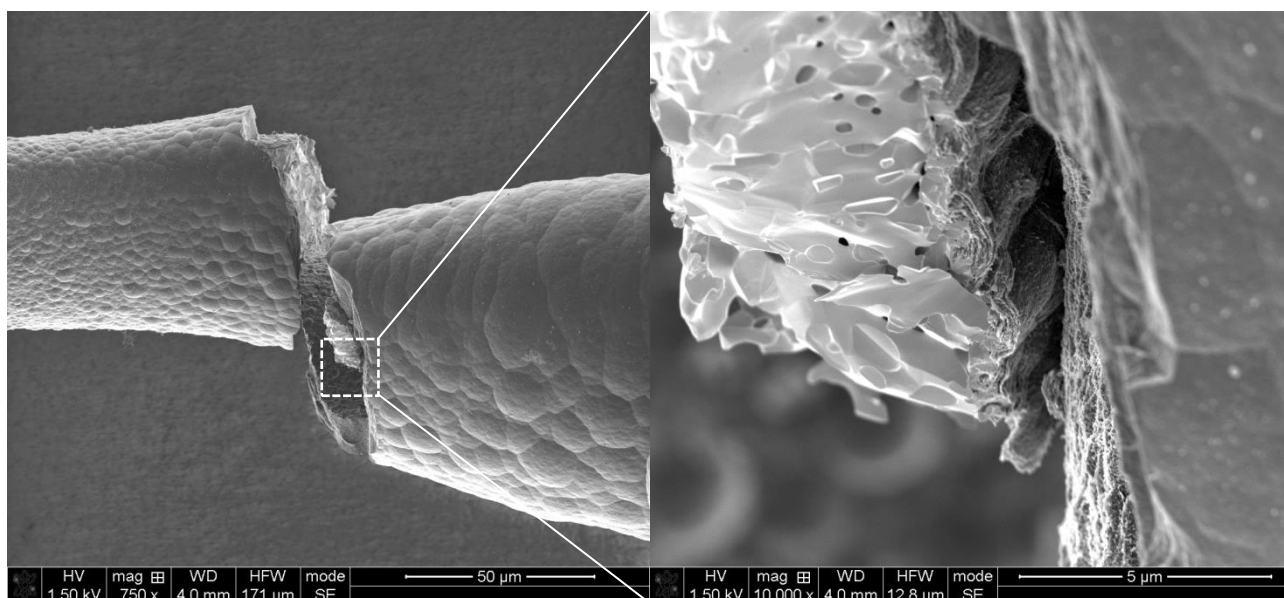


*Figure 4.29.* SEM image of broken segment of continuous Arc Assembled CNT thread

This also reinforces the analysis of the D-band G-Band ratios for site 2 as it would suggest the disordered components of the MWNTs are being removed – such as the caps leaving incomplete MWNTs which may “unroll” into sheets.

However it is unclear why this exfoliation is most apparent in the core of the thread, and in particular because the Raman data was taken at the surface of the thread, where the SEM images look most amorphous. It is possible that the threads are composed of multiple graphene fragments, as residue from damaged carbon nanotubes, and the core of the thread is undergoing a different mechanism of assembly due to the expected vortex within the dielectrophoretic plasma. There is already literature covering the topic of forming graphene fragments from carbon nanotubes via plasma discharge,<sup>52</sup> so this result may be similarly related.

## 4.11 Conclusion

This chapter sought to use electrosharpened tungsten probes as a tool to fabricate carbon nanotube threads, such that CNTs could be exploited on the macroscale. An entirely new method of applying dielectrophoresis with an arc discharge plasma was created called Arc Assembly and incrementally developed, guided by the analysis provided by SEM, EDX, TEM Raman spectra and COMSOL simulations. This novel process demonstrated that it had the capability of altering the chemical bonds of the CNTs whilst simultaneously joining them together. This is a key demand of modern research for exploiting the nanoscale properties of CNTs for larger applications. So far, this process has been able to fabricate threads of up to 5 mm in length.

This chapter showed that dielectrophoresis can be combined with voltages beyond the breakdown strength of the fluid medium to allow arc discharges to occur between dipole chains - this is the core principle behind Arc Assembly. Intermittent and continuous modes were established as variations on this, depending on the rate of separation between electrodes and overall power supplied to the system. Fluidic effects within the dielectrophoretic system were observed experimentally in the movement of CNTs and the overall electric fluid over a droplet of CNT mixture was modelled using COMSOL. In addition, the models showed how the dielectrophoretic effect would be reduced with increasing probe tip radii, as well as the change in field strength with electrode separation.

SEM analysis showed a high density of CNT branching and connections within Arc Assembled threads, and suggested that different types of branching were present due to the textures visible. In addition to branching, Lichtenberg figures, evidence for a fluidic vortex from dielectrophoretic forces and exfoliation of CNTs were also observed.

EDX data confirmed that the fluid medium would also adhere to the CNT threads to some degree with OMCTS polymer being used to show silicon within the threads.

TEM images with electron diffraction patterns were analysed showing indications that CNT crystallinity was at least partially conserved within the branches of Arc Assembly. However, amorphous carbon was also observed throughout the results. Given the fragile nature of the threads it is likely that either there are insufficient CNT branches or it is due to amorphous carbon forming during the process.

Raman analysis was conducted on a continuous arc assembled thread. This also revealed that some degree of CNT graphitization was preserved within the threads as the D-band to G-band ratios remained high relative to the raw CNTs. However the data also indicated large differences between sites at different stages of the Arc Assembly process. Both at the start and the end of the process indicated a growth of amorphous carbon, whilst the main withdrawal of the thread (when the rate of electrode separation was most constant) had comparable Raman spectra to the raw CNTs.

## 4.12 References

- [1] K. Jiang, Q. Li, and S. Fan, “Nanotechnology: Spinning continuous carbon nanotube yarns,” *Nature*, vol. 419, no. 6909, pp. 801–801, 2002.
- [2] M. Zhang, “Multifunctional Carbon Nanotube Yarns by Downsizing an Ancient Technology,” *Science*, vol. 306, no. 5700, pp. 1358–1361, Nov. 2004.
- [3] X. Zhang, K. Jiang, C. Feng, P. Liu, L. Zhang, J. Kong, T. Zhang, Q. Li, and S. Fan, “Spinning and Processing Continuous Yarns from 4-Inch Wafer Scale Super-Aligned Carbon Nanotube Arrays,” *Adv. Mater.*, vol. 18, no. 12, pp. 1505–1510, Jun. 2006.
- [4] N. Behabtu, C. C. Young, D. E. Tsentalovich, O. Kleinerman, X. Wang, A. W. K. Ma, E. A. Bengio, R. F. ter Waarbeek, J. J. de Jong, R. E. Hoogerwerf, S. B. Fairchild, J. B. Ferguson, B. Maruyama, J. Kono, Y. Talmon, Y. Cohen, M. J. Otto, and M. Pasquali, “Strong, Light, Multifunctional Fibers of Carbon Nanotubes with Ultrahigh Conductivity,” *Science*, vol. 339, no. 6116, pp. 182–186, Jan. 2013.
- [5] F. A. Hill, T. F. Havel, A. J. Hart, and C. Livermore, ‘Enhancing the Tensile Properties of Continuous Millimeter-Scale Carbon Nanotube Fibers by Densification’, *ACS Applied Materials & Interfaces*, vol. 5, no. 15, pp. 7198–7207, Aug. 2013.
- [6] F. Li, H. M. Cheng, S. Bai, G. Su, and M. S. Dresselhaus, ‘Tensile strength of single-walled carbon nanotubes directly measured from their macroscopic ropes’, *Applied Physics Letters*, vol. 77, no. 20, p. 3161, 2000.

- [7] Y. Liu, J.-H. Chung, W. K. Liu, and R. S. Ruoff, 'Dielectrophoretic Assembly of Nanowires', *The Journal of Physical Chemistry B*, vol. 110, no. 29, pp. 14098–14106, Jul. 2006.
- [8] V. M. L. L. V. Radushkevich, 'About the structure of carbon formed by thermal decomposition of carbon monoxide on iron substrate', *Zurn. Fisic. Chim.*, vol. 26, pp. 88–95, 1952 (in Russian).
- [9] S. Iijima, 'Helical microtubules of graphitic carbon', *Nature*, vol. 354, no. 6348, pp. 56–58, Nov. 1991.
- [10] Peter J. F. Harris, *Carbon Nanotube Science: Synthesis, Properties and Applications*. Cambridge University Press, 2009, 9780521535854.
- [11] Z. H. K. M Husain, 'Carbon Nanotube and its possible applications', *Indian Journal of Engineering & Material Sciences*, vol. 12, pp. 529–551, 2005.
- [12] D. Zhou, E. V. Anoshkina, L. Chow, and G. Chai, 'Synthesis of carbon nanotubes by electrochemical deposition at room temperature', *Carbon*, vol. 44, no. 5, pp. 1013–1016, Apr. 2006.
- [13] M. F. L. De Volder, S. H. Tawfick, R. H. Baughman, and A. J. Hart, 'Carbon Nanotubes: Present and Future Commercial Applications', *Science*, vol. 339, no. 6119, pp. 535–539, Jan. 2013.
- [14] Q. Zeng, Z. Li, and Y. Zhou, 'Synthesis and application of carbon nanotubes', *Journal of Natural Gas Chemistry*, vol. 15, no. 3, pp. 235–246, 2006.

- [15] N. Nishimiya, K. Ishigaki, H. Takikawa, M. Ikeda, Y. Hibi, T. Sakakibara, A. Matsumoto, and K. Tsutsumi, 'Hydrogen sorption by single-walled carbon nanotubes prepared by a torch arc method', *Journal of alloys and compounds*, vol. 339, no. 1, pp. 275–282, 2002.
- [16] J. Zhang and C. Pan, 'Magnetic-field-controlled Alignment of Carbon Nanotubes from Flames and Its Growth Mechanism', *Journal of Physical Chemistry C*, vol. 112, no. 35, pp. 13470–13474, Sep. 2008.
- [17] L. Alvarez, T. Guillard, G. Olalde, B. Rivoire, J. F. Robert, P. Bernier, G. Flamant, and D. Laplaze, 'Large scale solar production of fullerenes and carbon nanotubes', *Synthetic metals*, vol. 103, no. 1, pp. 2476–2477, 1999.
- [18] D. Laplaze, P. Bernier, W. K. Maser, G. Flamant, T. Guillard, and A. Loiseau, 'Carbon nanotubes: the solar approach', *Carbon*, vol. 36, no. 5, pp. 685–688, 1998.
- [19] S. Iijima and T. Ichihashi, 'Single-shell carbon nanotubes of 1-nm diameter', *Nature*, vol. 363, no. 6430, pp. 603–605, Jun. 1993.
- [20] A. Maiti, C. J. Brabec, C. M. Roland, and J. Bernholc, 'Growth Energetics of Carbon Nanotubes', *Phys. Rev. Lett.*, vol. 73, no. 18, pp. 2468–2471, Oct. 1994. ARC
- [21] P. J. F. Harris, 'Solid state growth mechanisms for carbon nanotubes', *Carbon*, vol. 45, no. 2, pp. 229–239, Feb. 2007.
- [22] H. H. Kim and H. J. Kim, 'The preparation of carbon nanotubes by dc arc discharge using a carbon cathode coated with catalyst', *Materials Science and Engineering: B*, vol. 130, no. 1–3, pp. 73–80, Jun. 2006.

- [23] A. K. Zettl and M. L. Cohen, Method for making nanotubes and nanoparticles. Google Patents, 2000. US6063243 A
- [24] Y. Kim, E. Nishikawa, and T. Kioka, ‘An underwater arc discharge method of CNT production using carbon electrode physical vibration’, J. Plasma. Fusion Res, vol. 8, 2009.
- [25] S.-D. Wang, M.-H. Chang, K. M.-D. Lan, C.-C. Wu, J.-J. Cheng, and H.-K. Chang, ‘Synthesis of carbon nanotubes by arc discharge in sodium chloride solution’, Carbon, vol. 43, no. 8, pp. 1792–1795, Jul. 2005.
- [26] J.-C. Charlier, A. De Vita, X. Blase, and R. Car, ‘Microscopic Growth Mechanisms for Carbon Nanotubes’, Science, vol. 275, no. 5300, pp. 647–649, Jan. 1997.
- [27] E. G. Gamaly and T. W. Ebbesen, ‘Mechanism of carbon nanotube formation in the arc discharge’, Physical Review B, vol. 52, no. 3, pp. 2083–2089, Jul. 1995.
- [28] O. A. Louchev, ‘Transport-kinetical phenomena in nanotube growth’, Journal of Crystal Growth, vol. 237–239, pp. 65–69, Apr. 2002.
- [29] K. K. Kia and F. Bonabi, ‘Electric field induced needle-pulsed arc discharge carbon nanotube production apparatus: Circuitry and mechanical design’, Review of Scientific Instruments, vol. 83, no. 12, p. 123907, 2012.
- [30] H. A. Pohl, “The motion and precipitation of suspensoids in divergent electric fields,” J. Appl. Phys., vol. 22, no. 7, pp. 869–871, 1951.

- [31] H. A. Pohl, K. Kaler, and K. Pollock, "The continuous positive and negative dielectrophoresis of microorganisms," *J. Biol. Phys.*, vol. 9, no. 2, pp. 67–86, 1981.
- [32] H. Morgan and N. G. Green, "Dielectrophoretic manipulation of rod-shaped viral particles," *J. Electrostat.*, vol. 42, no. 3, pp. 279–293, 1997.
- [33] M. Dimaki and P. Bøggild, "Dielectrophoresis of carbon nanotubes using microelectrodes: a numerical study," *Nanotechnology*, vol. 15, no. 8, pp. 1095–1102, Aug. 2004.
- [34] R. Pethig, "Dielectrophoresis: Status of the theory, technology, and applications," *Biomechanics*, vol. 4, no. 2, p. 022811, 2010.
- [35] Thomas B. Jones, *Electromechanics of Particles*. Cambridge University Press, 1995.
- [36] T. B. Jones and G. W. Bliss, 'Bubble dielectrophoresis', *Journal of applied physics*, vol. 48, no. 4, pp. 1412–1417, 1977.
- [37] T. B. Jones, 'Dielectrophoretic force calculation', *Journal of Electrostatics*, vol. 6, no. 1, pp. 69–82, 1979.
- [38] T. B. Jones, 'Dielectrophoretic force in axisymmetric fields', *Journal of electrostatics*, vol. 18, no. 1, pp. 55–62, 1986.
- [39] T. B. Jones, 'An electromechanical interpretation of electrowetting', *Journal of Micromechanics and Microengineering*, vol. 15, no. 6, pp. 1184–1187, Jun. 2005.



- [40] A. Szabó, C. Perri, A. Csató, G. Giordano, D. Vuono, and J. B. Nagy, ‘Synthesis Methods of Carbon Nanotubes and Related Materials’, *Materials*, vol. 3, no. 5, pp. 3092–3140, May 2010.
- [41] S. Boncel, R. M. Sundaram, A. H. Windle, and K. K. K. Koziol, “Enhancement of the Mechanical Properties of Directly Spun CNT Fibers by Chemical Treatment,” *ACS Nano*, vol. 5, no. 12, pp. 9339–9344, Dec. 2011.
- [42] F. A. Hill, T. F. Havel, A. J. Hart, and C. Livermore, “Enhancing the Tensile Properties of Continuous Millimeter-Scale Carbon Nanotube Fibers by Densification,” *ACS Appl. Mater. Interfaces*, vol. 5, no. 15, pp. 7198–7207, Aug. 2013.
- [43] C. Zhu, C. Cheng, Y. H. He, L. Wang, T. L. Wong, K. K. Fung, and N. Wang, “A self-entanglement mechanism for continuous pulling of carbon nanotube yarns,” *Carbon*, vol. 49, no. 15, pp. 4996–5001, Dec. 2011.
- [44] C. Bower, W. Zhu, D. Shalom, D. Lopez, L. H. Chen, P. L. Gammel, and S. Jin, ‘On-chip vacuum microtriode using carbon nanotube field emitters’, *Applied Physics Letters*, vol. 80, no. 20, pp. 3820–3822, 2002.
- [45] Shengyong Xu, Yong Yang, Sishen Xie, and Lianmao Peng, ‘Current sustainability and electromigration of Pd, Sc and Y thin-films as potential interconnects’, *Nano-Micro Letters*, vol. 2, no. 3, pp. 184–189, May 2010.
- [46] M. S. Dresselhaus, G. Dresselhaus, R. Saito, and A. Jorio, ‘Raman spectroscopy of carbon nanotubes’, *Physics Reports*, vol. 409, no. 2, pp. 47–99, Mar. 2005.

- [47] A. M. Rao, E. Richter, S. Bandow, B. Chase, P. C. Eklund, K. A. Williams, S. Fang, K. R. Subbaswamy, M. Menon, A. Thess, and others, ‘Diameter-selective Raman scattering from vibrational modes in carbon nanotubes’, *Science*, vol. 275, no. 5297, pp. 187–191, 1997.
- [48] S. D. M. Brown, P. Corio, A. Marucci, M. A. Pimenta, M. S. Dresselhaus, and G. Dresselhaus, ‘Second-order resonant Raman spectra of single-walled carbon nanotubes’, *Phys. Rev. B*, vol. 61, no. 11, pp. 7734–7742, Mar. 2000.
- [49] V. W. Brar, G. G. Samsonidze, M. S. Dresselhaus, G. Dresselhaus, R. Saito, A. K. Swan, M. S. Ünlü, B. B. Goldberg, A. G. Souza Filho, and A. Jorio, ‘Second-order harmonic and combination modes in graphite, single-wall carbon nanotube bundles, and isolated single-wall carbon nanotubes’, *Phys. Rev. B*, vol. 66, no. 15, p. 155418, Oct. 2002.
- [50] M. Souza, A. Jorio, C. Fantini, B. R. A. Neves, M. A. Pimenta, R. Saito, A. Ismach, E. Joselevich, V. W. Brar, G. G. Samsonidze, G. Dresselhaus, and M. S. Dresselhaus, ‘Single- and double-resonance Raman  $G$ -band processes in carbon nanotubes’, *Phys. Rev. B*, vol. 69, no. 24, p. 241403, Jun. 2004.
- [51] X. Zhao, Y. Ando, L.-C. Qin, H. Kataura, Y. Maniwa, and R. Saito, ‘Radial breathing modes of multiwalled carbon nanotubes’, *Chemical Physics Letters*, vol. 361, no. 1–2, pp. 169–174, Jul. 2002.
- [52] L. Jiao, L. Zhang, X. Wang, G. Diankov, and H. Dai, ‘Narrow graphene nanoribbons from carbon nanotubes’, *Nature*, vol. 458, no. 7240, pp. 877–880, Apr. 2009.

# Chapter 5

Conclusion

## Chapter 5: Conclusion

This thesis has delivered a new approach: *Tungstate Sharpening* for fabricating tungsten probes to controllable lengths with tip radii of the order of 10 nm. Furthermore, *Enhancements to Electrosharpening* scaled probe fabrication using a novel magnetohydrodynamic etching effect – which has also expanded the work to include razor blades. In addition, these tungsten probes were used to facilitate the development of Carbon Nanotube (CNT) threads – which were made using a novel dielectrophoretic ‘*Arc Assembly*’ process – up to 5 mm in length.

### 5.1 Electrosharpening Conclusion

Before the start of the PhD tungsten probes were fabricated on variations of an archaic method that had been used for at least sixty years. The drop-off method is unreliable and time consuming, yet was still essential for modern research. It is often deemed an ‘art’ in a field where by 2015 it should be a ‘science’. By the end of this PhD an alternative method had been invented and demonstrated to offer a process that could be rapidly automated and scaled, whilst maintaining the instrumental qualities that modern research demands.

The contributions of this body of research and contribution to the field of engineering may be summarised thus:

1. Tungstate Sharpening as a new method for fabricating tungsten probes, demonstrating reliable fabrication of tip radii down to 20 nm confirmed via SEM imaging and lengths between 0.5 – 5 mm.
2. The probes can successfully perform STM operations: the most common application, which further reinforces the desirable sharp nature of the probe tips.
3. A complete LabVIEW program was developed that now gives users the ability to fabricate probes to desired parameters without necessarily needing to even understand the underlying principles outlined in this thesis.
4. Tungstate Sharpening can be scaled to etch five probes simultaneously in a batch process – something that was impossible for the drop-off method. This meets the demands of the probe's consumable nature.
5. The batch process was modelled within a SolidWorks flow simulation to assess likely causes for perturbations within the etching fluid's motion. It found differences in tungstate density distribution and turbulence depending on the spacing between probes. This gave improvements for further experiments as well as showing that relatively simple flow simulations may be sufficient for modelling elements within complex electrochemical phenomena.
6. The process could be improved via the application of magnetohydrodynamics, which allows for new probe geometries and more reliable simultaneous etches. Furthermore, this demonstrates that some of the processes' key parameters can be modified without compromising the overall sharpening effect, suggesting there are opportunities for further research in this field.
7. A new application of the process for etching stainless steel razor blades is already being considered with preliminary results offering a competitive and versatile alternative to modern manufacturing techniques.

## 5.2 Future Work on Tungstate Sharpening and Enhancements to Electrosharpening

Although the tungstate sharpening process has already yielded many useful results, many questions remain such as:

*Can the process be further optimized?* This thesis explored tungstate sharpening and its derivatives using the parameters most commonly used within the drop-off method – this was so any results would be directly comparable to drop-of method. Although many shortcomings of the drop-of method were addressed, it become apparent that many of the critical parameters such as the concentration, voltage, electrolyte etc.... may be adjusted to improve further the tungstate sharpening method proposed to give a competitive edge over any existing technique.

*Can the scalability of the process continue for use in industrial applications?* The batch processing method proposed clearly demonstrates the ability to produce several probes simultaneously. However, ensuring uniform lengths among the probes etched was seen as the only obstacle. Coupling magnetic sharpening to the process reduced this effect significant for five probes. However, it is not clear if scaling up the technique will give consistency for 100s or 1000s of probes etched simultaneously.

*Can the probes be modified even further?* It has already been shown that the length and shapes of the probes can be altered through control of etching duration and magnetic fields. However, other preliminary experiments have shown uniform oxide coatings may be applied and it is not clear if more complex magnetic fields could give the probes a greater range of profiles.

## 5.3 Arc Assembly Conclusion

A new process called Arc Assembly was developed using the electrosharpened tungsten probes. Although the research was unable to create a thread that matched the nanoscale mechanical characteristics of carbon nanotubes the process was able to assemble the nanotubes into a thread, and show that those nanotubes had undergone significant chemical change beyond what other methods have been able to achieve, whilst still retaining elements of graphitization within the thread.

Analysis of various thread samples was performed via SEM imaging, EDX, TEM and Raman Spectroscopy. The analysis was performed over the course of the developing experiments in each case, to improve and guide the experiments, rather than characterise the material produced. The SEM results gave clear images of CNTs adhered to each other throughout the work, suggesting that the Arc Assembly process was successful in altering the chemical nature of the CNTs, rather than forming bundles as in conventional techniques. The EDX data indicated that the role of the fluid medium may be influencing this adhesion as silicon was found within the threads from OMCTS polymer used as a dielectric medium. TEM analysis showed sites of highly ordered crystalline branching in addition to amorphous regions amongst the CNTs. Whilst Raman data indicated that the preservation of sp<sup>2</sup> bonds within the CNT material was closely related to the removal process of the thread as it was being formed.

Given the novel nature of this research, the rate at which it is improving since its inception, and that this first time dielectrophoresis has been shown to interact with a plasma, although a complete theoretical model is beyond the scope of this thesis, the key parameters of voltage, field strength, frequency and medium have all been shown to have a strong influence over the

outcome of the process. The fact that this is now possible is knowledge which may open avenues for researchers who previously had thought such interactions impossible.

## 5.4 Future Work on Arc Assembly

Although carbon nanotubes exhibit remarkable properties on the nanoscale they have not yet seen widespread use in any large-scale application. If their nanoscale properties could be exploited it would revolutionize the use of nanomaterials in mechanical, electronic and thermal applications – as well as possibly developing into entirely new ranges of applications.

Many attempts have been made to align carbon nanotubes together. However, they remain unsuccessful as none of the attempts to extend the  $sp^2$  crystallinity between nanotubes, which determines their desirable nanoscale characteristics.

This work has shown that Arc Assembly may be a viable route to overcome this problem. It is now possible to simultaneously align and perform an arc discharge between nanotubes, such that the nanotubes adhere together. This is a completely new approach to developing macro-scale carbon nanotube material, and based on well-established literature, there are many parameters which may be altered, particularly in the nature of the plasma to form a greater proportion of  $sp^2$  bonds within this material. Currently the threads are too weak to measure mechanically, however the analysis presented here shows, and the *progression* of the experimentation indicates that the reasoning behind this approach is sound and may lead towards the successful assembly of ultra-strong CNT threads. Ultimately it is hoped that some key goals may be accomplished using this technique and questions answered such as:



*What is the nature of the combined dielectrophoretic arc discharge?* The current theory for dielectrophoresis outlined in Chapter 4.2 does not account for the phenomenon occurring within plasma. Although intermittent Arc assembly may approximately follow this theory, the continuous process does not. The plasma introduces a medium that will not behave as a dielectric, yet the same fluidic motion is observed as with conventional dielectrophoresis. The answer to this question may inform the future work outlined here – in addition to providing a new method of control over any arc discharge process.

*What is the role of the dielectrophoretic medium?* Many dielectric fluids were used during the progression of the experiments. Although they have a large influence on the dielectrophoretic effect they also affect the breakdown voltage between the CNTs, and the nature of the plasma that adheres them together. Currently Oleic Acid (with trace fatty acid impurities), polydimethylsiloxane, octomethylcyclotetrasiloxane and perfluorocarbon fluids have been used successfully yielding different results over the course of the SEM, TEM EDX and Raman analysis. Despite this no pattern has emerged to give insight into their role and leaves the question to what other mediums may be used instead?

*Utilising different nanomaterials:* Multi-walled nanotubes were extensively used throughout this thesis, due to the difficulty in successfully maintaining a dispersion of single-walled nanotubes (SWNTs) throughout the Arc Assembly process. However, this opens up the possibility that SWNTs may produce CNT threads provided this technical difficulty can be overcome. In addition, given the variety of electronic properties CNTs can exhibit, and the wide range of frequencies Arc Assembly has been shown to work under, it is expected that other nanoparticles or nanowires may also produce threads with this method.

*Automation of the process:* To date, Arc Assembly has been performed manually. This leads to inconsistencies with the experimentation as well as being time consuming for the researcher. If the process could be automated it would expedite and improve the reliability of future results, in addition to opening the route to industrial exploitation.

*Establishing a high yield of sp<sup>2</sup> crystalline bonds throughout the thread over a longer length.*

The ultimate goal for CNT threads is to exploit their nanoscale properties in macroscale applications. This thesis has delivered a process to accomplish this – however, it remains unfinished! Indications of sp<sup>2</sup> bonding between CNTs within 5 mm threads have been established, yet further research remains to produce a thread, which truly represents the remarkable properties of CNTs...

Regardless of how this work continues, it has been shown that a great many questions in the fields of dielectrophoresis, plasma physics and nanomaterials have been opened up from experiments facilitated by the new tungsten probes.

## Final Remark

This author encourages anyone interested in this work to further any discussion and criticism on this thesis such that the knowledge it attempts to contribute may always be improved. It is also hoped that other researchers and anyone interested feel free to use this work as a foundation or a supplement for new inventions and research beyond what is imagined here.

## Acknowledgements

I would like to thank *Professor. Dagou Zeze*, beyond what this short paragraph will portray, as a most patient, pragmatic and insightful supervisor. And for giving me the freedom, independence and encouragement to pursue ideas that I doubt many other academics would have even considered. I hope that many more students will benefit from him in the future...

And I would also like to thank:

*Dr. Andrew Gallant*, who gave me great support and encouragement for starting me down the road towards experimentation and research as my undergraduate supervisor.

*Professor Mike Petty*, for very wise and learned advice, especially towards academic publications.

*Professor Karl Coleman*, for helping in particular with the preparation of carbon nanotubes and Raman Spectroscopy.

*Mr. Leon Bowen and Dr Budhika Mendis* for showing and teaching me about the nanoscale world through the electron microscopes.

*Professor David Wood*, for his continuous and generous support throughout the PhD.

*Dr. Mark Rosamond*, for great down-to-earth advice at the beginning of the PhD.

*Dr Mike Cooke, Mr. John Gibson, Mr. Ian Hutchinson, Mr. Colin Wintrip and the staff and technicians of the school of engineering*, for helping and advising with many of the practical and logistical elements of this work.

I would also like to thank all my friends and family who have always expressed great interest and support in my work, and with whom many discussions have inspired many new ideas and motives.

## Publications, Conferences, Awards & Patents

### Journal Papers

Tungstate Sharpening: A versatile method for extending the profile of ultra-sharp tungsten probes

Review of Scientific Instruments 84, 035107 (2013); doi: 10.1063/1.4797483

R. Stone, M. Rosamond, K. Coleman, M. Petty, O. Kolosov, L. Bowen, V. Dubrovskii, and D. Zeze

### Conference Proceedings

Controlled Electrosharpening of Tungsten Probes

IEEE Nanotechnology 2012 August 20-23 Poster & Proceedings: doi: 10.1109/NANO.2012.6322013

R. Stone, M. Rosamond, K. Coleman, M. Petty, O. Kolosov, and D. Zeze

Magnetically enhanced batch electrosharpening of tungsten probes

EMRS 2014 Lille Spring Meeting May 26-30 (Analytical Techniques for Nanomaterials)

R. Stone, L. Bowen, K. Coleman, M. Petty, and D. Zeze

Carbon Nanotube Composites by Combined Plasma Polymerisation Dielectrophoresis

EMRS 2014 Lille Spring Meeting May 26-30 (Hybrid Materials in Biology, Chemistry & Physics)

R. Stone, L. Bowen, K. Coleman, M. Petty, and D. Zeze

## **Prizes**

1<sup>st</sup> Prize Poster, Durham School of Engineering and Computer Science, Research Day 2011

1<sup>st</sup> Prize Poster, EMRS 2014 Lille Spring Meeting May 26-30

1<sup>st</sup> Prize, Durham School of Engineering and Computer Science, Images in Technology Competition 2014

## **Patents**

*Patent Application:* Method and apparatus for electrochemical etching (submitted 15/05/2014)

WO 2015173541 A1 (reapplied as an international (PCT) patent 28/04/2015) R. Stone & D. Zeze

*Patent Application:* Arc discharge assembly of dielectrophoretically aligned conductive particles (submitted 15/05/2014) GB2526268 R. Stone & D. Zeze

# Appendix

This appendix includes figures of the expanded LabVIEW layout referred to in Chapter 2.7 including descriptions of the functions of each section of the program relevant to Figure 2.14, and future improvements.

## Automated Measurement

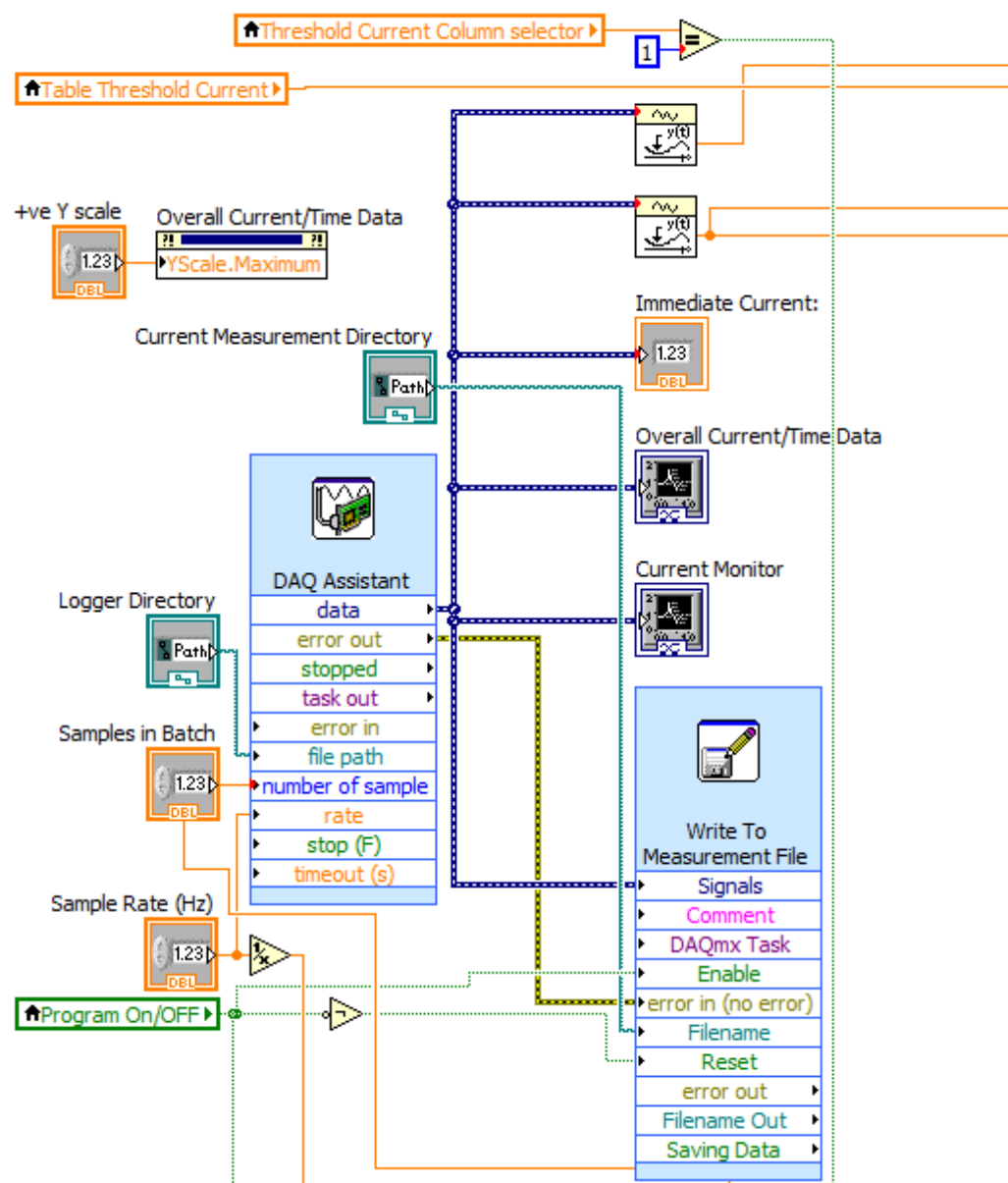


Figure A.1. Block diagram of measurement system in LabVIEW. This collects raw data from the IO device and sends data to measurement thresholds, integration and GUI sub-sections.

This uses a control block for the analogue inputs of the NI6009 IO device that takes inputs for the sampling rate and the number of samples taken continuously within that rate (i.e the total number of samples will be sample rate x samples in batch) Typically, the program just takes a single sample instead of a batch and determines the speed of measurement by just the sample rate. For other devices or measurement regimes (such as the drop-off method) it may be better to change the sampling values, as the devices can take measurements within a batch at a faster rate, provided the software can process the entire batch before the next batch of sampling takes place – if this is not the case the program will crash. However, given the timescale of the tungstate sharpening experiments is on the order of seconds, this program has a greater emphasis on reliability and uses a singular batch value to ensure no errors can occur.

Once the sample values are obtained they are automatically converted to a current value determined from a shunt resistor (typically  $100\Omega \pm 1\Omega$  and measured as such) and lies between 0.25 to -0.25A (which is hardware determined.) These values are then displayed via a graph which shows the current measurement over the last 10 values, to give the user a visual indicator of the gradient and value of the current. Another graph which displays all measurements (up to 144000 values) recorded of the process that gives the user a display of how the experiment is progressing (and typically looks as Figure 2.16) Single instantaneous measurements are also used for the current thresholds and noise thresholds detection, and a single value is displayed to the user. All measurements are also recorded directly into a text file with a timestamp, which is used for analysis of results afterwards.

## Measurement Thresholds

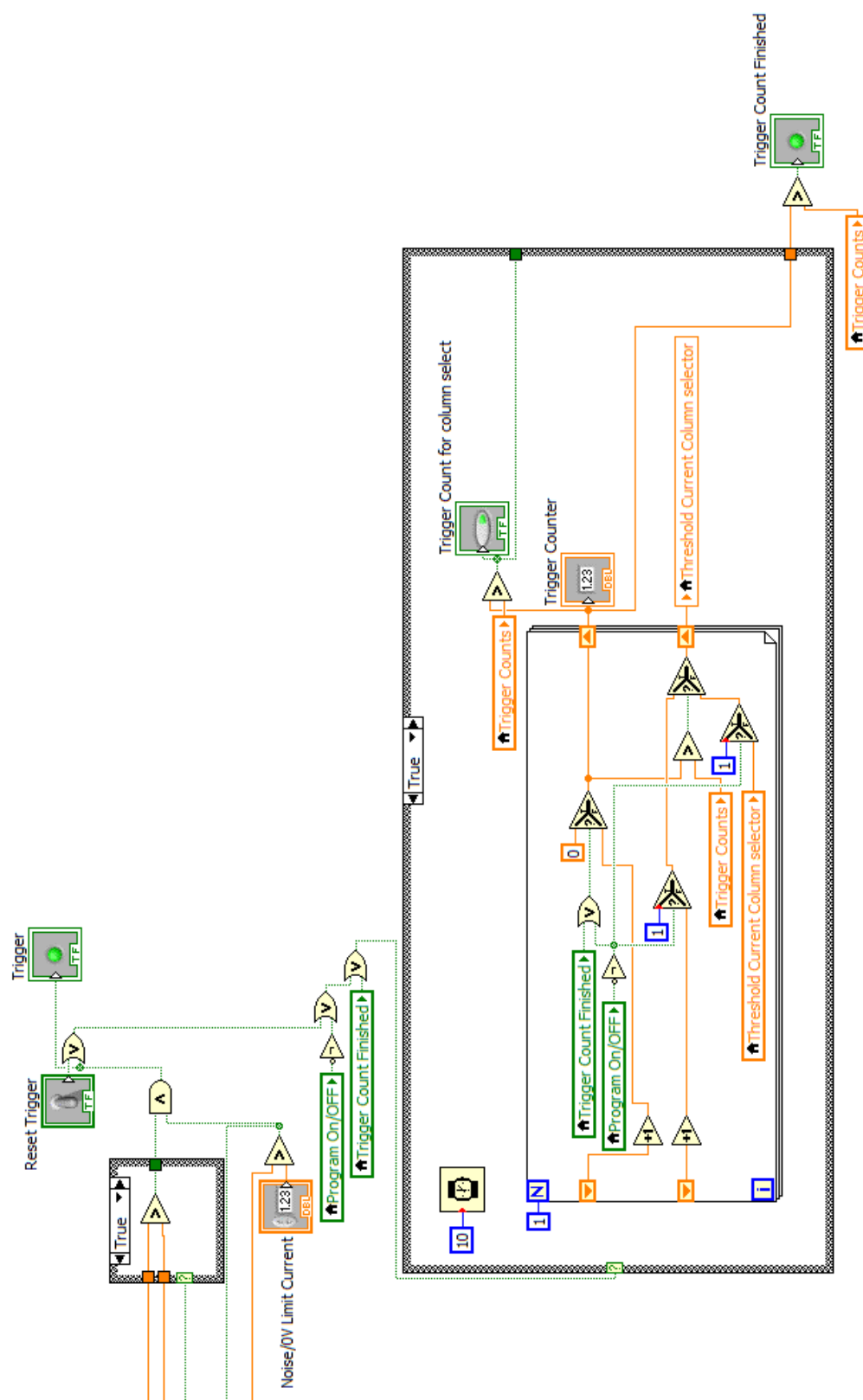


Figure A.2 Expanded view of current threshold trigger in LabVIEW. This makes comparisons over experimental values with user set parameters.



This uses a case structure containing an inequality block which compares the instantaneous current measurements against the fixed value entered by the user from the relevant stage in the threshold value in the table. The case structure may flip the inequality between 'less than' or 'greater than' depending on the stage, e.g. the first stage is typically greater than the measurement as the current rises with the removal of the outer oxide layer, and for the remaining stages is less than the measurement value.

If a measurement and threshold comparison is true, then the program counts the number of times this has occurred to a user selected value (typically 5) via a shift register. This is to prevent a single anomalous measurement to cause the program to change stages. This count will be automatically reset when it reaches the selected value but may also be manually reset if desired.

The noise control block is also a user controlled threshold measured against the measurements to ensure the values noise fluctuations do not trigger a change in the program stages. Additionally, all noise is cut out from the process (as shown in Figure. 2.16 this is typically 0.001) when the power is off. This prevents these small values cumulatively affecting the integrated values of the bulk coulometry and simplifies the management of any measurement files for later analysis.

## Programmatic Integration of Data

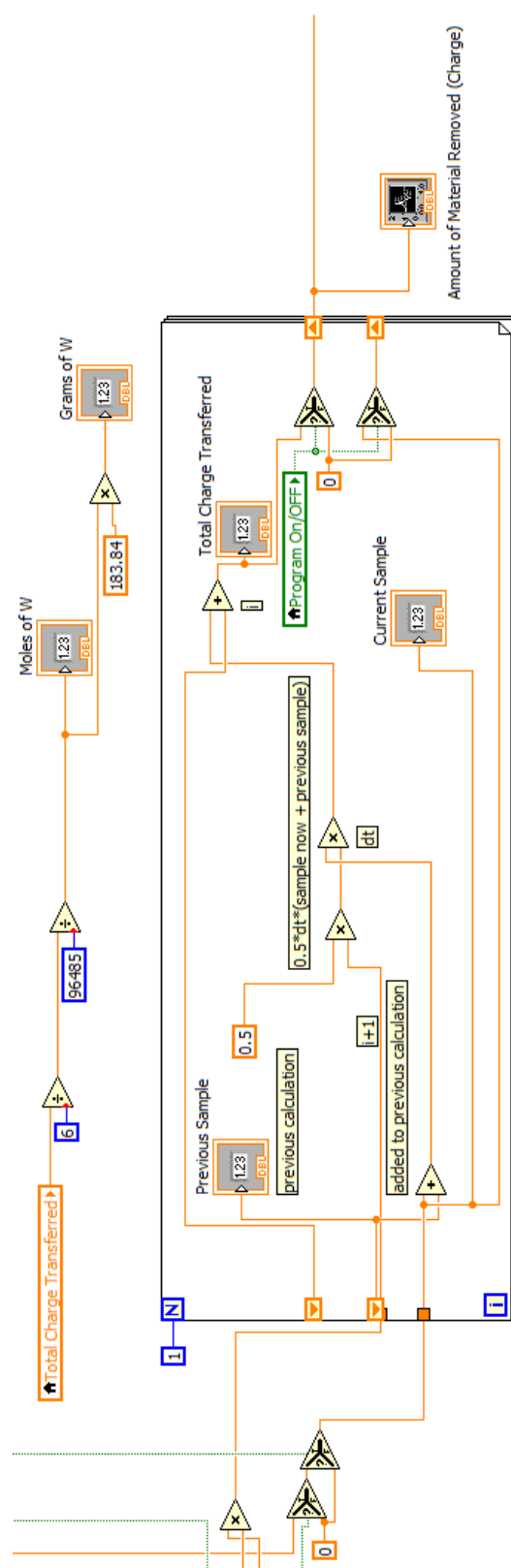


Figure A.3 Expanded view of the trapezium rule used for integration in LabVIEW. This allows for bulk coulometry analysis.

This performs an additional calculation over the last 2 measurements recorded. It uses the trapezium rule to approximate an integration over the data. Provided that data points are retrieved significantly faster than any significant changes in the actual current occur, this approximation should be acceptable. As shown from the current graphs in Figure 2.17 the feedback can adjust the etching routine to within 1% of a selected current threshold. This is typical of other etching regimes which use duty cycles above a given amount for a certain concentration, whilst the sample rate is typically 0.25s. The result of these calculations is entered into a graph displaying the data against to the full duration of the process which is a representation of the material removed during the process in the form of total charge transferred. An additional calculation is performed to give the actual mass value of tungsten removed as a single numerical value but is displayed independently to the graph. Currently, the program only performs this calculation for the reaction with tungsten (see equation 6) with the material values fixed within the program but could be manually adjusted for other materials in a future implementation.

## Process Control

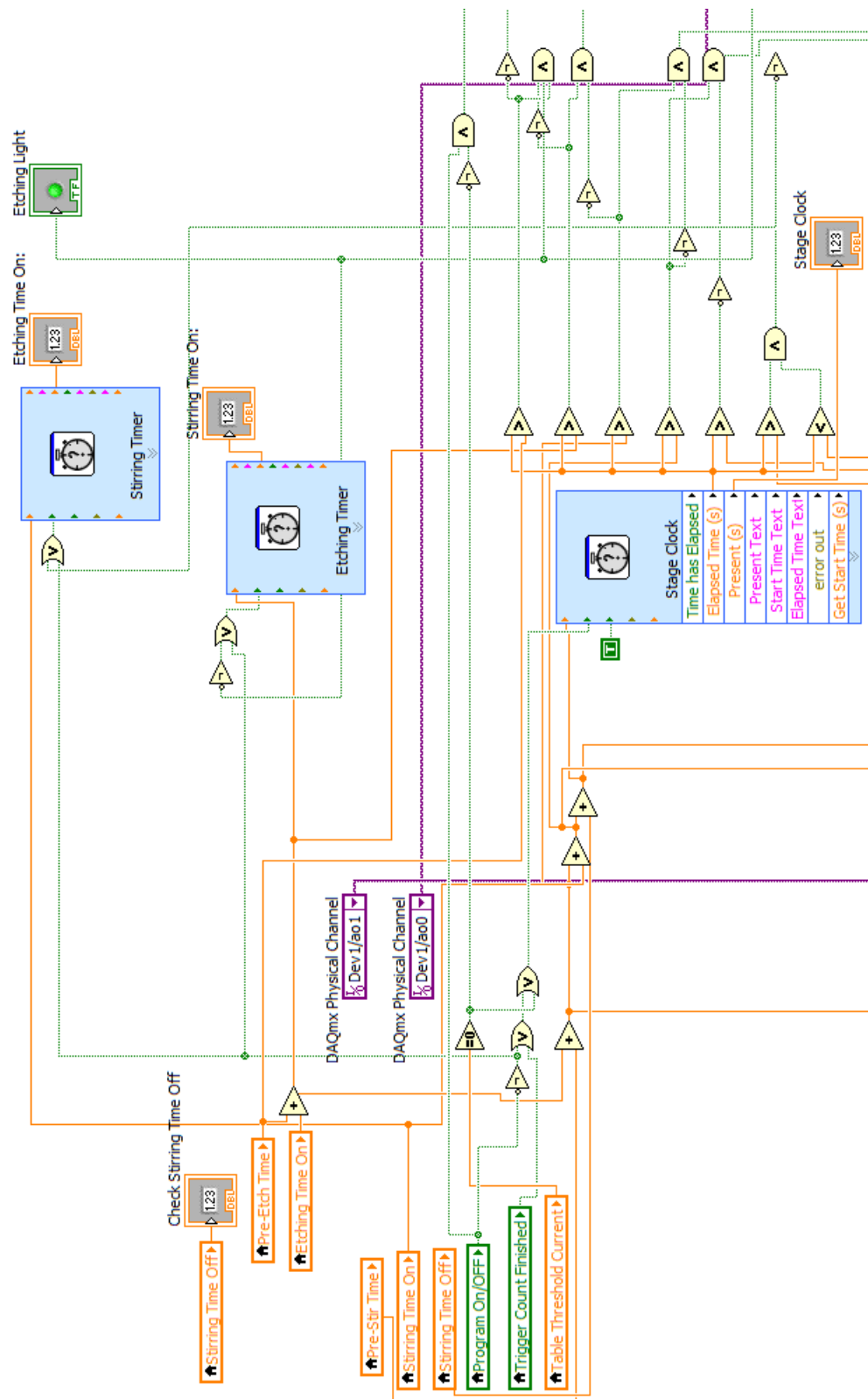


Figure A.3. Expanded view of process control. This controls and changes the sequence of events that make up a complete etch of a probe.

The stages progress through a series of timed sequences until they are interrupted by the current moving past the predetermined thresholds and changes the stage, which starts a new sequence. The sequences are controlled via 3 timers: (i) a main stage timer which measures the time over the whole sequence, (ii) separate etching and (iii) stirring timers. The user determined times are incrementally added as the sequence progresses and compared against the main stage timer. Based on whether the total time added from each part of the sequence is greater or less than the total time lapse, a Boolean logic circuit determines the states of the outputs. This system will work for any times the user requires. However, it does not allow the user to change the quantity of parameters within each sequence. Figure A.3 shows the timers connected to the relevant parameters in orange on the left-hand side to compare to the present value, this output then drives the Boolean circuits on the right-hand side in green.

## Output Control

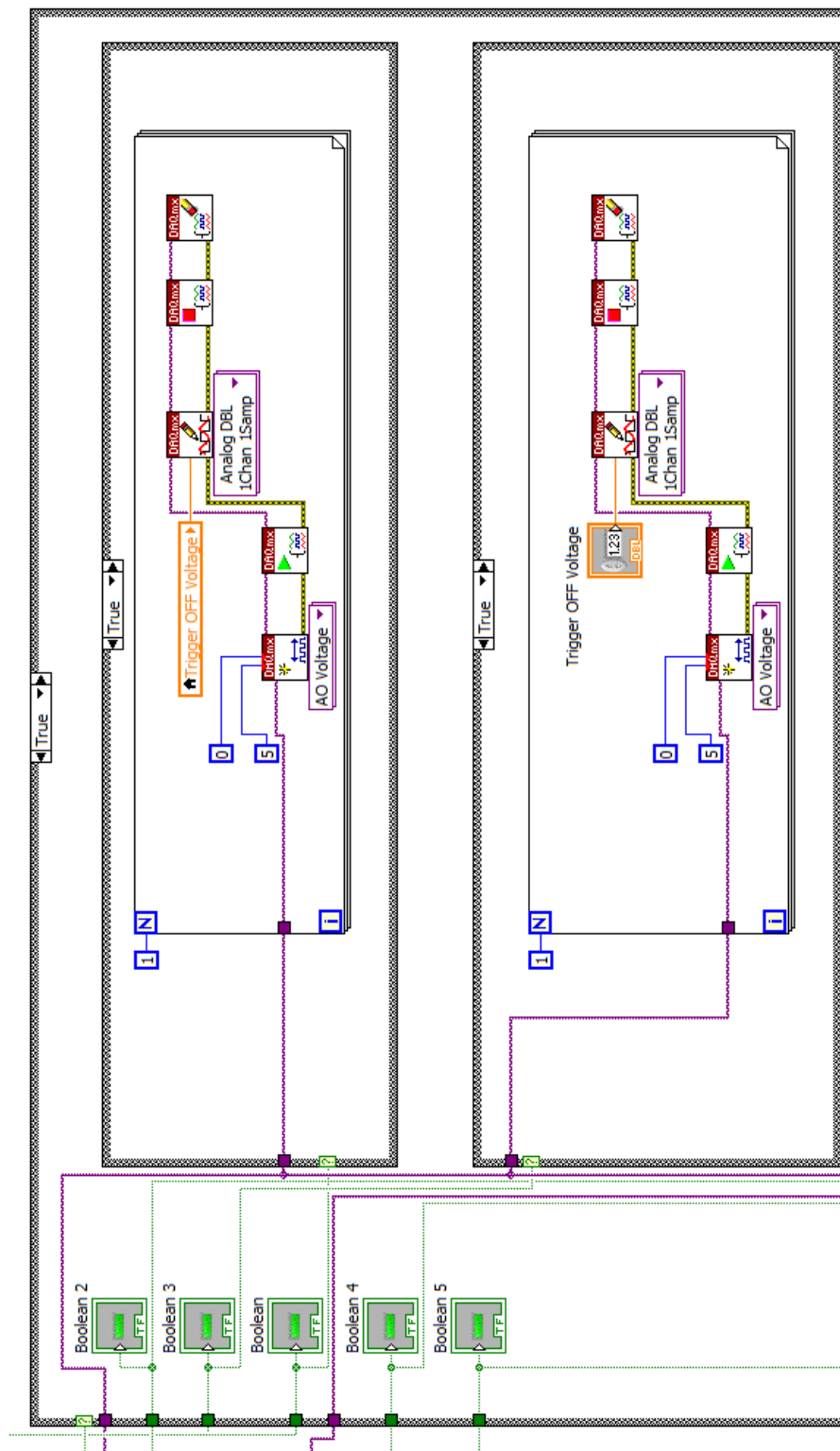


Figure A.4. Layout of output control in LabVIEW. This uses a Boolean code to set the outputs of the IO device. (See also top portion of Figure 2.17)

Currently the program requires 2 outputs for 3 states: OFF, etching and stirring. The fixed sequence within the program is OFF, stirring, OFF, etching, OFF. These outputs are directly linked to a Darlington array controlling relays within the circuit (outlined later in Figure 2.23).

LabVIEW allows for multiple layers of control over the I/O ports. The program initiates each output and writes an ON/OFF value to it and defaults each output to OFF if it is not used. This ensures that the states of the outputs are always known and there is no danger of an alternative combination of states occurring in the process i.e both tungsten probes and counter electrodes being connected as anode.

Each output is set to an ON/OFF value within a conditional block which will make a single increment of that value. The conditional blocks are started via the timing sequence when the associated Boolean logic for that part of the sequence is triggered.

## User Determined Parameters

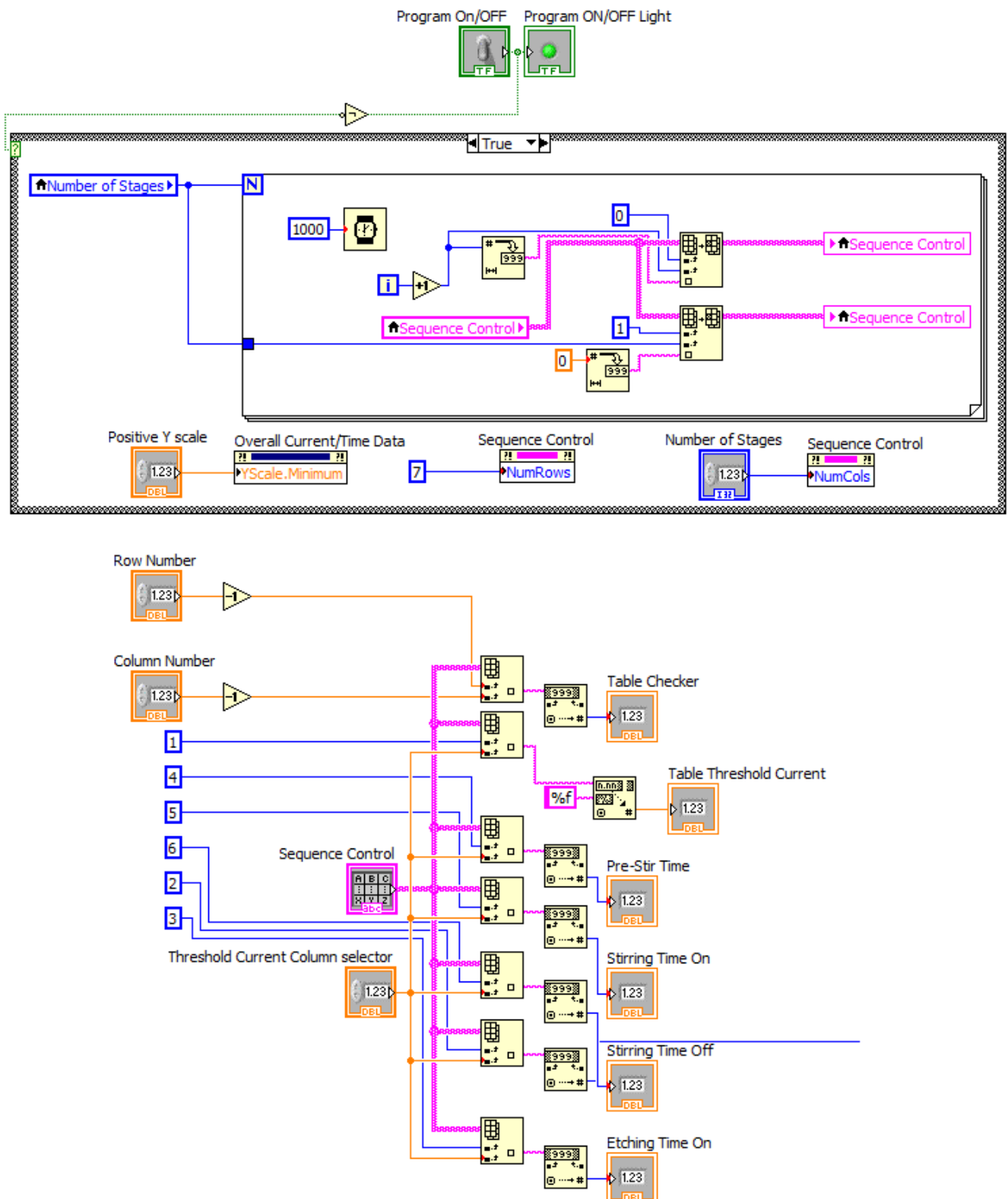


*Figure A.5* Layout of parameter control in LabVIEW. This controls the table in which the user can enter the desired parameters for an etching regime.



The user controls the process via a table of parameters which determine the current thresholds etching, stirring, and off times. The user can change the number of stages, but cannot change the number of parameters. The table is continuously read every second from a for-loop that places all the data into a 2D array. During operation, as the current triggers the threshold, a column selector for the array is incremented and the parameters (rows) for that column are transferred to the rest of the program via global variables.

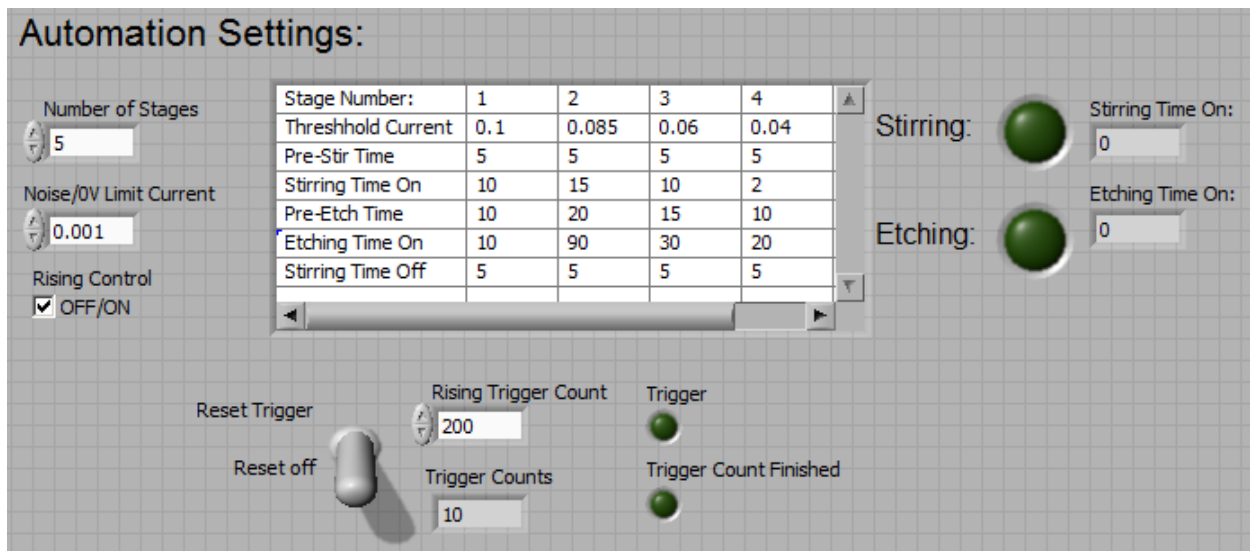


*Figure A.6* User Interface: control of etching parameters. This displays the user controlled parameters in addition to the current output state of the etching process.

3 files are saved with each experiment in text format, for the current measurements and respective time stamps, the integration calculations (mass etched) and a logger which is a labview specific document referring to the performance of the program (no directly relevant information from the experiment)

The sample rate of the process is also user controlled, for tungstate sharpening a sample is typically taken every 0.25s, however for analysis of the drop-off method it is essential that the program runs as fast as possible 0.05s/sample for the system used.

## Front End

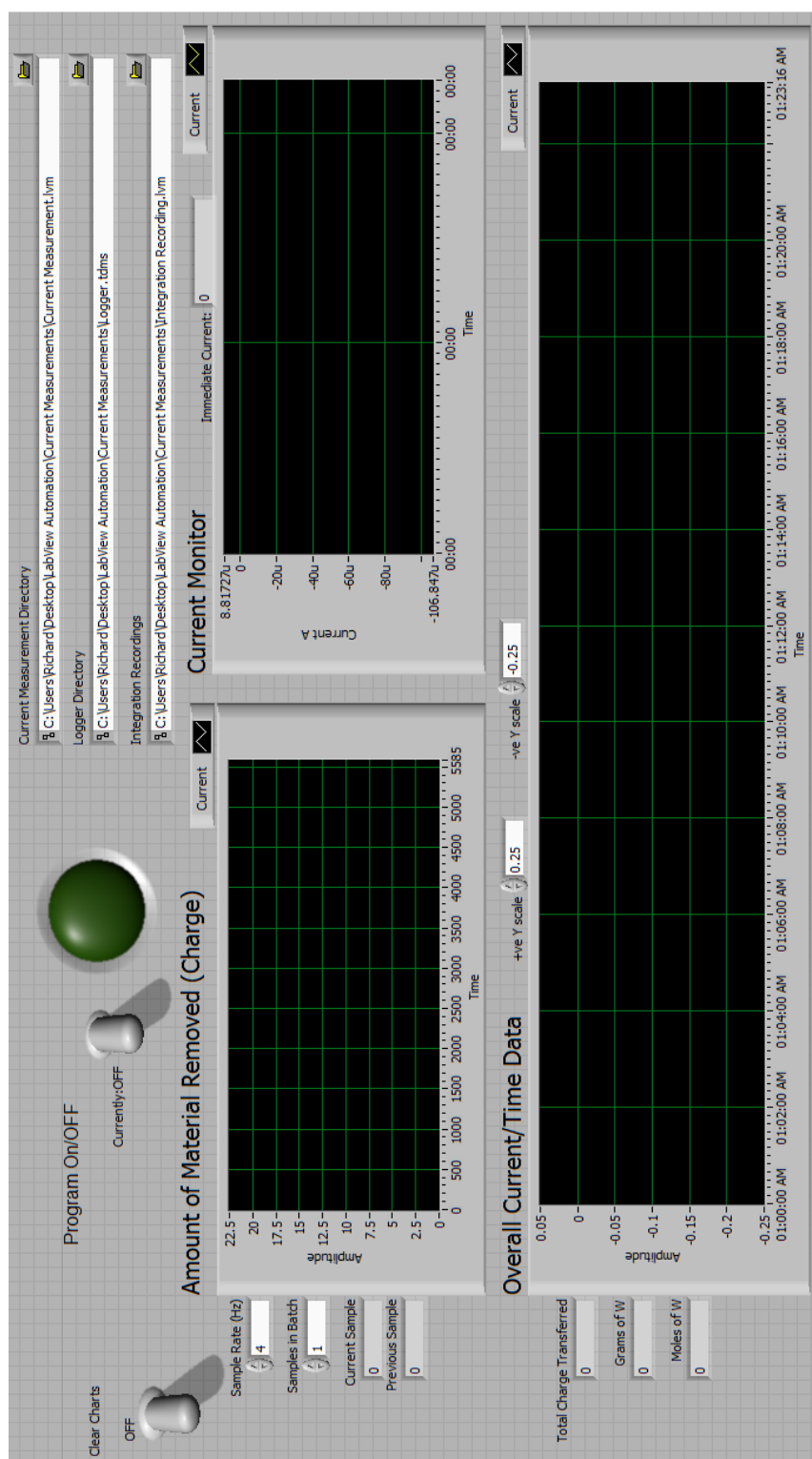


Figure A.7 User Interface: Graphs for In-situ measurements

The finished program gives the user a display of the overall progress of the process via bulk coulometry, which is a visually intuitive way for the user to check that the process is performing as expected. A current monitor shows instantaneous readings (a graph of the last 10 measurements) which are useful for showing the user if the current is approaching a threshold. And a graph of the total charge transferred in the process also gives the user an indication if the process is performing in a similar manner to other experiments with the same parameters

The process is broken into a series of stages which determines all aspects of the duty cycle of the etching. This is modified and displayed via an embedded spreadsheet within the program. A current threshold is entered which determines when one stage ends and another begins. It is possible for the user to have a threshold trigger from a measurement above or below the value. i.e. at the start of the process the current rises due to the oxide layer being removed from the tungsten. Therefore, the first stage triggers when the current rises above the threshold. For all other stages the current decreases such that the subsequent stages start when a measurement falls below the threshold. The thresholds are only triggered when a certain number of measurements satisfy the requirement – this is to prevent an anomalous reading disrupting the process.

### **Future Improvements**

- The program will be packaged into an installable file which can run on systems without LabVIEW.
- Error tracking, and in situ feedback to the user
- Optimised to reduce the time of sampling
- Compatibility over a variety of I/O devices
- Aesthetic changes such as windowed components, templated parameters for easier user control.

## Cover Picture Details

*Front Cover:* A tungsten probe in the middle of an electrosharpening experiment. The bubbles are oxygen released from the initial dissolution of  $\text{WO}_3$  in KOH. The wire was split before the process started which sometimes occurs due to tungsten's brittle nature. This rarely has any observable effect on the sharpening process as the top is etched before the sharp probe forms.

*Chapter 1:* A picture taken just before an arc assembly experiment, ensuring the tungsten probe is not in contact with the stainless steel counter electrode. Once the CNT mixture is placed over the electrodes, visibility becomes poor (hence the bright back-lighting).

*Chapter 2:* A single tungsten probe on the KOH-perfluorocarbon liquid-liquid interface. The lighting conditions were to see the edge-effect shadowgraphs.

*Chapter 3:* A SolidWorks PhotoView 360 render of the design for the magnetic batch-electrosharpening apparatus.

*Chapter 4:* A colourised SEM image of CNTs adhered to the tungsten probe after an arc assembly experiment. Some CNTs stick to the probe from the solution, but the majority on the lower-end of the probe are from plasma adhesion. The purple glow is purely aesthetic.

*Chapter 5:* A batch of 316 stainless steel Razor blades after being etched – the curved nature of the blades is still under investigation – but thought to be due to the rotational motion of the fluid around the edges of the blade, from the Lorentz force.